



I E V A   M A R K Ū N I E N Ē

---

**DEVELOPMENT OF A  
PIEZOELECTRIC COMPOSITE  
MATERIAL BASED ON  
BETA-PHASE POLYVINYLDENE  
FLUORIDE FOR BIOMECHANICAL  
SENSORS**

---

D O C T O R A L   D I S S E R T A T I O N

K a u n a s  
2 0 2 5

KAUNAS UNIVERSITY OF TECHNOLOGY

IEVA MARKŪNIENĖ

DEVELOPMENT OF A PIEZOELECTRIC  
COMPOSITE MATERIAL BASED ON BETA-  
PHASE POLYVINYLDENE FLUORIDE FOR  
BIOMECHANICAL SENSORS

Doctoral dissertation  
Technological Sciences, Mechanical Engineering (T 009)

2025, Kaunas

The dissertation has been prepared at the Department of Mechanical Engineering of the Faculty of Mechanical Engineering and Design of Kaunas University of Technology in 2021–2025. The research has been sponsored by the Research Council of Lithuania.

The doctoral right has been granted to Kaunas University of Technology together with Vytautas Magnus University.

**Research supervisor:**

Prof. dr. Giedrius JANUŠAS (Kaunas University of Technology, Technological Sciences, Mechanical Engineering, T 009).

**Research consultant:**

Dr. Joris VĖŽYS (Kaunas University of Technology, Technological Sciences, Mechanical Engineering, T 009).

**Edited by:** English language editor Birutė Jurkšaitė (Publishing House *Technologija*), Lithuanian language editor Aurelija Gražina Rukšaitė (Publishing House *Technologija*).

**Dissertation Defence Board of Mechanical Engineering Science Field:**

Prof. Dr. Hab. Vytautas OSTAŠEVIČIUS (Kaunas University of Technology, Technological Sciences, Mechanical Engineering, T 009) – **chairperson**;

Prof. Dr. Regita BENDIKIENĖ (Kaunas University of Technology, Technological Sciences, Mechanical engineering, T 009);

Prof. Dr. Sergei KRUCHININ (National Academy of Sciences of Ukraine, Ukraine, Natural Sciences, Physics, N 002);

Prof. Dr. Juozas PADGURSKAS (Vytautas Magnus University, Technological Sciences, Mechanical Engineering, T 009);

Assoc. Prof. Dr. Kęstutis PILKAUSKAS (Kaunas University of Technology, Technological Sciences, Mechanical Engineering, T 009).

The dissertation defence will be held on 6 June 2025, at 10 a.m. in a public meeting of the Dissertation Defence Board of the Mechanical Engineering science field at the Rectorate Hall of Kaunas University of Technology.

Address: K. Donelaičio 73-402, LT-44249 Kaunas, Lithuania.

Phone: (+370) 608 28 527; email [doktorantura@ktu.lt](mailto:doktorantura@ktu.lt)

The dissertation was sent out on 6 May, 2025.

The dissertation is available on the website <http://ktu.edu>, at the Library of Kaunas University of Technology (Gedimino 50, LT-44239 Kaunas, Lithuania) and the library of Vytautas Magnus University (K. Donelaičio 52, Kaunas, LT-44244, Lithuania).

© I. Markūnienė, 2025

KAUNO TECHNOLOGIJOS UNIVERSITETAS

IEVA MARKŪNIENĖ

PJEZOELEKTRINĖS KOMPOZITINĖS  
MEDŽIAGOS BETA FAZĖS  
POLIVINILIDENFLUORIDO PAGRINDU  
KŪRIMAS BIOMECHANINIAMS JUTIKLIAMS

Daktaro disertacija  
Technologijos mokslai, mechanikos inžinerija (T 009)

2025, Kaunas

Disertacija rengta 2021–2025 metais Kauno technologijos universiteto Mechanikos inžinerijos ir dizaino fakultete, Mechanikos inžinerijos katedroje. Mokslinius tyrimus rėmė Lietuvos mokslo taryba.

Doktorantūros teisė Kauno technologijos universitetui suteikta kartu su Vytauto Didžiojo universitetu.

**Mokslinis vadovas:**

prof. dr. Giedrius JANUŠAS (Kauno technologijos universitetas, technologijos mokslai, mechanikos inžinerija, T 009).

**Mokslinis konsultantas:**

dr. Joris VĖŽYS (Kauno technologijos universitetas, technologijos mokslai, mechanikos inžinerija, T 009).

**Redagavo:** anglų kalbos redaktorė Birutė Jurkšaitė (leidykla „Technologija“), lietuvių kalbos redaktorė Aurelija Gražina Rukšaitė (leidykla „Technologija“).

**Mechanikos inžinerijos mokslo krypties disertacijos gynimo taryba:**

prof. habil. dr. Vytautas OSTASEVIČIUS (Kauno technologijos universitetas, technologijos mokslai, mechanikos inžinerija, T 009) – **pirmininkas**;

prof. dr. Regita BENDIKIENĖ (Kauno technologijos universitetas, technologijos mokslai, mechanikos inžinerija, T 009);

prof. dr. Sergei KRUCHININ (Ukrainos nacionalinė mokslo akademija, Ukraina, gamtos mokslai, fizika, N 002);

prof. dr. Juozas PADGURSKAS (Vytauto Didžiojo universitetas, technologijos mokslai, mechanikos inžinerija, T 009);

doc. dr. Kęstutis PILKAUSKAS (Kauno technologijos universitetas, technologijos mokslai, mechanikos inžinerija, T 009).

Disertacija bus ginama viešame Mechanikos inžinerijos mokslo krypties disertacijos gynimo tarybos posėdyje 2025 m. birželio 6 d. 10 val. Kauno technologijos universiteto Rektorato salėje.

Adresas: K. Donelaičio g. 73-402, LT-44249 Kaunas, Lietuva.

Tel. (+370) 608 28 527; el. paštas [doktorantura@ktu.lt](mailto:doktorantura@ktu.lt)

Disertacija išsiųsta 2025 m. gegužės 6 d.

Su disertacija galima susipažinti interneto svetainėje <http://ktu.edu>, Kauno technologijos universiteto bibliotekoje (Gedimino g. 50, LT-44239 Kaunas, Lietuva) ir Vytauto Didžiojo universiteto bibliotekoje (K. Donelaičio g. 52, Kaunas, LT-44244, Lietuva).

## CONTENTS

LIST OF TABLES .....	8
LIST OF FIGURES .....	9
LIST OF ABBREVIATIONS .....	12
INTRODUCTION .....	14
1. ANALYSIS OF PIEZOELECTRIC COMPOSITES AND FILLERS USED FOR SENSING APPLICATIONS WITH DATA PROTECTION EVALUATION	17
1.1. Data protection in biosensors .....	17
1.1.1. Evaluation of data protection for wearable and implantable biosensors	23
1.2. Types of sensors .....	28
1.3. Piezoelectric composites .....	29
1.3.1. Effects of PVDF $\beta$ -phase on piezoelectric sensor applications .....	33
1.3.2. Hydroxyapatite (HA) material .....	35
1.3.3. Graphene oxide (GO) material .....	35
1.3.4. Silver nitrate ( $\text{AgNO}_3$ ) material .....	36
1.4. Chapter conclusions .....	37
2. MATERIALS AND EXPERIMENTAL METHODOLOGY .....	38
2.1. X-ray diffraction measurement methodology .....	38
2.2. Fourier transform infrared (FTIR) spectroscopy measurement methodology and $\beta$ -phase transformation .....	38
2.3. Scanning electron microscope (SEM) measurement methods .....	39
2.4. Energy-dispersive X-ray (EDX) and mapping measurement methodology ..	40
2.5. Electrical potential measurement methodology .....	41
2.6. Hydrophilicity testing.....	42
2.7. Piezoelectric coefficient ( $d_{33}$ ) measurement.....	43
2.8. Surface roughness measurement methodology .....	45
2.9. Multifractal spectra measurement methodology .....	46
2.10. Dynamic investigation methodology .....	46
2.11. Four-point probe measurement methodology .....	48
2.12. Synthesis of hydroxyapatite (HA).....	50
2.13. Chapter conclusions .....	51
3. SYNTHESIS AND ANALYSIS OF PIEZOELECTRIC PVDF COMPOSITE MATERIALS .....	52
3.1. Development of PVDF-based materials with hydroxyapatite (HA) and silver nitrate ( $\text{AgNO}_3$ ) .....	52
3.1.1. Preparation of PVDF/HA/ $\text{AgNO}_3$ composites .....	52
3.1.2. Investigation of crystallinity parameters and particle size by X-ray diffraction .....	53
3.1.3. Investigation of chemical properties and $\beta$ -phase transformation by Fourier transform infrared (FTIR) spectroscopy .....	55
3.1.4. Morphology investigation with a scanning electron microscope (SEM)	56
3.1.5. Chemical components analysis by energy dispersive X-ray (EDX) method .....	58

3.1.6. Study of electrical potential .....	60
3.1.7. Hydrophilic analysis and results .....	60
3.1.8. Piezoelectric coefficient ( $d_{33}$ ) measurement results .....	61
3.1.9. Surface roughness properties and results .....	62
3.1.10. Multifractal spectra analysis .....	63
3.1.11. Dynamic investigation results .....	69
3.1.12. Chemical components analysis by mapping method .....	71
3.1.13. Conductivity resistance investigation .....	72
3.1.14. Mathematical model of dynamic investigation .....	73
3.2. Development of PVDF-based materials with hydroxyapatite (HA), graphene oxide (GO), and silver nitrate ( $\text{AgNO}_3$ ) .....	75
3.2.1. Preparation of PVDF/HA/GO/ $\text{AgNO}_3$ composites .....	75
3.2.2. Morphology investigation with a scanning electron microscope (SEM) .....	76
3.2.3. Chemical components analysis by energy dispersive X-ray (EDX) and mapping methods .....	77
3.2.4. Investigation of chemical properties and $\beta$ -phase transformation .....	79
3.2.5. Hydrophilic properties analysis and results .....	80
3.2.6. Electrical investigation of four-point probe pulses .....	82
3.2.7. Piezoelectric coefficient ( $d_{33}$ ) measurement results .....	83
3.2.8. Surface roughness properties and results .....	83
3.3. Chapter conclusions .....	85
4. APPLICATION AND INTEGRATION OF A PIEZOELECTRIC COMPOSITE MATERIAL .....	86
4.1. Comparison of the results of the created composites and the influence of graphene oxide (GO) on their properties .....	86
4.2. Application and integration of a functional element .....	90
4.3. Chapter conclusions .....	91
5. CONCLUSIONS .....	92
6. SANTRAUKA .....	93
6.1. Duomenų apsauga biojutikliuose .....	96
6.1.1. Nešiojamųjų ir implantuojamųjų biojutimų duomenų apsaugos įvertinimas .....	97
6.2. Pjezoelektriniai kompozitai .....	99
6.2.1. PVDF $\beta$ fazės poveikis pjezoelektriniams jutikliams .....	100
6.2.2. HA-hidroksiapatito medžiaga .....	101
6.2.3. GO – grafeno oksido medžiaga .....	102
6.2.4. $\text{AgNO}_3$ – sidabro nitrato medžiaga .....	102
6.3. Medžiagos ir ekesperimentinė metodika .....	103
6.3.1. Dinaminis tyrimas .....	103
6.3.2. Pjezoelektrinio koeficiento $d_{33}$ matavimas .....	104
6.3.3. 4 zondų matavimas .....	105
6.4. Pjezoelektrinių PVDF kompozitinių medžiagų sintezė ir analizė .....	106
6.4.1. Kompozitų PVDF/HA/ $\text{AgNO}_3$ paruošimas .....	107
6.4.2. Elektros potencialo tyrimas .....	107
6.4.3. Pjezoelektrinio koeficiento $d_{33}$ matavimo rezultatai .....	108

6.4.4. Elektrinių savybių matavimas (4 zondų) .....	109
6.5. PVDF pagrindu pagamintų medžiagų su HA, GO ir AgNO <sub>3</sub> užpildais kūrimas .....	111
6.5.1. Kompozitų PVDF/HA/GO/AgNO <sub>3</sub> paruošimas .....	111
6.5.2. Elektrinis keturių taškų zondo impulsų matavimas .....	111
6.5.3. Pjezoelektrinio koeficiento d <sub>33</sub> matavimo rezultatai .....	112
6.6. Sukurtų kompozitų rezultatų palyginimas ir GO įtaka savybėms .....	113
6.6.1. Funkcinio elemento taikymas ir integravimas .....	115
6.7 Išvados.....	116
REFERENCES .....	118
CURRICULUM VITAE .....	128
ACKNOWLEDGMENTS .....	130



## LIST OF TABLES

Table 1.1. Comparison of piezoelectric composites .....	31
Table 3.1. Concentrations and recipes of samples with PVDF/HA/AgNO <sub>3</sub> .....	53
Table 3.2. $\beta$ concentrations of samples with PVDF, HA, and AgNO <sub>3</sub> .....	56
Table 3.3. EDX results and component concentrations in samples.....	59
Table 3.4. Energy values extracted for each sample .....	60
Table 3.5. Mapping results of four specimens.....	71
Table 3.6. Parameters for the numerical model of the PVDF/0.05HA/AgNO <sub>3</sub> sample .....	73
Table 3.7. Theoretical and practical values comparison of dynamic investigation and electrical potentials .....	74
Table 3.8. Concentrations of samples with PVDF/HA/GO/AgNO <sub>3</sub> .....	75
Table 3.9. Chemical composition of specimens. ....	77
Table 3.10. Mapping results of four specimens.....	78
Table 3.11. $\beta$ concentrations of samples with PVDF, HA, GO, and AgNO <sub>3</sub> .....	80
Table 4.1. Concentrations and recipes of samples .....	86
6.1 lentelė. Mėginių su PVDF/HA/AgNO <sub>3</sub> koncentracijos ir receptūros .....	107
6.2 lentelė. Kiekvieno mėginio išskirtos energijos vertės rezultatai.....	108
6.3 lentelė. Mėginių su PVDF/HA/GO/AgNO <sub>3</sub> koncentracijos ir receptūros .....	111
6.4 lentelė. Mėginių koncentracijos ir receptai.....	113

## LIST OF FIGURES

Fig. 1.1. Types of attackers and attack information .....	18
Fig. 1.2. Security key based on phase transitions in $\alpha$ -phase, $\beta$ -phase, and $\gamma$ -phase .....	21
Fig. 1.3. Nmap scan .....	22
Fig. 1.4. DDoS attack .....	22
Fig. 1.5. MITM attack .....	23
Fig. 1.6. Network topology.....	24
Fig. 1.7. Interface of the patient tracking system .....	24
Fig. 1.8. Attack flow diagram.....	25
Fig. 1.9. Attack detection using artificial intelligence algorithms.....	26
Fig. 1.10. Detection of attackers using the artificial intelligence model. ....	27
Fig. 1.11. Molecular structure of PVDF and, representation of its $\alpha$ , $\beta$ , and $\gamma$ phases .....	34
Fig. 2.1. FTIR measurement: (a) measuring of sample; (b) spectrometer.....	39
Fig. 2.2. Au coating machine: (a) mirror plate with samples; (b) Nanovak NVEB-600 machine.....	40
Fig. 2.3. Scanning electron microscopy FEI QUANTA 250 machine .....	40
Fig. 2.4. EDX measurement: (a) samples prepared for scanning; (b) Esprit system analysis .....	41
Fig. 2.5. Scheme for measuring the electrical properties of samples .....	41
Fig. 2.6. Hydrophilicity measurement scheme: (1) drop on samples, (2) coating base, (3,4) convex double lenses, (5) Guppy CMOS camera, and (6) software system....	44
Fig. 2.7. PolyK Quasi-Static Piezoelectric $d_{33}$ Meter .....	45
Fig. 2.8. Schematic of the piezoelectric constant $d_{33}$ by PolyK Quasi-Static Piezoelectric $d_{33}$ Meter .....	45
Fig. 2.9. Samples prepared on steel plates coated with different PVDF materials with a conductive copper phase on top and contacts.....	47
Fig. 2.10. Experimental setup with key hardware components: (1) – computer, (2) – oscilloscope, (3) – signal generator, (4) – signal amplifier, (5) – laser distance meter, (6) – clamps, (7) – PVDF-covered metal plate, (8) – vibrator .....	47
Fig. 2.11. Four-point probe method: I is the current applied between the outer probes (1, 4), U is the voltage between probes 2 and 3, and R is the sheet resistance.....	48
Fig. 2.12. The four-point probe method measuring equipment: (a) specimen measurement; (b) Model 4200-SCS Semiconductor Characterization System .....	49
Fig. 2.13. Visualization of the chemical structure of (a) HA, (b) PVDF, and (c) $\text{AgNO}_3$ .....	50
Fig. 2.14. Synthesis of HA via sol-gel method.....	50
Fig. 3.1 Synthesis scheme of composite solid films with PVDF/HA/ $\text{AgNO}_3$ .....	53
Fig. 3.2. X-ray diffraction results of samples with PVDF, HA, and $\text{AgNO}_3$ .....	54
Fig. 3.3. FTIR spectrum results of deposited thin films .....	55
Fig. 3.4. FTIR spectrum peaks of $\alpha$ and $\beta$ phases.....	56
Fig. 3.5. SEM images of PVDF/HA/ $\text{AgNO}_3$ samples .....	58
Fig. 3.6. EDX results: 1 – PVDF/0.05HA, 2 – PVDF/0.1HA, 3 –PVDF/ $\text{AgNO}_3$ , 4 – PVDF/HA/ $\text{AgNO}_3$ , 5 – PVDF.....	59

Fig. 3.7. Droplet imaging and wetting angles of sample on solid films .....	60
Fig. 3.8. $d_{33}$ measurement results of each sample.....	61
Fig. 3.9. Str (texture aspect ratio) and Sdr (developed interfacial area ratio).....	62
Fig. 3.10. Surface roughness images of s 1–5 .....	63
Fig. 3.11. Multifractal spectra of individual images, illustrating stable distributions that suggest a homogeneous structure – for samples 15 .....	65
Fig. 3.12. Graphs showing the juxtaposition of three key points in the multifractal spectrum ( $h^0$ , and $h_{\max}$ ) and a graph showing the change in entropy with each increment for samples 1–5 (a–e) .....	68
Fig. 3.13. Data collection from three sensors: accelerometer (1), laser rangefinder (2), and both contacts from our newly created sensor (3); (a) signals using the 1st newly created sensor, (b) signals using the 2nd newly created sensor, (c) signals using the 3rd newly created sensor, (d) signals using the 4th newly created sensor, (e) -signals using the 5th newly created sensor.....	70
Fig. 3.14. Results of electrical measurement of four-point probe pulses: sample 1 – PVDF/0.05HA, sample 2 – PVDF/0.1HA, sample 3 – PVDF/AgNO <sub>3</sub> , sample 4 – PVDF/HA/AgNO <sub>3</sub> , sample 5 – PVDF.....	72
Fig. 3.15. Surface electrical potential of samples at a frequency of 11 Hz and deformation of the functional element.....	74
Fig. 3.16. Schematic methods of sample preparation.....	75
Fig. 3.17. SEM analysis of each sample.....	76
Fig. 3.18. EDX graph results of each sample .....	77
Fig. 3.19. FTIR spectrum of PVDF/AgNO <sub>3</sub> /GO, PVDF/HA/AgNO <sub>3</sub> , PVDF/HA/GO and PVDF/HA/AgNO <sub>3</sub> /GO specimens.....	79
Fig. 3.20. FTIR spectrum of $\alpha$ - and $\beta$ -phases in PVDF/AgNO <sub>3</sub> /GO, PVDF/HA/AgNO <sub>3</sub> , PVDF/HA/GO, and PVDF/HA/AgNO <sub>3</sub> /GO .....	80
Fig. 3.21. Drop liquid angle measurements: (a) water drop on sample 1, (b) sample 2, (c) sample 3, (d) sample 4, and (e) glycerol drop on sample 1, (f) sample 2, (g) sample 3, (h) sample 4 .....	81
Fig. 3.22. Results of electrical measurements using four-point probe pulses .....	82
Fig. 3.23. $d_{33}$ measurement results: sample 1 – PVDF/AgNO <sub>3</sub> , GO, sample 2 – PVDF/HA/AgNO <sub>3</sub> , sample 3 – PVDF/HA/GO, and sample 4 – PVDF/HA/AgNO <sub>3</sub> /GO .....	83
Fig. 3.24. STR (texture aspect ratio) and Sdr (developed interfacial area ratio) .....	84
Fig. 3.25. Surface roughness images of samples 1–4 .....	84
Fig. 4.1. Comparison of SEM images of composites .....	87
Fig. 4.2. Comparison of $d_{33}$ piezoelectric constants for all samples .....	88
Fig. 4.3. Electrical conductivity results from four-probe measurements; comparison of all samples .....	89
Fig. 4.4. Comparison of FTIR spectrum results for all samples.....	89
Fig. 4.5. Piezoelectric pressure sensor structure, PUF in $\beta$ -phase, and FTIR peaks of $\beta$ -phase in created functional elements.....	90
6.1 pav. Sukurtas saugos raktas fazės perėjimu $\alpha$ fazėje, $\beta$ fazėje ir $\gamma$ fazėje .....	97
6.2 pav. Tinklo topologija.....	98

6.3 pav. Atakų aptikimas naudojant dirbtinio intelekto algoritmus.....	99
6.4 pav. PVDF molekulinė struktūra, vizualinis $\alpha$ , $\beta$ ir $\gamma$ fazių vaizdas .....	101
6.5 pav. Eksperimento paruošimas matavimams, parodant pagrindines naudojamos techninės įrangos dalis: 1 – kompiuteris, 2 – PicoScope 3424 osciloskopas (Pico Technology, Kembridžsyras, JK), 3 – signalų generatorius UNI-T UTG1022X (Uni-Trend Technology Ltd., Kinija), 4 – signalo stiprintuvas VEB Metro LV103, 5 – LK-G82 lazerio nuotolis metras (Keyence, Elmwood Park, Naujasis Džersis, JAV), 6 – spaustukai, 7 – plieninė plokštė, padengta PVDF medžiagomis, ir vario laidžioji fazė, 8 – vibratorius .....	103
6.6 pav. Pjezoelektrinės konstantos $d_{33}$ matavimo schema, naudojant PolyK statinį pjezoelektrinį $d_{33}$ matuoklį .....	105
6.7 pav. Keturių taškų zondo metodo principas: $I$ yra srovė, taikoma tarp išorinių zondų, $U$ yra įtampos pokytis tarp zondų 2 ir 3, $R$ yra lakšto varža.....	105
6.8 pav. Keturių taškų zondo metodo matavimo įranga: a) mėginio matavimas; b) 4200-SCS modelio puslaidininkių charakteristikų sistema .....	106
6.9 pav. Kompozitinių kietųjų plėvelių su PVDF/HA/AgNO <sub>3</sub> sintezės schema ....	107
6.10 pav. Mėginių elektrinių savybių matavimo schema .....	108
6.11 pav. $d_{33}$ konstantos mėginių matavimo rezultatai.....	109
6.12 pav. Keturių taškų zondo impulsų elektrinio matavimo rezultatai, 1 pavyzdys – PVDF/0,05HA, 2 pavyzdys – PVDF/0,1HA, 3 pavyzdys – PVDF/AgNO <sub>3</sub> , 4 pavyzdys – PVDF/HA/AgNO <sub>3</sub> , 5 pavyzdys – PVDF.....	110
6.13 pav. Mėginių PVDF/HA/GO/AgNO <sub>3</sub> paruošimo shema.....	111
6.14 pav. Keturių taškų zondo impulsų elektrinio matavimo rezultatai: PVDF/AgNO <sub>3</sub> /GO, PVDF/HA/AgNO <sub>3</sub> , PVDF/HA/GO ir PVDF/HA/AgNO <sub>3</sub> /GO.....	112
6.15 pav. $d_{33}$ rezultatai (matuojami statiniu $d_{33}$ matavimo įrenginiu), 1 mėginys – PVDF/AgNO <sub>3</sub> , GO, 2 pavyzdys – PVDF/HA/AgNO <sub>3</sub> , 3 mėginys – PVDF/HA/GO, 4 mėginys – PVDF/HA/AgNO <sub>3</sub> /GO.....	113
6.16 pav. $d_{33}$ pjezoelektrinių konstantų visų mėginių palyginimo rezultatai.....	114
6.17 pav. 4 zondo matavimų elektros laidumo rezultatai, visų mėginių palyginimas .....	114
6.18 pav. Visų mėginių FTIR spektro rezultatų palyginimas .....	115
6.19 pav. Pjezoelektrinio jutiklio struktūra, PUF – funkcija $\beta$ fazėje ir FTIR $\beta$ fazės smailės sukurtuose funkciniuose elementuose .....	116

## LIST OF ABBREVIATIONS

PVDF – Polyvinylidene fluoride  
HA – Hydroxyapatite  
AgNO<sub>3</sub> – Silver nitrate  
GO – Graphene oxide  
SEM – Scanning electron microscopy  
NPs– Nanoparticles  
rGO – Reduced graphene oxide  
AGNP– Silver nanoparticle  
GBMs – Graphene-based materials  
PUF – Physical unclonable function  
DMSO – Dimethyl sulfoxide  
MITM – Man-in-the-middle attack  
IC – Integrated circuit  
FPGA– Field programmable gate array  
TCP – Transmission control protocol  
MySQL – Relational database management system  
DDoS– Distributed denial-of-service  
DNA – Deoxyribonucleic acid  
SGD – Stochastic gradient descent  
SVM – Support vector machine  
MCC – Malicious mobile code  
CA – Certificate authority  
PLA – Polylactic acid  
PLC – Polycaprolactone  
ID – Identification  
LOx/HRP – Redox dye  
NADH/ NAD<sup>+</sup> – Nicotinamide adenine dinucleotide  
ALT/LDH – Ratio used to assess liver function and potential liver damage  
POx/HRP – Pyranose oxidase/horseradish peroxidase  
GDH/GLDH – Glutamate dehydrogenase  
HRP – Horseradish peroxidase  
ALT – Alanine aminotransferase  
PZT – Lead zirconate titanate  
SRAM PUF – Cryptographic root key  
a-IGZO TFTs – IGZO thin film transistors  
CRP – Challenge-response pair  
CPU – Central processing unit  
PVDF-HFP – Poly(vinylidene fluoride-co-hexafluoropropylene)  
DMF – Dimethylformamide  
BOD – Biochemical oxygen demand  
P(VDF-TrFE) – Poly(vinylidene fluoride trifluoroethylene)  
PI – Polyimides  
PAN – Polyacrylonitrile

ZnO – Zinc oxide  
PMN-PT – Lead magnesium niobate-lead titanate  
LiNbO<sub>3</sub> – Lithium niobate  
TTTT – All-trans conformations  
FTIR – Fourier-transform infrared  
EDX – Energy-dispersive X-ray spectroscopy  
MWCNT – Multi-walled carbon nanotubes  
Sdr – Interfacial area ratio  
Str – Material ratio  
DDoS – Denial-of-service attack  
ARP – Address resolution protocol  
MAC – Medium/media access control address  
IP – Internet protocol address  
PES – Polyethersulfone  
VON – Vonahi security  
LC – Inductor-capacitor

## INTRODUCTION

Information used in sensing technology can be a target for attackers. They can determine whether a person is wearing an implant and identify its type. In addition to capturing messages, attackers may also send commands, modify the information, and resend it. Therefore, when developing the functional element, it is first necessary to select a material production technology and then examine the possibilities for ensuring security.

The use of polymeric materials, or composites, is becoming increasingly necessary due to their affordability and wide availability. Composites consist of two or more materials with different properties combined. Polymers typically have high field strength and high dielectric properties. Piezoelectric polymers are suitable for a variety of device configurations as well as technical and engineering applications. Piezoceramic materials serve as the foundation for basic technical components in biomedical devices, acoustics, and microelectronics.

Due to its superior stability and electrical properties, polyvinylidene fluoride (PVDF) is one of the most appealing and advantageous fluoride polymeric materials in the industry. The piezoelectric properties of PVDF are attributed to the  $\beta$ - and  $\gamma$ -phases, which are polar crystalline phases. The  $\beta$ -phase has the largest electric dipole moment of all the crystalline phases. Therefore, increasing the  $\beta$ -phase content in the PVDF is an effective way to improve the piezoelectric properties of PVDF-based piezoelectric sensors. Several methods, such as stretching, polarization in a high electric field, thermal annealing, and filler insertion, can be used to induce dipole alignment and increase the  $\beta$ -phase fraction in PVDF.

By increasing the  $\beta$ -phase of PVDF, its piezoelectric response can be enhanced; hence, porous ceramics such as hydroxyapatite (HA) can be used as reinforcement to improve the piezoelectric properties of PVDF. The PVDF polymer and  $\alpha$ -PVDF/HA composites have mechanical properties, as well as dielectric, thermal, and physical properties, which are determined by factors such as thickness, structure, surface topography, and functional groups on the film surfaces.

Graphene-based materials (GBMs) can be widely applied in biomedical engineering. Graphene has very high mechanical strength, surface area, and thermal and electrical conductivity. Graphene oxide (GO) can be added to polymer matrices to enhance their mechanical, thermal, and electrical characteristics.

Silver nanoparticles ( $\text{Ag}^0$ ) release silver ions ( $\text{Ag}^+$ ), which interact with the phosphorous moieties of DNA. Adding a conductive phase, such as silver, can be advantageous for the following reasons: first, by increasing the sensitivity of the piezoelectric response, the conductive phase enhances charge transfer.

Solid layers, known as dielectric films, have extensive applications in the pharmaceutical, organic transistor, capacitor, sensor, microelectronics, and power electronics sectors. In the field of sensor applications, there are numerous threats, including cyber-attacks aimed at obtaining or controlling personal information. Therefore, biosensors are a potential area to explore the possibilities of attacks and methods for their protection.

The composite being developed is a potential material for information protection in this application domain. Physical unclonable functions (PUFs) are often found in cyber-physical systems. Using this type of PUF could add security features without investing in expensive new hardware.

**The aim of this doctoral thesis** is to develop a piezoelectric composite material based on a  $\beta$ -phase polyvinylidene fluoride for biomechanical sensors with data protection capabilities.

## Objectives

1. To investigate methods for data protection and materials used in wearable and implantable biomechanical sensors.
2. To synthesize a piezoelectric composite with  $\beta$ -phase transformation by incorporating hydroxyapatite (HA), graphene oxide (GO), and silver nitrate ( $\text{AgNO}_3$ ) nanoparticles into PVDF.
3. To evaluate the influence of HA and  $\text{AgNO}_3$  nanoparticles, as well as their different compositions, on the piezoelectric composite's electrical, mechanical, and morphological properties.
4. To evaluate the influence of GO on the piezoelectric, electrical, and morphological properties of a PVDF-based composite for sensing applications.

## Research methods

For preparation, the solvent casting method was used with dimethyl sulfoxide (DMSO) as the solvent. The vibration accelerometer KD35 (RFT GmbH, Schwabmünchen, Germany) was used for vibration experiments. The amplitude of the vibration of the metal plate and its end was measured using the Keyence 5 laser distance meter. Data were collected using the PicoScope 3424 oscilloscope. The software program PicoScope 6.14.69 was used to analyze the data once it was linked to a personal computer. A wide-area 3D measurement system was used for surface roughness analysis. For electrical four-probe measurement, the Model 4200-SCS Semiconductor Characterization System was used. The samples were coated using the e-Beam method. They were placed in an electron beam physical vapor deposition chamber (Nanovak NVEB-600), evacuated to a pressure of  $9 \times 10^{-6}$  Torr, and coated with gold to obtain a conductive surface for SEM analysis. The gold source was evaporated by heating the filament with a current of 56 mA, maintaining a constant layer thickness of 5 nm. Scanning electron microscopy (SEM) images were obtained using an FEI QUANTA 250 model. The  $d_{33}$  constant was measured using a PolyK Quasi-Static Piezoelectric  $d_{33}$  Meter. Theoretical vibration models were simulated using COMSOL Multiphysics software. A contact angle goniometer was used to measure angles and determine the contact angle between a liquid drop and a solid surface (Faculty of Mechanical Engineering and Design, Kaunas University of Technology). For EDX measurements, Bruker 127 eV equipment was used along with Esprit software for analysis. A Perkin Elmer UATR Two FT-IR spectrometer was used for Fourier-transform infrared (FTIR) analysis.



### **Scientific novelty**

1. PVDF-based piezoelectric composites with HA, GO, and AgNO<sub>3</sub> particles are biocompatible and suitable for the formation of biomechanical sensors with complex geometries.
2. The integration of piezoelectric properties and  $\beta$ -phase transformation in the composite material ensures data security and supports its application in the development of the Internet of Things.

### **Practical value of the work**

1. The methodology of synthesis of piezoelectric composite based on PVDF with HA, GO, and AgNO<sub>3</sub> nanoparticles has been developed to ensure the integration of piezoelectric properties and  $\beta$ -phase transformation in the composite material.
2. Functional elements based on the synthesized piezoelectric composite can be used to measure physical pulses while ensuring the security of input and output information.

### **Statements to be defended**

1. The synthesized piezoelectric composite exhibits piezoelectric properties at the micrometric level, while its mechanical, electrical, morphological, and hydrophobic properties are controlled by modifying the added nanoparticles.
2. The developed  $\beta$ -phase transformed piezoelectric composite is suitable for the development of biomechanical sensors.

### **Research approbation**

The results of the dissertation were published in two peer-reviewed scientific articles indexed in the Web of Science database with a citation rate in international (foreign) publishing houses, one article in a journal of a national publishing house, and one article in a Web of Science-indexed publication without a citation rate. The results were presented at five international scientific conferences: Mechanics 2021, Advanced Materials and Technologies 2022, Mechanics 2023, Engineering Mechanics 2023, and Mechanics 2024. Additionally, in 2024, the author participated in three international conferences: IEEE MEMSTECH 2024, Mechanics 2024, and the 2024 Innovations in Intelligent Systems and Applications Conference (ASYU).

### **Structure of the dissertation**

The dissertation consists of an introduction, a literature review, four main chapters, general conclusions of the final thesis, a summary in Lithuanian, a list of references, a curriculum vitae, and acknowledgments. The total length is 132 pages, with 74 figures, 16 tables, and 120 references.

# **1. ANALYSIS OF PIEZOELECTRIC COMPOSITES AND FILLERS USED FOR SENSING APPLICATIONS WITH DATA PROTECTION EVALUATION**

Attackers have already demonstrated that targeting sensors and devices is highly convenient for them [1]. Due to their widespread use and lack of security features, sensors and devices remain prime targets for attacks [1].

The functional element under development is a potential material for information protection applications. For security reasons, PUFs are commonly found in cyber-physical systems. By using this type of PUF, security features could be added without the need for investing in expensive new hardware [2].

The piezoelectric effect is commonly used in sensors, so the most popular materials with this property are reviewed below. Since polymer/ceramic composites are widely used and discussed, this chapter will focus on composites that have already been developed and studied with this composition. Compared to piezoelectric ceramics, PVDF is the most widely used organic piezoelectric material due to its lighter weight and versatility. PVDF films with 98.8%  $\beta$  phase are prepared at an ideal crystallization temperature of 60 °C using DMSO as a solvent. HA is an osteoconductive, biocompatible, bioactive, and thermodynamically stable material, which, when combined with biocompatible polymers (PVDF, polylactic acid (PLA), polycaprolactone (PCL), etc.), becomes a material with great potential for composite development [3]. GO and reduced GO (rGO) composite films exhibit improved dielectric, ferroelectric, and piezoelectric properties. The composite film with optimized GO concentration (0.16 wt%) has a conductivity of 25.6 (~2 times that of pure PVDF). A conductive phase such as silver can be beneficial because it increases the sensitivity of the piezoelectric response and improves charge transfer, which is a crucial aspect in the design of piezoelectric composites. Silver nanoparticles (AgNPs) can be used as a filler in PVDF to increase the  $\beta$ -phase content, as well as an antibacterial agent in industries or surgery.

## **1.1. Data protection in biosensors**

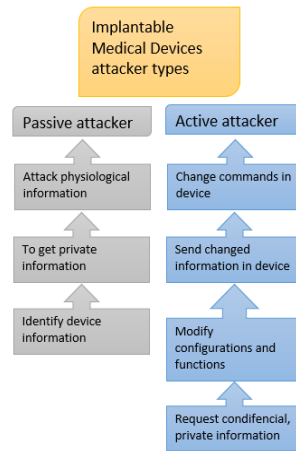
Attackers have already demonstrated that targeting sensors and devices is a convenient option for them [1]. Due to the widespread use and lack of security features, sensors and devices appear to be a prime target [1].

The composite being developed is a potential material for information protection in the application domain. The authors suggest that PUFs are commonly found in cyber-physical systems, and using this type of PUF could add security features without the need for expensive new hardware [2].

Since attackers can affect sensing technology, it is first necessary to analyze potential threats and identify ways to protect the information flow in the application area.

Biosensors handle confidential information, which must be protected against potential attacks. Therefore, it is crucial to review the threats that can be detected in sensors used in medicine and its devices. Security violators can be divided into two main categories: active and passive. A passive attack can only listen on a channel and

therefore gain access to messages. Assuming that the radio channel is insecure, a passive attacker poses a direct threat to confidentiality and can threaten authentication. A passive attacker (Fig. 1.1) can determine whether a person carries an implant, find out what type of implant it is, and capture other details such as its model, serial number, etc. They can also disclose private information about the patient, such as their health record ID, name, age, condition, etc. In contrast, an active attacker (Fig. 1.1) can capture the messages exchanged over the radio channel and send commands to modify outgoing messages before they reach the device. Attacks can involve multiple interceptions, modifications, and message generation. The attacker may also try to change the configuration of the device, disable the treatment, or even put the patient into a state of shock [5].



**Fig. 1.1** Types of attackers and attack information

Another approach that biosensors are currently interested in is biometric data. One way to identify individuals is to measure the concentrations of three metabolites in their perspiration. The metabolites lactate, urea, and glutamate are the focus of each of the three enzymatic assays used in this investigation. The enzymes urease and glutamate dehydrogenase are used in the urea assay. Only glutamate dehydrogenase is utilized in the last glutamate assay. These assays can be evaluated spectrophotometrically using the redox dye LOx/HRP or the conversion of NADH and NAD<sup>+</sup> in the other two [6].

Though more studies are required to make biometrics a dependable method of authentication using biosensory techniques, the use of sweat materials for biometric applications is growing. When used for authentication, other metabolites should be tracked simultaneously for enhanced security, especially for higher-security and cybersecurity systems. This tracking procedure would benefit current fields like clinical diagnostics as well as upcoming biometric research. Biosensors are increasingly being used in cybersecurity. New cryptographic techniques and the use of sensors for personal authentication have emerged recently.

Before that, the paper provides an overview of the implementation of a versatile wearable biosensor designed to continuously monitor individual sweat metabolites for

authentication purposes. Monitoring these metabolites can provide output data that would be useful in determining the authentication of an individual for multiple cybersecurity applications. The data obtained during the colorimetric tests are used to encrypt the message. If the recipient of the message performs the same experiment under the same conditions, the message will be correctly deciphered. Data from these enzymatic assays act as “keys” that can be used to lock and unlock data associated with encryption.

The future of user authentication, cryptography, and non-traditional computing may be significantly impacted by this brief fusion of biosensors and cryptology. For user authentication, which is just as crucial as, if not more crucial than, data protection via encryption, the procedures outlined here can be integrated with biometric information [6].

Ceramic-based PZT and polymer PVDF-based transducers generate a voltage proportional to the applied mechanical stress, force, or pressure. Piezoelectric transducers mounted in a cantilever position oscillate under mechanical force, producing an electrical output signal that oscillates at the resonance frequency of the inverter. Resistance measurement curves for each transducer show the lowest resistance at series resonance and highest impedance at parallel resonance, which are unique to each converter. A simplified resonator circuit can simulate this, with the impedance response measured using an impedance analyzer to extract the resonance frequencies. Thermal and polarization noise contribute to the output noise signal from piezoelectric transducers. A weak, low-amplitude vibration signal applied to the inverter generates this noise. The transducer’s output, ranging from microvolts to millivolts, is amplified by an external circuit. This amplified signal is then sampled or recorded for statistical analysis. A shaker provides low-level excitation, while the piezoelectric transducer outputs a noisy signal. The noise signal combines applied vibration, noise sources, and voltage fluctuations from the pyroelectric effect in PZT and PVDF converters. Shielded cables minimize external noise, but the connections remain susceptible. Preliminary data analysis indicated that resonance frequency measurements could be potential PUF candidates. Samples placed in a heat chamber had their resonance frequencies measured at temperatures ranging from 25 °C to 150 °C [7].

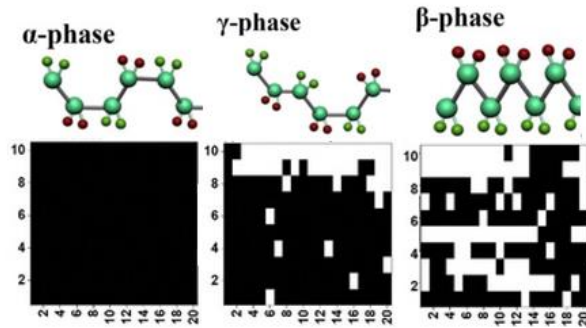
PUF is a lightweight hardware security primitive for devices that shows promise. Depending on process modifications that unavoidably take place during chip production, it can produce non-cloneable replies. PUFs can be classified as internal or non-internal based on whether further hardware design is needed. While intrinsic PUFs don’t require any changes to the current hardware, non-essential PUFs—like ring oscillator and arbiter PUFs—need extra hardware circuits to carry out the PUF function. One such example of an internal PUF is the cryptographic root key (SRAM PUF). The initial state of the enabled SRAM cells determines its responses. Nevertheless, the challenge-response pair (CRP) space is constrained due to the poor SRAM PUF. An further common PUF is the internal processor-based PUF, which generates PUF replies by employing delay variability in the data pathways and control paths in the microprocessor pipeline and challenges with central processing unit (CPU) commands [8]. PUFs, a type of hardware-based security primitives that take

advantage of the distinct physical properties of electronic devices to generate random and unexpected cryptographic keys, are the most promising choice [4]. A ring oscillator PUF is a device consisting of an odd number of NOT gates that produce an oscillating output between two voltage levels. Each NOT gate contributes to the delay in the output signal, where the output frequency depends on the entire ring delay line oscillator. The delay occurs due to manufacturing differences in NOT gates. A PUF will be produced since each NOT gate will be practically random, as will the ring oscillator's output frequency. A more intricate setup is needed for an optical PUF. The glass, a translucent substance infused with light-scattering particles that produce a distinctive stain pattern when activated by a laser beam, is exposed to the laser. The orientation of the laser beam on the transparent material causes the dot pattern to shift in both location and angle. The stain pattern in the output will differ between two similar transparent materials if their doping levels vary, even when the laser beam is focused on the same spot at different angles. The inductor-capacitor (LC) PUF consists of two metal plates and a metal coil, forming a passive LC circuit. Due to the influence of metallic materials on capacitance and inductance, similar-looking systems will exhibit different resonance frequencies when a frequency sweep is performed in an LC circuit. It is challenging to ensure identical values for the container and inductive materials because of manufacturing discrepancies. Computer methods are used in pseudo-random number generators, and noise sources are used in hardware random number generators [7].

PUFs are crucial in information security for identification, authentication, and key generation in device authentication and anti-counterfeiting. They generate unique keys from physical modifications that are hard to replicate due to high entropy. Metal oxides like amorphous indium gallium zinc oxide (a-IGZO) are promising for PUFs due to large-area synthesis and low-temperature processing but require engineering to add randomness as they usually have uniform properties [7]. Thin-film transistors (TFTs) offer parameters like carrier mobility, threshold voltage, and on/off-state current that are essential for PUFs, enabling multi-factor authentication and securing individual apps with unique security keys. Hardware-based PUFs offer strong defenses against side-channel and machine-learning threats when used with software solutions [7].

PVDF-HFP induces irregular electrical properties in a-IGZO semiconductors and is soluble in organic solvents like N-methyl-2-pyrrolidone and DMF. It contains fluorine and hydrogen, with short carbon-fluorine bonds and high bond energy. The presence of HFP units increases solubility compared to other PVDFs, with PVDF-HFP having the highest fluorine content. It can transform into  $\alpha$ -,  $\beta$ -, and  $\gamma$ -phases. As a thermoplastic, PVDF undergoes phase transitions during annealing, affecting electrical characteristics through dipole interactions. PVDF and its derivatives find uses in TFTs, sensors, batteries, and more. Its phase transition properties are valuable for PUF devices needing high-entropy electrical attributes [7]. PVDF-HFP changes into  $\alpha$ -,  $\beta$ -, and  $\gamma$ -phases, with the  $\beta$ -phase enhancing the dipole moment due to aligned C-F bonds [7]. Non-polar  $\alpha$ - and  $\gamma$ -phases maintain balanced electrical properties through zigzag hydrogen and fluorine arrangements. The VON range varies due to interfacial dipole effects, with the  $\beta$ -phase showing the largest, unpredictable VON

distribution in PVDF-HFP a-IGZO TFTs. Hardware safety relies on local dipole moments.  $\beta$ -phase devices showed a significant 37 V  $\Delta$ VON and the largest VON distribution, roughly 50% more than pristine a-IGZO TFTs, whereas  $\gamma$ -phase had smaller VON dispersion [7]. Digital values formed a QR code-like security key. Low VON values in  $\alpha$ -phase devices stem from limited dipole doping, primarily in the 0 state. The  $\beta$ -phase contained mixed 0 and 1 states due to uneven polar dipole distribution, while the  $\gamma$ -phase was more predictable. PUF device security was evaluated by uniformity and inter-HD, with inter-HD measuring output string differences, affirming phase randomness in PVDF-HFP-doped a-IGZO TFTs. The  $\beta$ -phase showed a 49.79% inter-HD, indicating potential for highly unpredictable keys [7]. The digitally segmented values were used to create a security key that resembles a QR code, as shown in Fig. 1.2.



**Fig. 1.2** Security key based on phase transitions in  $\alpha$ -phase,  $\beta$ -phase, and  $\gamma$ -phase

To determine if an attacker can detect a pulse, it is necessary to find out the methods that are used to detect the information. Therefore, several scanning methods are presented to help assess the scope and accuracy of information detection. Port scanning is a method used to determine open ports on devices in a network. This information can provide attackers with opportunities to identify and exploit weaknesses in the target system [9]. For instance, an open port on a patient monitoring device can allow attackers to infiltrate the system and manipulate patient monitoring data [27]. Using the Nmap tool in the model, information such as IP addresses, MAC addresses, used ports, and many other details about devices in the network were obtained. This information was a significant step in identifying and closing security vulnerabilities in the system [28]. The scanning results are shown in Fig. 1.3.

```
(root@kali)~# nmap 192.168.43.0/24
Starting Nmap 7.94SVN ( https://nmap.org ) at 2024-06-06 04:16 EDT
Nmap scan report for 192.168.43.1
Host is up (0.010s latency).
Not shown: 999 closed tcp ports (reset)
PORT      STATE SERVICE
53/tcp    open  domain
MAC Address: 22:A3: (Unknown)

Nmap scan report for 192.168.43.61
Host is up (0.00036s latency).
Not shown: 993 filtered tcp ports (no-response)
PORT      STATE SERVICE
80/tcp    open  http
443/tcp   open  https
1801/tcp  open  msq
2103/tcp  open  zephyr-clt
2105/tcp  open  eklogin
2107/tcp  open  msq-mgmt
3306/tcp  open  mysql
MAC Address: 18:67: (Samsung Electronics)

Nmap scan report for 192.168.43.250
Host is up (0.0062s latency).
All 1000 scanned ports on 192.168.43.250 are in ignored states.
Not shown: 1000 closed tcp ports (reset)
MAC Address: 68:C6: (Espressif)

Nmap scan report for 192.168.43.135
Host is up (0.0000890s latency).
All 1000 scanned ports on 192.168.43.135 are in ignored states.
Not shown: 1000 closed tcp ports (reset)

Nmap done: 256 IP addresses (4 hosts up) scanned in 49.66 seconds
```

Fig. 1.3 Nmap scan

Distributed Denial of Service (DDoS) is a type of Denial of Service attack carried out by sending an excessive amount of traffic from multiple sources to a target system or network. These attacks are typically orchestrated through a group of devices or computers controlled from a large network [62]. Especially in the healthcare sector, DDoS attacks can prevent monitoring of patient’s health conditions, hinder access to healthcare services, and impede timely emergency interventions [30]. In the created model, as seen in Fig. 1.4, after the DDoS attack was initiated, the system froze and empty packets from different IPs were observed. Additionally, it was observed that data transmission to the patient monitoring system was not possible due to the system being overwhelmed.

```
(root@kali)~# hping3 -C 100000 -d 120 -S -w 64 -p 1020 --flood 192.168.43.250
HPING 192.168.43.250 (wlan0 192.168.43.250): S set, 40 headers + 120 data bytes
hping in flood mode, no replies will be shown

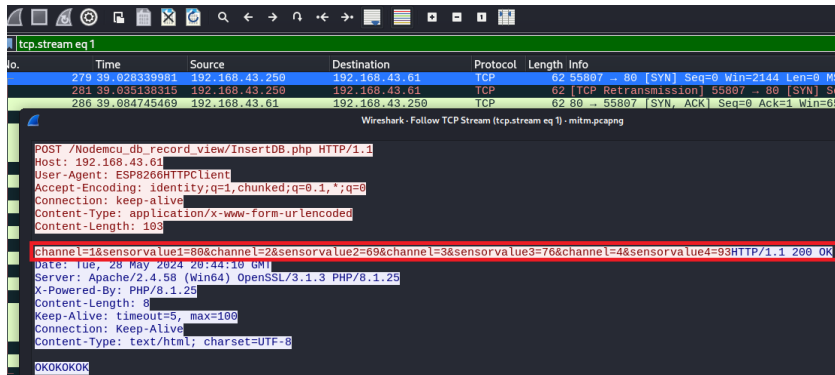
(root@kali)~# ping 192.168.43.250
PING 192.168.43.250 (192.168.43.250) 56(84) bytes of data:
64 bytes from 192.168.43.250: icmp_seq=1 ttl=255 time=7.68 ms
64 bytes from 192.168.43.250: icmp_seq=2 ttl=255 time=6.77 ms
64 bytes from 192.168.43.250: icmp_seq=3 ttl=255 time=8.48 ms
64 bytes from 192.168.43.250: icmp_seq=4 ttl=255 time=6.19 ms
64 bytes from 192.168.43.250: icmp_seq=5 ttl=255 time=8.27 ms
64 bytes from 192.168.43.250: icmp_seq=6 ttl=255 time=1006 ms
64 bytes from 192.168.43.250: icmp_seq=12 ttl=255 time=220 ms
64 bytes from 192.168.43.250: icmp_seq=14 ttl=255 time=222 ms
64 bytes from 192.168.43.250: icmp_seq=15 ttl=255 time=880 ms
64 bytes from 192.168.43.250: icmp_seq=16 ttl=255 time=1009 ms
64 bytes from 192.168.43.250: icmp_seq=19 ttl=255 time=784 ms

No.      Time           Source           Destination      Protocol
21885 47.609077866 95.237.110.162   192.168.43.250   TCP
21886 47.609127747 186.153.117.229  192.168.43.250   GnuteL...
21887 47.609160877 165.134.187.164  192.168.43.250   TCP
21888 47.609178236 232.33.232.207   192.168.43.250   TCP
21889 47.609190539 16.147.41.2      192.168.43.250   TCP
21890 47.609202418 62.139.47.13     192.168.43.250   TCP
21891 47.609222708 128.255.158.33   192.168.43.250   TCP
21892 47.609246391 46.94.245.217    192.168.43.250   TCP
```

Fig. 1.4 DDoS attack

A man-in-the-middle (MITM) attack is a type of attack that allows an attacker to intercept communication between two points and even manipulate it [31]. Such attacks can lead to serious consequences, especially in the healthcare sector, such as

theft or alteration of sensitive data [32]. For instance, through a MITM attack, data from patient monitoring devices can be altered, misleading healthcare staff and leading to incorrect treatments [33]. In the created model, as seen in Fig. 1.5, it was observed that sensors capture patient pulse data.



**Fig. 1.5 MITM attack**

Such attacks can jeopardize the security of vital data in the healthcare sector [34]. The theft or manipulation of sensitive patient data can lead to incorrect diagnoses and treatments, putting patients' lives at risk. Therefore, taking security measures to detect and prevent such attacks is of critical importance [36]. Especially to ensure the security of devices and healthcare systems, various measures should be taken. Continuous updates and patches, security firewalls, anomaly detection systems, encryption methods, and secure communication protocols are among these measures [54].

### 1.1.1. Evaluation of data protection for wearable and implantable biosensors

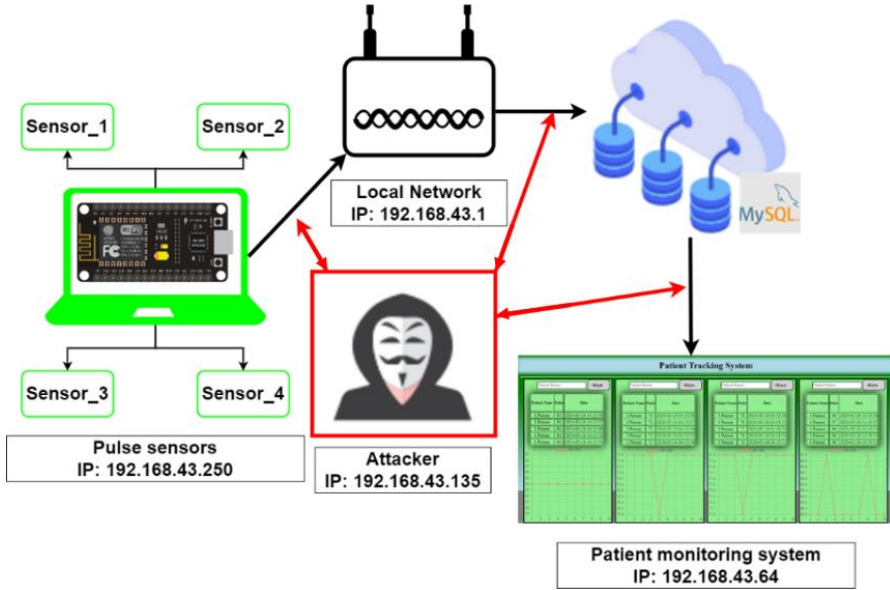
Biosensors handle confidential information, which must be protected against potential attacks through methods that enable identification of the pulse information stream. Since attackers can affect sensing technology, it is essential to first analyze potential threats and find ways to protect the information flow in the application domain. Information retrieval, search methods, and best practices in the targeted application area will be examined.

The patient tracking system is an important technology used in the healthcare sector. The network topology in Fig. 1.6 illustrates the organization of the patient tracking system and the integration of sensors. These sensors measure patients' pulse values and transmit the data over the network. The network topology shows how sensors communicate with the patient tracking system and how the data is transferred. A MITM attack can detect information at the three points highlighted in red in the image. The attacker can not only detect but also modify the information and send it back, replacing it with the desired information.

The sensing method offers a technical advantage over signal monitoring by transmitting the targeted information to a readable output. A passive attacker directly threatens confidentiality and could jeopardize authentication if the radio channel is insecure. Such an attacker can determine if someone has an implant, identify its type,

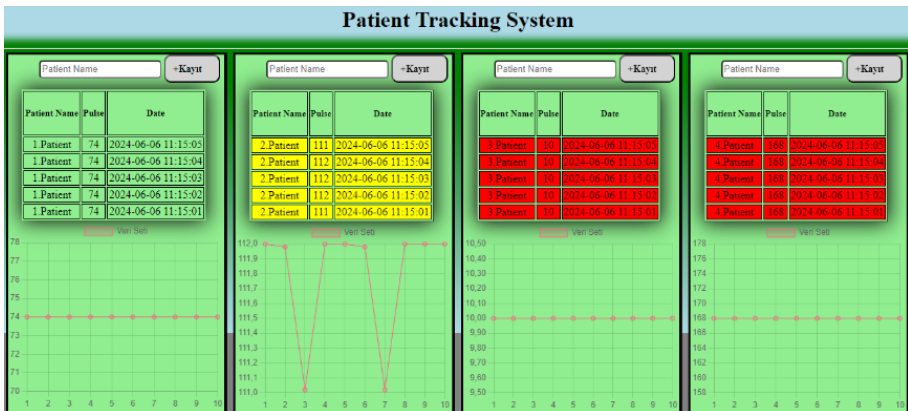


and retrieve other parameters, such as the model and serial number. They can also access additional information and expose personal data about the patient, including their name, age, condition, health record ID, and other details. In this scenario, an active attacker can transmit commands to alter the messages delivered before they reach the device in addition to intercepting the messages sent over the radio channel. Since this can affect not only personal information but also the range of treatments or applications, it is crucial to safeguard such data from potential risks [5].



**Fig. 1.6** Network topology

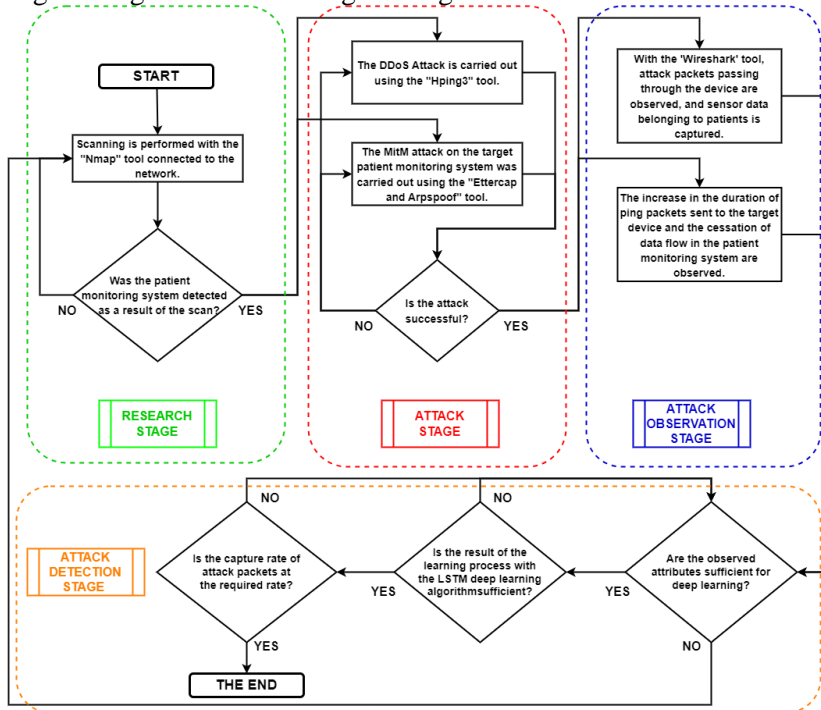
The interface of the patient tracking system consists of the tables and graphs shown in Fig. 1.7. These tables and graphs display the pulse values of patients, allowing for simultaneous measurement of pulse values for four patients. A sensor is attached to the patient's wrist for pulse measurement, and once the sensor is in place, pulse data is sent to the patient tracking system.



**Fig. 1.7** Interface of the patient tracking system

When the system is started, the sensor value is transmitted to the computer environment via the TCP communication protocol, and the transmitted value is added to the database. Using the MySQL database, the time of each incoming value, pulse rate, and patient name are recorded. These data are displayed in both the table and the graph showing the values indicated by the pulse sensors to which the patients are connected. The system measures the pulse rate once per second, transmits these data to the system, and ensures they are displayed. The table turns yellow when pulse values exceed normal ranges, indicating that the patient's pulse has either decreased or increased. However, when pulse values are extremely high or low, the table turns red, indicating that the patient's pulse rate is at a risky level and requires urgent intervention.

When examining Fig. 1.8, the flow diagram, it is observed that the system consists of four fundamental stages. The sections related to the attack encompass the reconnaissance, attack, and observation stages. However, to actively rescue the system from attacks as soon as possible, focusing on a passive attack like MITM, which is the focal point of the study, and to prevent information disclosure, an attack detection stage through artificial intelligence algorithms has been added.



**Fig. 1.8** Attack flow diagram

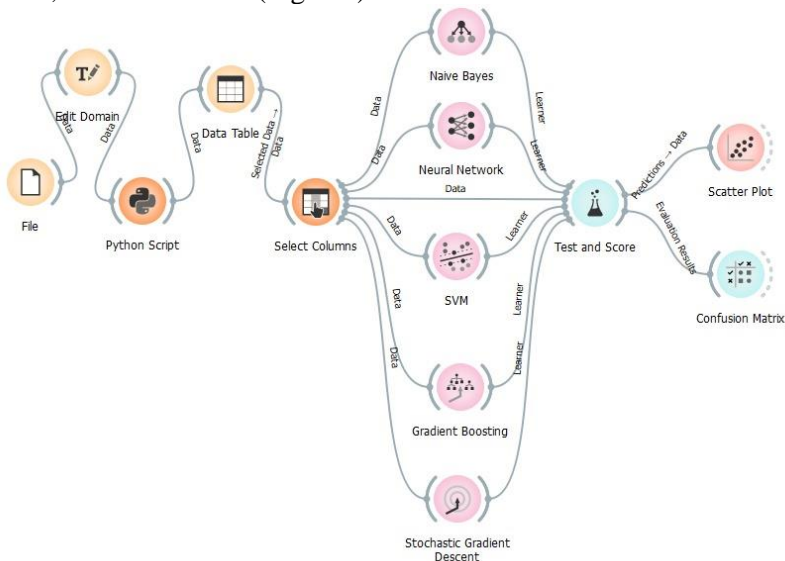
In the first stage, the network was generally scanned, and after determining the target system, brand model information was verified to confirm whether this target system was actually on the network. As shown in the flow diagram, two separate attacks (DDoS and MITM) were then carried out on the identified target system. The effects of these attacks on the system were observed in the third stage. During the

DDoS attack, an increase in packet durations was observed, while in the MITM attack, duplicate packets were received via Wireshark, and entries were made into the tables of the victim devices.

In the final stage of attack detection, packets obtained with Wireshark were used to first add abnormal network packets and those classified as attacks into the system through machine learning. After machine learning was completed, the success percentage of attack packets was examined with the packets in the training set. The evaluation revealed that attack packets were detected successfully with a success rate of 98%.

Today, technologies used in the healthcare sector play a critical role in monitoring and managing patients' health conditions. However, the increased use of these technologies has made them more vulnerable to cybersecurity threats. The security of health data is of paramount importance, both for protecting patient privacy and ensuring accurate treatment processes. In this context, examining cyberattack types and security measures against these threats is essential for ensuring the security of healthcare systems. Below are the vulnerability analyses of the attacks conducted in the model.

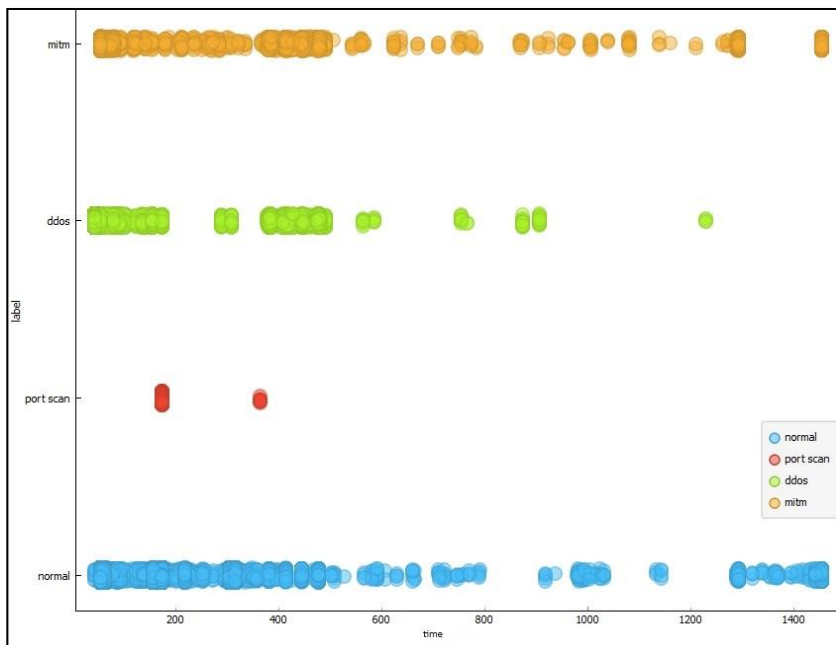
Network traffic attack detection was performed using artificial intelligence algorithms. The detection model consists of four steps. First, to improve algorithm accuracy, network traffic data was preprocessed into a suitable dataset and split into 10-millisecond pieces. Second, 30% of the dataset was used for validation, while 70% was used for training. Ten-fold cross-validation was used to analyze several algorithms, including Support Vector Machine, Gradient Boosting, Neural Networks, Naive Bayes, and Stochastic Gradient Descent (SGD). Third, to gain a better understanding of algorithm performance, visualization approaches were employed. Ultimately, SGD was chosen for real-time attack detection due to its superior accuracy, recall, and time values (Fig. 1.9).



**Fig. 1.9** Attack detection using artificial intelligence algorithms

Artificial neural network-based SGD efficiently analyzes data and discovers patterns, which makes it helpful for intrusion detection. It is composed of linked neurons in multiple layers. Data is delivered into the input layer during training, and error values are calculated by comparing the output. SGD iterates over tiny, randomly chosen portions of the dataset, enabling quick, effective training. These errors are transmitted backward to change the network's weights and biases. SGD can detect intrusions with high accuracy by learning intricate patterns in large datasets. SGD was the best technique for intrusion detection in real-time data, with the highest accuracy and time performance in comparison evaluations.

In the second phase, machine learning and artificial intelligence algorithms were used to parse packets and analyze attacks. 70% of the training data for the system was derived from captured packets, which were categorized as either normal or attack. 30% of the validation data was subjected to different methods following classification. It was not enough to evaluate accuracy alone; other important parameters included precision, memory, and test time. The system picks up data definitions without any problems during training, but test time—the speed and precision of identifying incoming packets—is crucial. SGD was chosen for the expert system due to its better success rate and faster test time, even though its accuracy rates were comparable. SGD demonstrated the best success percentage and the quickest test time. Attacker packet traces were tracked and shown in red to indicate attacks, while the network traffic of source hosts (Fig. 1.10) (Y-axis) was assessed over time (X-axis). Attack detection techniques successfully identify attacker activities and distinguish attack packets from regular traffic, as seen by the visual detection of these packets in the reference model without attackers.



**Fig. 1.10** Detection of attackers using the artificial intelligence model

These findings highlight the importance of robust security measures in patient tracking systems. Effective attack detection ensures the security of healthcare data, protecting patient privacy and treatment accuracy. Measures include continuous updates, security firewalls, anomaly detection systems, encryption methods, and secure communication protocols.

## **1.2. Types of sensors**

There are several types of technological sensors, thus this section examines those used not only for medical purposes but also in other areas of application.

Biosensors can often use nanoparticles to detect and amplify various signals. These biosensors have developed functional nanoparticles (electronic, magnetic, and optical) coupled with biological molecules. In addition, there are nanoparticle-based sensors, such as optical biosensors, magnetic biosensors, electrochemical biosensors, and acoustic wave sensors [10, 11]. Other action-based sensors are also frequently used, such as vibration, force, and dynamic mode mechanical biosensors as well as various mechanical surface sensors. These sensors work by converting changes in pressure, acceleration, temperature, strain, or force into an electrical charge that can be detected and measured.

Accelerometer sensors are extensively used in consumer electronics, automotive, and aerospace industries to measure acceleration and track motion, shocks, and vibrations. An accelerometer is a device that measures continuous static force or dynamic vibration and motion, with vibration, shock, motion, and earthquake being various forms of acceleration that can be measured. Accelerometers can be classified as piezoresistive, capacitive, piezoelectric, or resonant based on several sensitive components.

In contrast to other sensor types, piezoelectric accelerometers are characterized by their wide frequency band, large range, simple structure, consistent performance, strong output linearity, etc. Their structure primarily consists of a base, a mass block, and a piezoelectric-sensitive element. When a particular acceleration is applied to an object, the accelerometer is affected. The inertial force opposing the device's acceleration causes the piezoelectric element to bend as the mass block operates. This results in a potential difference when the two surfaces of the piezoelectric element amass equal quantities of opposing charges due to the piezoelectric effect [12].

Typically, a piezoelectric element consists of two piezoelectric sheets. After placing a mass with a higher specific gravity on top of the piezoelectric sheet, the mass is preloaded using a stiff spring, bolt, or nut. The piezoelectric sheet generates alternating charges (voltage) on both sides of its surface as a result of its piezoelectric effect. The output charges of the sensor are proportionate to the applied force, or the acceleration of the specimen, when the vibration frequency is significantly lower than the fixed frequency.

Common applications for piezoelectric pressure sensors include environmental monitoring, medical equipment, and industrial processes. Flexible piezoresistive pressure sensors use the piezoresistive effect to transform changes in pressure into a shift in the resistance of the sensing material. To create a configuration, the sensitive layer can be positioned between two electrodes that are vertically aligned or in the

same plane as the connected electrodes. The sensitive layer of a structured sensor, for instance, must create several ant-paths for effective charge transfer and flexibility to adjust to various mechanical deformation processes. Due to the limited internal conductivity of polymers, the conducting function components often comprise additional conductive phases, such as carbon nanotubes, carbon black, graphene, MXene, gold/silver, and other conductive materials [13]. Force measurement sensors are used in robotics, medical devices, industrial machinery, scales, and other fields. A sensor that uses piezoelectric elements to directly convert force and electricity is known as a piezoelectric force sensor. Due to its high sensitivity, linear response, and low cost, the piezoelectric force sensor is one of the most popular sensors in force measurement applications. Piezoelectric sensors effectively use the direct piezoelectric effect to transform dynamic forces into electrical signals. It is common practice to use two or more functional elements as piezoelectric elements for both pulling and pressing. These sensors offer high linearity and stability, good dynamic characteristics, a large measuring range, and high rigidity [14].

Numerous machines and structures may sustain damage due to vibrations, which can hasten aging and wear. In industrial applications, vibration sensors help detect faults and perform predictive maintenance by tracking vibrations in structures and machinery. Various methods for detecting vibrations have been developed thus far. The majority of vibration sensors use indirect vibration measurement. For instance, many small vibration sensors measure acceleration, whereas seismometers typically measure velocity. The most common methods for measuring vibration are piezoelectric or electromagnetic transducers.

Vibration sensors are frequently used because of their ability to detect high-frequency inertial forces, whereas accelerometers must react to direct current. In certain situations, piezoelectric accelerometers can be employed as vibration sensors due to their broad operating frequency bandwidth. Piezoresistive, capacitive, tunnel, optical, and piezoelectric sensors are among the many detection methods that have been developed for vibration sensors. Compared to piezoresistive and capacitive devices, piezoelectric transduction offers superior linearity, long-term stability, and temperature stability [15].

Using the direct piezoelectric mode, one of the most popular operating principles is force sensors or multiple configuration sensors [10, 11].

### **1.3. Piezoelectric composites**

The piezoelectric effect is commonly used in sensors, and the most popular materials with this property are reviewed below. Since polymer/ceramic composites are widely used and discussed, the composites with this composition that have already been developed and studied will also be reviewed below.

Piezocomposites are used in the majority of piezoelectric materials. Due to their excellent mechanical qualities, piezoelectric polymers—such as poly(L-lactide) (PLLA), poly(vinylidene fluoride) (PVDF), poly(vinylidene fluoride trifluoroethylene) (P(VDF-TrFE)), polyimides (PI), polyacrylonitrile (PAN), and others—constitute the majority of organic piezoelectric materials. These materials are frequently utilized in flexible sensors. The most common organic piezoelectric

material is PVDF, which is lighter and more adaptable than piezoelectric ceramics. Therefore, they offer advantages over piezoelectric ceramics in various applications, as they can be integrated into thin films of any required shape [16, 26]. To improve the performance of piezoelectric polymer sensors, piezoelectric composites have been developed using various common inorganic piezoelectric materials, including PZT and ZnO. While piezoelectric polymers have good mechanical properties, their low piezoelectric coefficients limit sensor performance. The development of inorganic piezoelectric materials involves enhancing their piezoelectric characteristics. These materials include piezoelectric films, ceramics, and single crystals [16, 26].

Pb [ZrxTi1-x] O<sub>3</sub>, also known as lead zirconate titanate (PZT), is the most commonly used piezoelectric ceramic. One of its primary drawbacks is that PZT contains over 60% lead (Pb) by weight. Currently, no suitable lead-free piezoelectric materials have been developed, as no composition has been found that exhibits PZT-like characteristics. Barium titanate was among the first practical materials to use piezoelectrics. Despite its low piezoelectric constant, this material's conductivity is exceptionally high [16, 26]. Lead magnesium niobate-lead titanate (PMN-PT) and lithium niobate (LiNbO<sub>3</sub>) are also frequently utilized in piezoelectric materials. Biocompatible ceramics, such as KNbO<sub>3</sub>, NaNbO<sub>3</sub>, etc., can be employed in various sensors [19].

The benefits of HA and PVDF  $\beta$ -phase composites were also analyzed. The comparison of the stimuli-responsive properties of PVDF fibers suggests that solution-blowing spinning resulted in a higher fiber production rate than electrospinning and more  $\beta$ -phase in the fibers produced [21].

Ag/C particles were uniformly distributed throughout the PVDF matrix, which affected the crystallization process and dielectric characteristics of the Ag/C/PVDF composites. The crystallinity of the composites decreased as the quantity of Ag/C particles increased. As the Ag/C particle content increased, the transmittance of the Ag/PVDF composites also increased due to improved interfacial polarization. Thus, Ag-containing composites enhance PVDF  $\beta$ -phase behavior in addition to the electrical characteristics [22].

An Ag-NBCTO-PVDF composite was created, and the results demonstrated that Ag nanoparticles were crucial in increasing the dielectric permittivity of the material. The benefits of introducing the silver phase into the Ag-NBCTO-PVDF composite were also observed [115].

The PVDF films were prepared using a traditional rod-coating method [82]. DMF was combined with concentrations of biochemical oxygen demand (BOD) and water, and the mixture was heated to 100 °C for 9 hours. After the solution cooled to room temperature, PVDF was added at a weight percentage of 10% and heated for an additional 2 hours at 60 °C. Finally, rod coating was used to prepare the PVDF films at approximately 100 °C. The prepared PVDF/BDS solution remained stable without affecting the morphology or quality of the resulting films and could be stored for an extended period [82].

A PVDF solution, containing water and a small quantity of BOD, was used to cast  $\beta$ -phase PVDF films. During the thermal breakdown process, H<sub>2</sub>SO<sub>3</sub> is produced in situ and is spontaneously eliminated during the coating phase. A large  $\beta$ -phase ( $\beta$

= 95%) was successfully generated in PVDF by  $\text{H}_2\text{SO}_3$ . As a result, PVDF/BDS films showed excellent ferroelectric and piezoelectric characteristics without requiring mechanical stretching or an extended thermal annealing process. The author's simple and efficient method for synthesizing  $\beta$ -phase PVDF has various applications, including transducers, energy harvesters, electrochemical sensors, and other electronic devices [82]. Studies using PVDF/HA as control targets have been conducted. For example, a PVDF/HA composite was used to stop heavy corrosion of 316L stainless steel, resulting in good matches of electrochemical corrosion parameters. Additionally, the HA adsorption efficiency of hybrid PVDF membranes was investigated, and the results showed an acceptable range of adsorption ratios [70].

Furthermore, the deposition of HA using the PVDF polymer process on commercially pure titanium surfaces was examined using modified laser beam irradiation [29]. Another study described the use of PVDF/HAP composites for medical applications [23]. The evaluation of the bioactivity of HA nuclei with PVDF composites in a solid film mode was also reported [24]. All research on PVDF/HA composites indicates that the PVDF coating on the composite's surface did not facilitate the coating process. Therefore, a major challenge in applying piezoelectric PVDF is enhancing the hydrophilicity and electrical properties of the coating.

Another composite example provided is the PVDF/Ag/BaTiO<sub>3</sub> composite made by casting. Compared to conventional PVDF/BaTiO<sub>3</sub> composites, the composite containing silver particles exhibits superior dielectric properties. The dielectric constant of the PVDF/Ag/BaTiO<sub>3</sub> composites significantly increases as the amount of Ag increases [75]. Additionally, the findings demonstrate that electrodynamics affects the kinetics of apatite growth. A reverse piezoelectric effect can be achieved in bone implants by using the developed HA $\beta$ -PVDF composite [76].

Overall, a brief comparison of some related previous studies and their performances is presented in Table 1.1.

**Table 1.1** Comparison of piezoelectric composites

Sample	Short explanation	Ref.
HA/PVDF	The HA content ranges from 0% to 15%. The $d_{33}$ constant decreased from 2.61 pC/N to 1.08 pC/N, while the $d_{33}$ value increased to 1.53 pC/N as the HA content grew to 20%. The addition of HA altered the amount of $\beta$ -PVDF, and, consequently, the piezoelectric performance of the HA/PVDF composite.	[3]
PVDF/HA (60:40)	According to reports, the stress was $459.2 \pm 4.1$ MPa, and the deformation was 0.23 mm.	[4]
PVDF-hydroxyapatite composite	Piezoelectric scaffolds were created using polyvinylidene fluoride (PVDF) as a polymer matrix, and the formation of the PVDF piezoelectric phase was studied. To create multifunctional composite membranes with bioactive qualities, HA particles at the micro and nanoscale were added to this matrix as a dispersed phase. The results show that membranes containing composite micro and nanofibers can be produced by electrospinning. HA	[3]



	particles exhibit good dispersion in the polymer matrix and predominate PVDF $\beta$ -phase.	
PVDF-BaTiO <sub>3</sub> -Ag	Upon applying a 1.2 N force at a 5 Hz frequency, the fibers demonstrated an increase in output voltage (1.78 (12) mV) in comparison to pristine PVDF and PVDF-BaTiO <sub>3</sub> composite fibers (1.48(26) mV).	[17]
PVA/AgNO <sub>3</sub>	A set of samples dried at 25 °C showed the highest antibacterial properties. The antibacterial activity of the examined samples was attributed to the silver ions produced when the samples dissolved in water.	[63]
PVDF in DMSO solvent	When DMSO was used as the solvent at an ideal crystallization temperature of 60 °C, PVDF films with a $\beta$ -phase content of up to 98.8% were produced.	[67]
PVDF/NaY zeolite composites	A comparison of solvents, such as DMSO and DMF, revealed a significant variance in the dielectric constant.	[111]
PVDF/GO imprinted composite	Out of all the samples examined, the PVDF composite containing 0.1 weight percent rGO exhibited the highest degree of crystallinity, the most electroactive phase, and the highest piezoelectric coefficient ( $d_{33}$ ). As a result, quenching enhanced the piezoelectric response, while the addition of rGO significantly influenced the domain orientation (polarization).	[110]
H-PVDF-PVA/GO-m-Ag membrane	Although the rejection efficiency of the H-PVDF-PVA/GO-m-Ag membrane was slightly lower compared to the H-PVDF-PVA/GO membrane, the uniform imprinting of Ag ions on the membrane surface can provide a membrane with excellent antimicrobial properties.	[101]
HA/PVDF coating on titanium surface	The titanium surface was coated with HA/PVDF, which demonstrated a piezoelectric effect. The hydrophilicity of the coating was enhanced by the addition of more HA. Corona polishing successfully reduced the contact angle and imparted piezoelectric properties to the HA/PVDF coating. Moreover, the contact angle of the polarized HA/PVDF coating decreased by 66.9%. The introduction of HA and the high piezoelectric coefficient promotes the mineralization of the coating.	[38]
PVDF/AgN O <sub>3</sub> conductive membrane	The optimal conductivity, dissipation factor, and dielectric constant were achieved by mixing 0.6 g of AgNO <sub>3</sub> with PVDF. The presence of AgNO <sub>3</sub> significantly increased the conductivity of membranes.	[112]
HA/PVDF	The HA content ranges from 0% to 15%, which reduced the $d_{33}$ constant from 2.61 pC/N to 1.08 pC/N. When the HA content reached 20%, the $d_{33}$ value increased to 1.53 pC/N. The addition of HA altered the amount of $\beta$ -PVDF, thereby affecting the piezoelectric performance of the HA/PVDF composite.	[113]

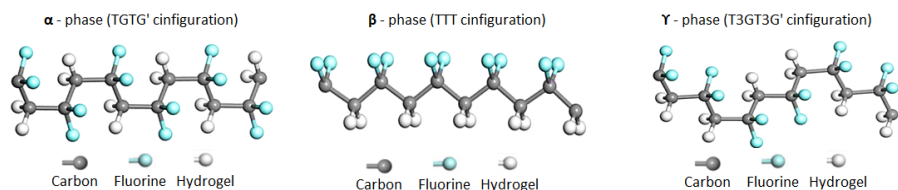
PVDF-HFP/CB/GO film	After creating PVDF-HFP/CB/GO composite films, Cai et al. discovered that the hybrid fillers could successfully encourage phase transition during the early stages of crystallization. The maximum output voltage and harvested power density of the films were 181% and 329% of the neat PVDF-HFP films, respectively, resulting in a higher $\beta$ -phase fraction at lower concentrations.	[114]
GO/PVDF nanogenerators	GO was added to PVDF to enhance its $\beta$ -phase content until the filler ratio reached 2 weight percent. The open-circuit voltage was 1.5 V, and the short-circuit current was 200 nA. When reduced at 140 °C, rGO led to the formation of a higher $\beta$ -phase, with the open-circuit voltage and short-circuit current increasing to 16 V and 700 nA, respectively, resulting in the most efficient power generation. The induced charge transfer produced by PVDF was further enhanced by the increased conductivity of rGO. By boosting the induced charge and $\beta$ -phase transfer of PVDF, rGO improved the piezoelectric response of the fiber, showing great potential for significantly increasing the power generation efficiency of nanogenerators.	[50]
PVDF in DMSO solvent	Phase characterization revealed that the highest $\beta$ -phase in the films was observed when PVDF was annealed at 90 °C for 5 hours.	[78]

After reviewing composites and materials used in piezoelectric sensors, nanogenerators, and energy harvesters, potential materials for developing the sensor are further explored.

### 1.3.1. Effects of PVDF $\beta$ -phase on piezoelectric sensor applications

Compared to piezoelectric ceramics, PVDF is the most widely used organic piezoelectric material due to its lighter weight and versatility. PVDF films with a 98.8%  $\beta$ -phase content are produced at the ideal crystallization temperature of 60 °C using DMSO as a solvent. The associated PVDF film exhibits exceptional ferroelectric and piezoelectric properties owing to its strong  $\beta$ -phase composition. Additionally, solvent casting can be used to create PVDF films. PVDF films can be produced at various crystallization temperatures (50–160 °C) using DMSO as the ideal solvent to evaluate the influence of temperature on  $\beta$ -phase content. DMSO, an aprotic solvent, is also miscible with polar liquids because of its dipole moment [77]. PVDF can be produced in all three phases using the same polar solvent. By adjusting the solution temperature with the polar DMSO solvent, several PVDF phases can be obtained. Additionally, annealing conditions can induce phase transitions leading to distinct PVDF phases. The  $\beta$ -phase is produced by a polar solvent and suitable annealing, which is necessary for ferroelectric applications. The PVDF films reach their maximal  $\beta$ -phase after annealing at 90 °C for 5 hours [78, 37]. The material PVDF is a viable choice for wearable, flexible, and implantable electronic sensors, nanogenerators, energy harvesters, artificial skin, and biomedical applications due to its mechanical and chemical stability, flexibility, non-toxicity, thermal stability, and biocompatibility. PVDF is dielectric, piezoelectric, ferroelectric, and pyroelectric.

As shown in Fig. 1.11, PVDF has three polymorphic crystalline modifications ( $\alpha$ ,  $\beta$ , and  $\gamma$ ), but only two constitute polar phases. The  $\beta$ -phase is the most preferred due to its highest electric dipole mobility. For PVDF to transition into the polar  $\beta$ -phase, its unique  $\alpha$ -phase must be treated. Typically, PVDF  $\beta$ -phase strengthening is achieved by heat treatment, mechanical stretching, electropolishing, and filler addition [37, 79, 80].



**Fig. 1.11** Molecular structure of PVDF and representation of its  $\alpha$ ,  $\beta$ , and  $\gamma$  phases

Using DMSO as a solvent during optimal crystallization produces PVDF films with a high  $\beta$ -phase content of up to 98.8% [78]. According to the XRD curve, the  $\beta$ -phase peak was at its highest when the PVDF film was annealed for 5 hours at 90 °C. The PVDF films exhibit their maximal  $\beta$ -phase after 5 hours of annealing at 90 °C. [73].

The  $\beta$ -phase with all-trans conformations (TTTT) offers the best piezoelectric characteristics. Polymeric fibers are created by rearranging molecules into the trans-conformation in a polymer solution. Numerous research have examined different  $\beta$ -phase enhancement values and the piezoelectric characteristics of PVDF fibers. For example, lowering the evaporation rate results in an increase in the amount of  $\beta$ -phase [17].

The  $\beta$  peak is seen in the PVDF film cast from the DMSO solvent, suggesting that the  $\beta$ -phase becomes the primary phase. The diffraction data show the trends of the  $\beta$ -phase in PVDF films when cast from a solvent with a greater dipole moment. During the  $\beta$ -phase transition, the molecular chain in the PVDF film transitions from its original  $\alpha$ -phase conformation TGTG to the TTTT conformation [77].

The impact of annealing on the conversion of  $\gamma$ -phase PVDF to  $\beta$ - and  $\alpha$ -phase PVDF was demonstrated. PVDF sheets were annealed in DMSO at 90 °C for 5 hours, resulting in  $\beta$ -phase conditions in the PVDF film. The presented data unequivocally demonstrate that the PVDF film's  $\beta$ - and  $\alpha$ -phases correlate with annealing temperatures of 70 °C for 5 hours, respectively. Thus, under these annealing circumstances, the PVDF film contains both the  $\beta$ - and  $\alpha$ -phases. After annealing, PVDF films display both the  $\beta$ - and  $\alpha$ -phases. Additionally, it has been confirmed that annealing at 110 °C for 5 hours is required. After 5 hours of annealing at 130 °C, PVDF films show both an increase and a decrease in the values of the  $\beta$ -phase in  $\alpha$ -phase content.

When PVDF is subjected to external mechanical force, it can generate a significant amount of power. PVDF is more practical than ceramics due to its remarkable flexibility and durability, making it a useful material for applications requiring tactile sensing or force feedback. Despite its many benefits, the primary obstacle to the restricted application of PVDF polymers is the challenge of reaching

the  $\beta$ -phase. If the polymer film is utilized as a functioning component of a device, this could become a significant issue [79].

### **1.3.2. Hydroxyapatite (HA) material**

Since ceramics exhibit good piezoelectric properties, HA is one of the potential materials. HA is an excellent material for biomedical applications due to its properties such as biocompatibility and piezoelectricity. This bioceramic compound, a form of calcium phosphate, is naturally found in human tissues in crystalline form and is the main inorganic mineral component of teeth and bones. Synthetic methods are widely used to produce HA, as synthetic HA exhibits a piezoelectric effect, making it suitable for detecting electromechanical signals. The synthesis of HA thin films is an effective way to produce sensors for technological applications [35].

Piezoelectric composites have been created using a range of popular inorganic piezoelectric materials, such as HA, to enhance the performance of piezoelectric polymer sensors. The produced HA exhibited low crystallinity and high porosity. HA derived from animal bones and calcined at 800 °C has the highest crystallinity. HA can develop a chemical link with the surrounding minerals once the HA interface layer has formed [4, 37].

HA, on the other hand, is a calcium phosphate with the chemical formula  $\text{Ca}_{10}(\text{PO}_4)_6(\text{OH})_2$ . It is extensively studied in bioceramics and is one of the most commonly used materials in biomedical and clinical applications because it closely resembles the crystalline phase of bone tissue. HA is an osteoconductive, biocompatible, bioactive, and thermodynamically stable material. When combined with biocompatible polymers such as PVDF, polylactic acid (PLA), polycaprolactone (PCL), etc., it becomes a material with great potential for composite development [3].

Considering that HA has good hydrophilicity and can form bone connections with bone tissue, HA/polymer composites can be prepared. The introduction of HA into the PVDF piezoelectric coating can improve the hydrophilicity of the coating and endow it with both the piezoelectric properties of PVDF and the good biocompatibility of HA [38].

HA is endowed with all kinds of morphologies, including three-dimensional HA nanoparticles. These nanoparticles have greater mechanical qualities, a higher specific surface area, increased adsorption capacity, and a larger pore volume, in addition to having a higher number of hydrophilic groups [67]. The synthesis of HA nanoparticles has been reported using several techniques, including heat treatment, hydrothermal, wet chemical sol-gel, and microwave methods [72, 69].

### **1.3.3. Graphene oxide (GO) material**

Graphene has very high mechanical strength, surface area, and thermal and electrical conductivity, making it a highly promising material for our composite. GO, a member of the graphene family of materials (GFMs), exhibits exceptional mechanical, electrical, optical, thermal, and biocompatible properties. According to studies, GO has antibacterial qualities through the processes of electrostatic adsorption, lipid peroxidation, oxidative stress, and physical isolation. However, its antibacterial properties have been extensively studied and mounting data indicates

that the antibacterial properties of pure GO are unstable and dependent on a number of variables, including structure, environment, temperature, and magnetic field. To overcome these factors, GO-based antibacterial composites can be developed by combining GO with components such as antibacterial agents and polymers. Compared with GO, the antibacterial properties of GO-based composites are more stable and excellent, as indicated by faster sterilization and longer duration of action [119].

Piezoelectric scaffolds composed of poly(3-hydroxybutyrate-co-3-hydroxyvalerate) (PB) and GO have been successfully fabricated using electrospinning technology. The fabricated scaffolds were investigated for their morphological, physical, chemical, piezoelectric, and biological properties. Reinforcement with 1.5% GO increased the tensile strength of PB to  $2.08 \pm 0.33$  MPa compared to PB alone ( $0.59 \pm 0.12$  MPa). GO reinforcement significantly increased the piezoelectric coefficient ( $d_{33}$ ), and PB of 0.5%, 1%, and 1.5% GO was found to be  $0.12 \pm 0.015$ ,  $0.57 \pm 0.19$ , and  $0.94 \pm 0.03$  pC/N, respectively. Voltages of  $11.84 \pm 1.4$ ,  $54.69 \pm 18.29$ , and  $100.2 \pm 3.2$  mV were generated, respectively [39].

The effect of GO/rGO on the electrical properties of the PVDF-(BZT-BCT) composite film was also investigated. GO and rGO composite films exhibit improved dielectric, ferroelectric, and piezoelectric properties. The composite film with an optimized GO concentration (0.16 wt%) has a conductivity of 25.6 (~2 times that of pure PVDF). The remanent polarization is improved by a factor of six, and piezoelectric deformation by a factor of three, making the composition ideal for piezoelectric energy harvesting purposes, such as artificial pacemakers and low-power electronics [40].

#### **1.3.4. Silver nitrate (AgNO<sub>3</sub>) material**

A conductive phase such as silver can be beneficial because it increases the sensitivity of the piezoelectric response, thereby improving the conductive phase charge transfer, which is a very important aspect in the design of piezoelectric composites. Silver nanoparticles (AgNPs) can be used as a PVDF filler to increase the amount of  $\beta$ -phase and as an antibacterial agent in industry or surgery. It was discovered that when the AgNP content was between 0.4% and 0.6%, the  $\beta$  content of PVDF increased by nearly 8%. The electrospun fibers exhibited increased overall crystallinity, tensile strength, and thermal stability, as well as a higher  $\beta$ -crystalline content and visible nanopores on their surfaces [41].

Silver ions (Ag<sup>+</sup>) released from silver nanoparticles (Ag<sup>0</sup>) interact with the phosphorus moieties of DNA. Silver nanoparticles are highly bactericidal, relatively harmless to humans, and non-toxic. Adding a conductive phase such as silver can be beneficial because, firstly, it improves charge transfer by increasing the sensitivity of the piezoelectric response, and the appropriate amount of Ag deposition enhances the piezoelectric activity, whereas higher Ag loading decreases it (concentration properties studied at 0.12%, 0.21%, 0.52%, and 1 mL) [20, 17]. Notably, the enhanced localized electromagnetic field of Ag nanoparticles (Ag NPs) can be rationally induced by pressing or bending the PVDF film to enable ultra-high sensitivity tuning [42].

## 1.4. Chapter conclusions

1. Biosensors are commonly used to measure a person's voice, breathing, heartbeat, brain or eye pressure, wrist pulse, and hand movements. In sensing technology, an attacker can not only capture messages but also send commands to change the information. This study examines the security vulnerabilities of the wireless infrastructure of piezoelectric biosensors used in the medical field. Additionally, solutions to correct the security flaws in the system are proposed. The integration of a PUF key into the PVDF  $\beta$ -phase, which does not require additional hardware to ensure security, is also investigated.

2. PVDF, as the main phase, is widely used due to its wide range of applications and piezoelectric properties. To compensate for the mechanical weakness of HA, several HA/polymer composites have been developed. The composition containing GO is well-suited for piezoelectric electronics, as it improves permanent polarization and piezoelectric deformation. Silver can be used as an antibacterial agent and as a PVDF filler to increase the  $\beta$ -phase content, thereby improving charge transfer and piezoelectric response. Composites consisting of PVDF, HA, GO, and  $\text{AgNO}_3$  have not yet been analyzed. Therefore, to improve the mechanical, electrical, and piezoelectric properties of the functional element under development, PVDF, HA, GO, and  $\text{AgNO}_3$  materials were selected along with a solvent annealing method.

3. Based on the literature review, PVDF, HA, GO, and  $\text{AgNO}_3$  materials were selected to create the functional element. The following objectives were set: to evaluate data protection methods and materials used in wearable and implantable biomechanical sensors; to synthesize a piezoelectric composite with  $\beta$ -phase transformation by incorporating HA, GO, and  $\text{AgNO}_3$  nanoparticles into PVDF; to evaluate the influence of HA, GO, and  $\text{AgNO}_3$  nanoparticles on the electrical, mechanical, and morphological properties of the piezoelectric composite, ensuring  $\beta$ -phase transformation; and to evaluate the possibilities for the application and integration of the functional element.

## **2. MATERIALS AND EXPERIMENTAL METHODOLOGY**

Measurement and application techniques are required to identify composite materials as viable for sensing applications. The first step is to measure the morphology, which is done using a scanning electron microscope (SEM). The current energy dispersive X-ray (EDX) peaks and chemical composition reveal the chemical properties of the composite being made and help identify the presence of contaminants in the samples. The quality of the liquid preparation can be determined using the multifractal spectra methodology, which is particularly important when adding more phases to the composite. However, the primary functions of measuring electrical characteristics, such as piezoelectric constants, are required to identify a functional material as a sensor layer.

### **2.1. X-ray diffraction measurement methodology**

An essential method for researching semi-crystalline and amorphous polymers is X-ray diffraction. It allows for the examination of various aspects of the material's microstructure, such as lattice parameters, the existence of flaws, crystallographic orientations (texture), and the degree of crystallinity.

In a standard X-ray diffraction experiment, the polymer sample is exposed to X-ray radiation, a type of electromagnetic energy with a short wavelength ( $\lambda = 0.1$  nm). X-ray diffraction of the samples was measured in the hard film mode in the  $2\theta$  range between  $10^\circ$  and  $80^\circ$ . The study was performed and showed mixed amorphous and crystalline phases, confirming no complete crystallization in the samples.

### **2.2. Fourier transform infrared (FTIR) spectroscopy measurement methodology and $\beta$ -phase transformation**

FTIR spectroscopy is a useful technique for investigating biological material chemistry. This method provides a quick, low-cost, and relatively non-invasive way to determine the chemical makeup of a biological material. It allows for the identification of primary chemical bonds and functional groups, offering details on the biological molecules present in the sample. Variability in the chemical profiles of specimens of the same species can be evaluated by spectral analysis. As a result, FTIR spectroscopy is an effective technique for analyzing differences in the ratios of key chemical components, both between species and specimens cultivated in various environments. FTIR spectra were used to analyze the bands associated with the  $\alpha$  and  $\beta$  phases of PVDF, which are more prevalent, especially at 537, 724, 734, and 895  $\text{cm}^{-1}$ . The effect of adding additional components such as HA, GO, and  $\text{AgNO}_3$  on the spectra was also examined.

Fig. 2.1 shows the Perkin Elmer UATR Two FT-IR spectrometer, which was used for FTIR analysis.



**Fig. 2.1** FTIR measurement: (a) measuring of sample; (b) spectrometer

Both phases ( $\alpha$  and  $\beta$ ) were observed in the FT-IR plots. To determine the fraction of the  $\beta$  phase present in each sample, IR absorption bands at  $763\text{ cm}^{-1}$  ( $\alpha$  phase) and  $840\text{ cm}^{-1}$  ( $\beta$  phase) were used. Assuming that the IR absorption follows the Lambert-Beer law, the relative fraction of  $\beta$  phase can be calculated using the equation [66, 120]:

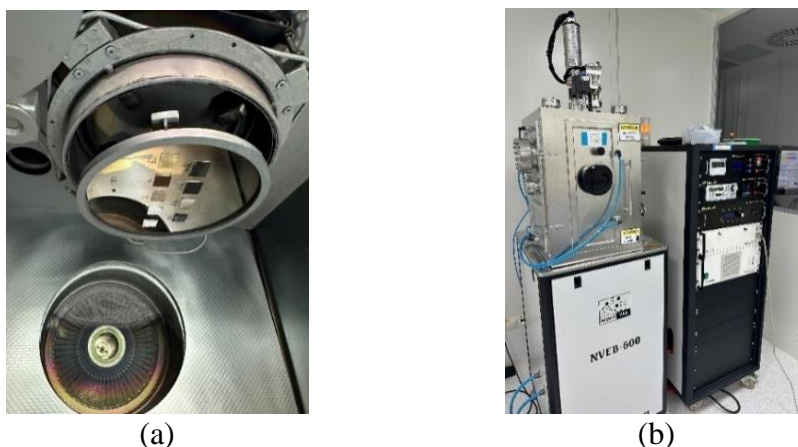
$$\Phi_{EA}^{IR} = \frac{I_{840}}{\frac{K_{840}}{K_{763}} I_{763} + I_{840}}; \quad (1)$$

where  $I_{840}$  and  $I_{763}$  are the absorptions at  $840\text{ cm}^{-1}$  and  $763\text{ cm}^{-1}$ , respectively, and  $K_{840}$  and  $K_{763}$  are the absorption coefficients at the corresponding wavenumbers [66, 120].

### 2.3. Scanning electron microscope (SEM) measurement methods

SEM is used to examine the morphology of materials. This analysis was chosen to observe the phase change of PVDF and determine whether the additive particles have penetrated the structure and are evenly distributed. To prepare the samples for measurements, they were coated (with an Au layer for scanning quality) using the e-Beam method. The samples were placed into an electron-beam physical vapor deposition chamber (Nanovak NVEB-600, Fig. 2.2), evacuated to a pressure of  $9 \times 10^{-6}$  Torr, and coated with gold to obtain a conductive surface for SEM analysis. The gold source was evaporated by applying 56 mA current to the filament and the layer thickness was kept constant at 5 nm.





**Fig. 2.2** Au coating machine: (a) mirror plate with samples; (b) Nanovak NVEB-600 machine

SEM images were obtained using the FEI QUANTA 250 model under the following conditions: a 7–9 mm working distance, 0–130 Pa pressure, and a voltage of 10 kV under a high vacuum medium. FEI QUANTA 250 model is shown in Fig. 2.3.



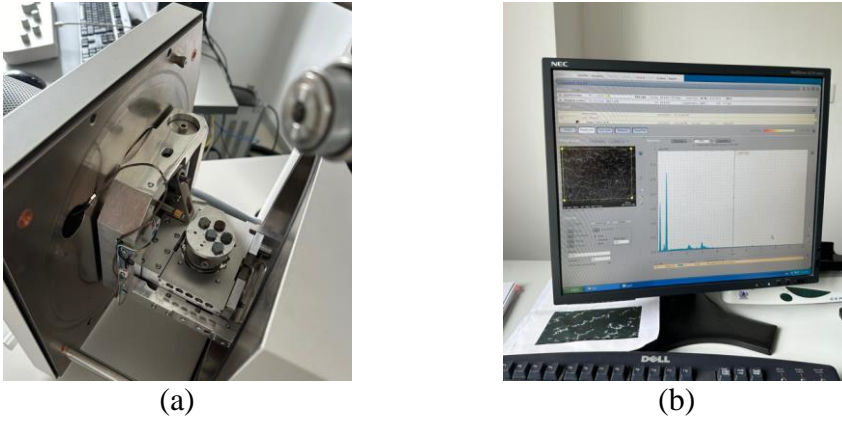
**Fig. 2.3** Scanning electron microscopy FEI QUANTA 250 machine

## 2.4. Energy-dispersive X-ray (EDX) and mapping measurement methodology

EDX analysis was used to determine the chemical elements and their concentrations in the precursors. It also reveals the presence of any additional impurities (chemical elements) in the samples, which is why this analysis was chosen.

The mapping results show the upper layer of the analyzed samples. A separate mapping result is created for each chemical component of the composition, which shows whether any impurities or additional elements are present, as well as the distribution and concentration of those particles. Alongside SEM or TEM, EDX analysis is carried out. This provides the general spatial mapping of a sample, as well as elemental specifics of its near-surface elements. In this process, the sample is exposed to a high-intensity electron beam of around 10–20 keV, and an energy-

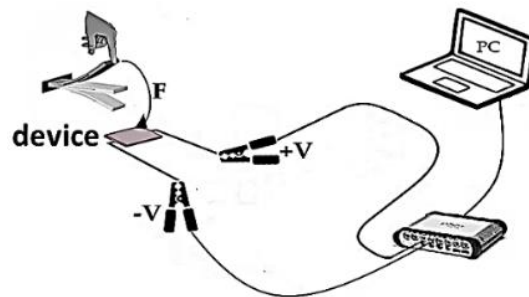
dispersive spectrometer gathers the X-rays emitted by the material. The elemental specifics of the sample are provided by the energy of the X-rays produced, which are traits of the atomic structure of the element from which they are emitted. EDX is typically used as a bulk characterization method because X-rays are produced to a depth of around  $2\text{ }\mu\text{m}$  in the material. One such method involves examining chemical maps of particle surfaces and cross-sections acquired with SEM/EDX. Information regarding the properties of the sample, including particle type (such as carbon or fluoride), layer composition, particle shapes, structure, etc., can be found in chemical maps and electron micrographs. Fig. 2.4 shows the EDX measurement equipment Bruker 127 eV and Esprit software for analysis.



**Fig. 2.4** EDX measurement: (a) samples prepared for scanning; (b) Esprit system analysis

## 2.5. Electrical potential measurement methodology

Electrical measurements were chosen to measure the electrical potential of each sample under the action of a force. This approach aims to determine whether the addition of materials affects the electrical characteristics. To investigate the electrical properties, five specimen-based devices (samples 1, 2, 3, 4, and 5) were constructed. Each device consisted of three layers: steel, specimens, and aluminum. Additionally, the reference [98] conducted similar research and measured the voltage in an open circuit. Fig. 2.5 depicts the schematic path of the electrical characteristics research of the devices.



**Fig. 2.5** Scheme for measuring the electrical properties of samples

## 2.6. Hydrophilicity testing

Hydrophilicity is measured to determine the effect of additional materials on the water absorption of the sample. This is important because it can affect electrical characteristics and play a role in hydrolysis processes. The wettability and surface free energy of the samples were evaluated by measuring the contact angle. Understanding the wetting behavior of solvents on solid surfaces is essential for improving the electrical characteristics of the produced samples and examining the intermolecular communication between the liquid analyte and the piezoelectric solid surface. The wetting intensity determines the equilibrium between adhesion and cohesion [50].

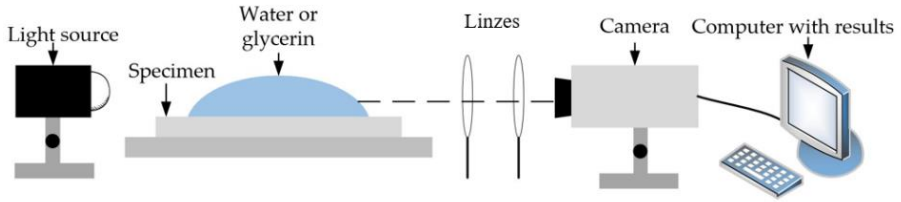
The impact of adding silver-impregnated activated carbon powder and functionalized carbon nanotubes to the material composite, aiming to increase its electrical conductivity and hydrophilicity on the electrosorption capacity of the electrodes was examined.

The PAC electrode and the silver-impregnated electrode both have contact angles close to  $90^\circ$ , demonstrating their hydrophobic nature and indicating that silver impregnation does not contribute to their alteration. However, the contact angle of the functionalized MWCNT-incorporated electrode dropped to  $82^\circ$ , suggesting that the addition of functionalized MWCNT increases the hydrophilicity of the electrode. According to the results [51], the contact angle decreases more slowly than the electrical conductivity increases.

In the frequency range of 0.1–25.0 GHz, the broadband behavior of the complicated electrical characteristics of glycerin–water mixtures was examined. Due to its total miscibility with water, glycerin is a particularly adaptable binding fluid that can be adapted to a range of fabric qualities. Being non-toxic and antibacterial, glycerin is perfect for human safety and is found in a lot of soaps, hand creams, and food products. In addition, it becomes lossy in the 1–2.5 GHz frequency band, making it useful for attenuating undesired multipath signals. At all frequencies, the actual conductivity decreases monotonically as the glycerin content increases. Similarly, as the glycerin–water ratio increases, a steepening of the dispersion is observed. At frequencies above 10 GHz, conductivity increases monotonically with both frequency and water concentration. Moreover, as the percentage of glycerin to water increases, the slope of the conductivity change with frequency decreases noticeably. The findings demonstrated that the conductivity of the water mixtures at 0.5, 2.0, and 5.0 GHz glycerin combined with water and 0.9% rises from low values to a maximum and then falls to lower values as the water content rises. Differences between the saline and water situations become more noticeable when the concentration surpasses 60% and start to appear when the concentration exceeds 30%. The near-complete binding of water to proteins and long-chain molecules at lower water concentrations was identified as the cause of this reaction, as it restricts the mobility of ions necessary for electrical conduction. There are not enough open water molecules to permit ion movement unless the water content is increased [53].

The wettability and surface free energy of the samples were assessed using contact angle measurements. Fig. 2.6 shows the schematic routes for measuring the angles. Understanding the wetting behavior of solvents on solid surfaces is essential for studying the intermolecular communication between the liquid analyte and the

piezoelectric solid surface, as well as for enhancing the electrical characteristics of the produced samples. The balance of forces between adhesion and cohesion is determined by the degree of wetness [50].



**Fig. 2.6** Hydrophilicity measurement scheme: (1) drop on samples, (2) coating base, (3, 4) convex double lenses, (5) Guppy CMOS camera, and (6) software system

A contact angle measurement technique was used to evaluate the wettability of a surface by a liquid. Fig. 2.6 shows the schematic routes for measuring the angles using a contact angle goniometer for the determination of the contact angle between a drop of liquid on a solid surface (Faculty of Mechanical Engineering and Design, Kaunas University of Technology). The process involves placing a droplet of liquid on a surface and measuring the angle formed between the droplet's edge and the surface. A low contact angle (below 90°) indicates a hydrophilic surface, while a high contact angle (above 90°) suggests a hydrophobic surface.

Moreover, biosensing elements often require hydrophilic surfaces to ensure efficient interaction with biological molecules, which are typically dissolved in aqueous solutions. A hydrophilic surface attracts water and, consequently, the biological molecules in it. This facilitates contact between the molecules and the sensor's detection layer, enhancing sensitivity. Furthermore, the force balance between adhesion and cohesion can be determined by the degree of wetting [3]. In this research, to understand how solvents wet solid surfaces and what is intermolecular communication between the liquid analyte and the piezoelectric solid surface, a set of five repeating measurements was performed with each liquid, water and glycerine, and the average angles were used for the final evaluation of hydrophilicity.

## 2.7. Piezoelectric coefficient ( $d_{33}$ ) measurement

The piezoelectric characteristics (D coefficient) are measured to determine the influence of additives and manufacturing technology on the samples. The manufacturing process and materials are selected to maximize the D constant. This constant is one of the most important properties for the application of a functional element in the piezoelectric field. The D constant is related to large mechanical displacements, typically found in motion transducer equipment. Conversely, the coefficient can also be considered as related to the load placed on the electrodes under mechanical stress. The piezoelectric effect is an interaction between the mechanical and electrical behavior of the material, and, to a linear approximation, this interaction can be described by the following expressions [80]:

$$S = S^E T + dE; \quad (2)$$

$$D = \varepsilon^T E + dT; \quad (3)$$

where  $E$  is the electric field strength,  $D$  is the dielectric displacement,  $T$  is the applied stress,  $S$  is the strain,  $s$  is the compliance, and  $\varepsilon$  is the permittivity.

The superscripts  $E$  and  $T$  are used to indicate values determined at constant field and stress, respectively. The above equations are generalized, without the directional notation [29].

The constant  $d$  is related to three important properties of the material, according to the following equation [80]:

$$d = k\sqrt{\varepsilon_0 k^T s^E} \quad (C \text{ N}^{-1}). \quad (4)$$

In this formula,  $k$  is the electromechanical coupling coefficient,  $k^T$  is a dielectric constant under constant tension, and  $s^E$  is the elastic correspondence ( $10 \text{ m N}^{-1}$ ) in the constant electric field. The following are the two main constants [80]:

$$d_{31} = k_{31}\sqrt{\varepsilon_0 k_3^T s_{11}^E} \quad (C \text{ N}^{-1}); \quad (5)$$

$$d_{33} = k_{33}\sqrt{\varepsilon_0 k_3^T s_{11}^E} \quad (C \text{ N}^{-1}). \quad (6)$$

The  $d$  constants are related to large mechanical displacements commonly found in motion transducer equipment. Conversely, the coefficient can be considered to be related to the load assembled on electrodes under mechanical stress,  $d_{33}$  applies when the force acts in three directions—parallel to the axis of polarization—and acts on the same surface from which the load is taken.  $d_{31}$  is applied when the load is collected from the same surface as  $d_{33}$ , but the force acts perpendicular to the axis of polarization. They are known to have the following empirical connection [80]:

$$d_{33} \approx -2.5 \times d_{31}. \quad (7)$$

The piezoelectric charge coefficient connecting the electrical charge generated per piece area with the mechanical force is applied and calculated by coulombs-Newton units ( $C \text{ N}^{-1}$ ). This constant is most commonly used for the evaluation of piezoelectric materials [80]:

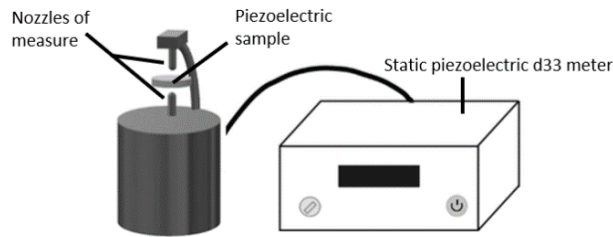
$$d = \frac{\text{Strain developed}}{\text{Applied field}} = \frac{\text{Charge density (open circuit)}}{\text{Applied stress}}. \quad (8)$$

PVDF-based thin films were prepared from DMSO solvent at  $90^\circ\text{C}$ . Granulated PVDF was dissolved in DMSO, while HA and  $\text{AgNO}_3$  were dispersed in DMSO at room temperature. The solutions were mixed uniformly and poured onto the substrate at room temperature. The films were then dried at  $65^\circ\text{C}$  for approximately 3 hours.

The  $d_{33}$  constant was measured using the PolyK Quasi-Static Piezoelectric  $d_{33}$  Meter (Fig. 2.7). A schematic of the piezoelectric constant is presented in Fig. 2.8.



**Fig. 2.7** PolyK Quasi-Static Piezoelectric  $d_{33}$  Meter



**Fig. 2.8** Schematic of the piezoelectric constant  $d_{33}$  by PolyK Quasi-Static Piezoelectric  $d_{33}$  Meter

## 2.8. Surface roughness measurement methodology

Surface roughness is measured by evaluating the differences in the height of surface particles in the relief. During scanning, these characteristics are assessed by selecting a point on the sample, which can affect other properties. The surface roughness of a film affects its mechanical properties [73]. The surface texture of an object is a key factor that greatly influences the wear resistance, fatigue life, and friction characteristics of individual components.

Fundamental surface parameters, such as waviness and surface roughness, are important features of the object that significantly affect the wear resistance, fatigue life, and friction characteristics of the components [84].

Surface roughness has been extensively researched as a major component of surface texture, although tactile surface texture has received significantly more attention. There are two methods for measuring surface roughness: touch and non-contact. Contact methods rely on repulsive mechanical contact with the test surfaces and are often immune to external interference. In contrast, non-contact methods, which are distinguished by their great sensitivity to the surface height and slope, measure the surface in a non-destructive manner [85].

The amplitude, frequency, and amplitude-to-wavelength ratio ( $a/\lambda$ ) of deviations from the typical surface form in the vertical direction can be used to quantify the roughness of the physical characteristics. The surface roughness of thin films is

frequently represented by average roughness values. For ultra-thin films, the size/wavelength-to-material ratio (Str) and the interfacial area ratio (Sdr) were created [64, 86].

The homogeneity of surface texture is gauged by the Str parameter. The value is calculated by dividing the horizontal distance in the direction of the slowest decrease by the horizontal distance in the direction where the autocorrelation function reduces to the value [s]. A measure of the correspondence between an image displayed at various coordinates and the original image is called the autocorrelation function in image processing. The autocorrelation function is determined using the following formula [86]:

$$Str = \frac{S_{al}}{\max(\sqrt{\tau_i^2 + \tau_j^2})}. \quad (9)$$

The Sdr represents the increase in surface area of a texture (within a defined area) relative to the plane definition area. This parameter is expressed as a percentage. The Sdr value increases with surface slope, while a perfectly level surface has an Sdr of 0 [86, 87]. It is defined as:

$$Sdr = \frac{1}{A} \left[ \iint_A \left( \sqrt{1 + \left( \frac{\partial z(x,y)}{\partial x} \right)^2 + \left( \frac{\partial z(x,y)}{\partial y} \right)^2} - 1 \right) dx dy \right]. \quad (10)$$

The experiments were conducted using the VR series ONE-SHOT 3D.

## 2.9. Multifractal spectra measurement methodology

Multifractal spectra reveal the microscopic distribution and structural complexity of materials. This analysis is crucial for assessing the quality and homogeneity of our samples. The analysis is performed using SEM images. In the context of the PVDF  $\beta$  phase, these spectra show the distribution of local particle density moments, which directly affects the heterogeneity of the material. Since it enables the thorough characterization and comparison of the complexity of various material structures and natural processes, multifractal analysis is essential in the context of materials. By employing this technique, traits that might not be apparent using traditional methods can be identified. Multifractal analysis is used to investigate the heterogeneity, pore distribution, grain shapes, and other structural elements that affect the physical and chemical properties of materials [88, 89]. It also enables the identification and quantification of material variability, opening new perspectives for assessing material quality and processing. In the context of material testing, this method can be particularly valuable for identifying and analyzing structural diversity, which directly affects material properties such as strength, elasticity, or conductivity.

## 2.10. Dynamic investigation methodology

Dynamic measurements are needed to determine whether the functional elements are working and can detect vibrations. The aim is to assess whether  $\text{AgNO}_3$  and HA gradually amplify the signal. Sensors such as an accelerometer, a laser distance meter, and both contacts of our recently developed functional element were used to collect data. The samples were evaluated by measuring the output signal and

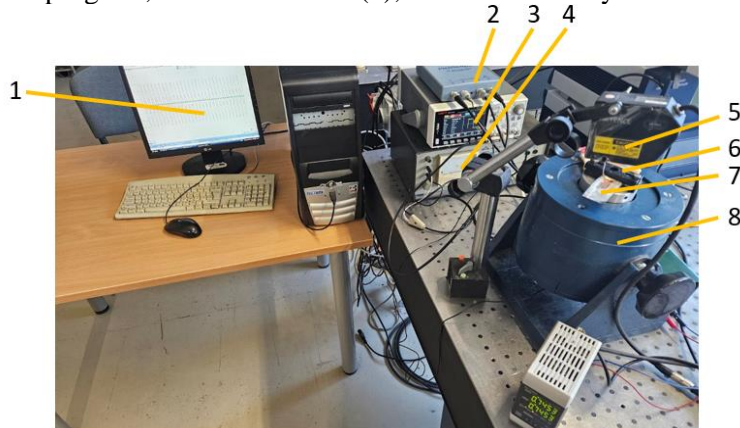


using a sinusoidal signal with the first resonant frequency of 11 Hz (plate frequency). Five metal plates, each covered with various PVDF materials, were tested. Following the addition of a thin layer of copper, two wires with contacts on both sides—on a copper plate and a metal plate—were soldered. A multimeter was used to verify the insulation, ensuring no short circuits. The samples used in this study are illustrated in Fig. 2.9.



**Fig. 2.9** Samples prepared on steel plates coated with different PVDF materials with a conductive copper phase on top and contacts

Fig. 2.10 displays the experimental configuration. Clamps (6) were used to secure the copper film and the PVDF-covered metal plate (7) to the vibrator (8). A sinusoidal signal for the vibrator was produced using the UNI-T UTG1022X signal generator (3) (Uni-Trend Technology Ltd., China) and VEB Metro LV103 signal amplifier (4). The vibration parameters (to detect vibration, mV) were detected using the KD35 vibration accelerometer (RFT GmbH, Schwabmünchen, Germany), which is not shown in the picture. The amplitude of the vibration of the metal plate and its end was measured using the LK-G82 laser distance meter (5) (Keyence, Elmwood Park, New Jersey, USA). Data from three sensors were collected using the PicoScope 3424 oscilloscope (2) (Pico Technology, Cambridgeshire, UK). The PicoScope 6.14.69 software program, connected to PC (1), was used to analyze the data.



**Fig. 2.10** Experimental setup with key hardware components: (1) computer, (2) oscilloscope, (3) signal generator, (4) signal amplifier, (5) laser distance meter, (6) clamps, (7) PVDF-covered metal plate, (8) vibrator



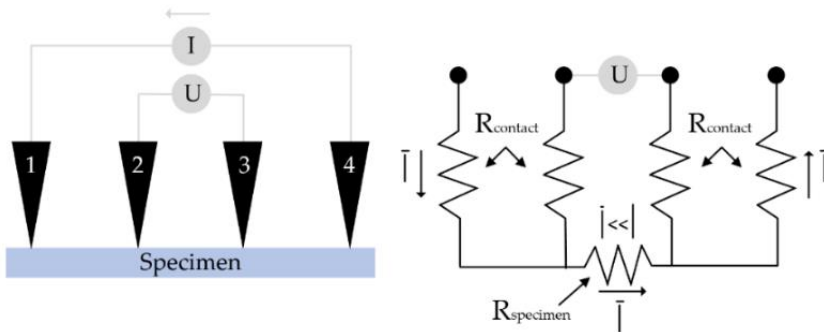
### 2.11. Four-point probe measurement methodology

A four-probe measurement was chosen to evaluate the resistance results of the samples. An ultra-high impedance voltmeter can be used to measure the voltage drop ( $V$ ) across the inner probe pair, while the current ( $I$ ) flows through the outer probe pair. Therefore, the current flowing through the sample causes a measured voltage drop across the semiconductor surface. During the measurement process, four equally spaced probes come into contact with the material and the electrical resistance measurement begins.

Due to its excellent precision and minimal sample preparation requirements, four-point probe characterization is a widely used technique in materials science to investigate the electrical characteristics of solids and thin films [55]. Novel nanoscale and biomaterials have been developed as a result of the rapid scaling of electronic devices [56].

In materials science and the semiconductor industry, four-point probe characterization is a common technique for examining the electrical characteristics of solids and thin films due to its high precision and minimal sample preparation requirements. The basic principle is quite straightforward: a voltmeter with very high resistance is used to detect the voltage drop across the inner pore of the probe after a current is allowed to pass through its outer pore. As a result, the measured voltage drop ( $V$ ) occurs mainly at the surface of the semiconductor due to the current ( $I$ ) flowing through the sample. When measuring semiconductor crystals or thin films, the current essentially flows through three channels, namely the surface state, the surface space charge layer, and the bulk state [25].

Various measurement modes have been developed for the traditional four-point probe, including the Van der Pauw mode, square mode, collinear mode, dual probe configuration mode, and other modes [25, 57, 58]. Among these, the collinear mode is widely used, and the principle of the collinear four-point probe method is presented in Fig. 2.11.



**Fig. 2.11** Four-point probe method:  $I$  is the current applied between the outer probes (1, 4),  $U$  is the voltage between probes 2 and 3, and  $R$  is the sheet resistance

A voltmeter with ultrahigh impedance can be used to measure the voltage drop ( $V$ ) across the inner probe pair, while a current ( $I$ ) flows through the outer probe pair. Consequently, the current flowing through the specimen causes the measured voltage

drop to occur on the semiconductor surface. Then, the four-point probe resistance ( $R$ ) is [25]:

$$R = \frac{V}{I}; \quad (11)$$

$$R_{2D}^{4pp} = \frac{1}{\pi\sigma_s} \ln\left(\frac{2s-r}{s+r}\right); \quad (12)$$

$$R_{3D}^{4pp} = \frac{1}{\pi\sigma_b} \ln\left(\frac{1}{s+r} - \frac{1}{2s-r}\right); \quad (13)$$

where:

$s$  – the spacing between adjacent point contacts;

$r$  – the radius between adjacent point contacts;

$\sigma_s/\sigma_b$  – uniform sheet conductivity of the specimen under measurement.

Since the  $r$  is tiny compared to the probe spacings, it is disregarded. The following formulas can be used for the calculation [25]:

$$R_{2D}^{4pp} = \frac{U}{I} = \frac{\ln 2}{\pi\sigma_s}; \quad (14)$$

$$R_{3D}^{4pp} = \frac{U}{I} = \frac{1}{2\pi s\sigma_b}. \quad (15)$$

In this study, the Model 4200-SCS Semiconductor Characterization System (Keithley, Tektronix, Bracknell, United Kingdom) was used for the four-point probe measurement. Fig. 2.12 presents the equipment.



**Fig. 2.12** The four-point probe method measuring equipment: (a) specimen measurement; (b) Model 4200-SCS Semiconductor Characterization System

As part of the measurement process, four equally spaced probes are brought into contact with a substance whose resistance is unknown. The volume resistivity can be calculated using the formula [25]:

$$\rho = \frac{\pi}{\ln 2} \cdot \frac{V}{I} \cdot t \cdot k; \quad (16)$$

where:

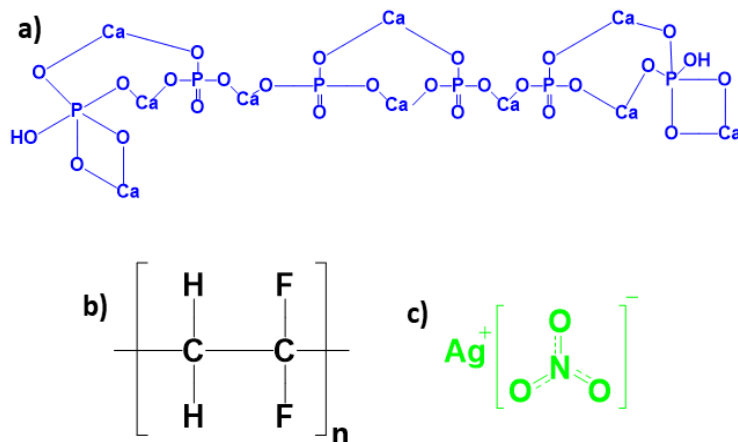
$\rho$  – volume resistivity,  $\Omega \cdot \text{cm}$ ;

$V$  – the measured voltage, V;  
 $I$  – the source current, A;  
 $t$  – the sample thickness, cm;  
 $k$  – a correction factor based on the ratio of the probe to wafer diameter and on the ratio of water thickness to probe separation.

To obtain the best measurement results, the probe must be placed in the center of the sample. One of the disadvantages of this method is that the specimen can be damaged.

## 2.12. Synthesis of hydroxyapatite (HA)

The chemical structures of PVDF, HA, and  $\text{AgNO}_3$  are shown in Fig. 2.13.



**Fig. 2.13** Visualization of the chemical structure of (a) HA, (b) PVDF, and (c)  $\text{AgNO}_3$

The production method for artificial HA in our investigation is depicted in Fig. 2.14. Phosphorus pentoxide ( $\text{P}_2\text{O}_5$ ) and calcium nitrate tetrahydrate ( $\text{Ca}(\text{NO}_3)_2 \cdot 4\text{H}_2\text{O}$ ) were employed as precursors in a 10:3 molar ratio. (1) Ten milliliters of ethyl alcohol ( $\text{C}_2\text{H}_5\text{OH}$ ) and distilled water were used to dissolve  $\text{Ca}(\text{NO}_3)_2 \cdot 4\text{H}_2\text{O}$  and  $\text{P}_2\text{O}_5$ . (2) The product was agitated at 400 rpm for 2 hours. (3) The gel formed near the bottom of the dish. (4) The gel was then allowed to air dry for 20 hours at  $120^\circ\text{C}$ . (5) Heat treatment was carried out for 15 hours at  $850^\circ\text{C}$  for sintering. This method is similar to the one described by [108, 109].



**Fig. 2.14** Synthesis of HA via the sol-gel method

### 2.13. Chapter conclusions

1. The characterization of the piezoelectric potential of the material can be analyzed through various methods, including SEM, surface roughness, multifractal spectra analysis, vibration parameters,  $d_{33}$  constants, 4-probe electrical measurements. SEM was used to study the morphology of the developed composites. The surface roughness methodology and its influence on the electrical characteristics are examined. Additionally, multifractal analysis was used to study material heterogeneity, pore distribution, grain shapes, and other elements affecting the physical and chemical properties of the material.

2. For dynamic research, a sinusoidal signal was generated using a signal generator and a signal amplifier. Vibration parameters were determined using a KD35 vibration accelerometer. The vibration amplitude of the metal plate and its end were measured using a Keyence laser distance meter. Three sensors were used to collect data using a PicoScope 3424 oscilloscope. The data analysis was performed with PicoScope 6.14.69 software, connected to a computer.

3. The wettability and free surface energy of the samples were evaluated using contact angle measurements. The piezoelectric effect, which describes the interaction between the mechanical and electrical behavior of a material, was investigated. The  $d_{33}$  constant was measured using a PolyK Quasi-Static Piezoelectric  $d_{33}$  meter.

4. The 4200-SCS semiconductor characterization system was used for four-point probe measurements. In materials science, the four-point probe measurement is a typical method for measuring the electrical characteristics of solids and thin films due to its high accuracy and minimal sample preparation requirements. During the measurements, four equally spaced probes make contact with a conductive surface to perform a four-point probe measurement.

### **3. SYNTHESIS AND ANALYSIS OF PIEZOELECTRIC PVDF COMPOSITE MATERIALS**

This dissertation aims to create a piezoelectric composite material based on PVDF with a cybersecurity model. The objectives include synthesizing PVDF by inserting HA, GO, and AgNO<sub>3</sub> nanoparticles to create a piezoelectric composite characterized by  $\beta$ -phase transformation. The study also aims to evaluate the influence of HA, GO, and AgNO<sub>3</sub> nanoparticles and their different compositions on the electrical, mechanical, and morphological properties of the piezoelectric composite. Since the phase transformation of PVDF is very important for these properties, a solvent casting method, along with materials that promote phase transformation, is selected. The properties of the materials are determined experimentally by measuring SEM, FTIR, vibration measurements, electrical characteristics, piezoelectric properties, hydrophilicity, roughness, and other characteristics.

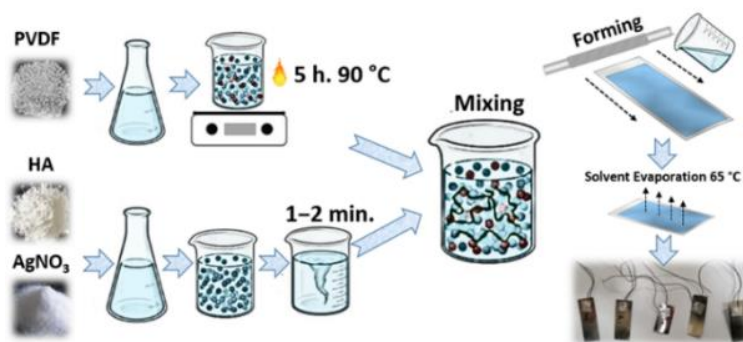
#### **3.1. Development of PVDF-based materials with hydroxyapatite (HA) and silver nitrate (AgNO<sub>3</sub>)**

This section describes the fabrication process of the functional element. The selected suitable materials for this element are PVDF, HA, and AgNO<sub>3</sub>, with the solvent casting method chosen for fabrication. The non-toxic solvent DMSO is used in the process. This fabrication method and materials were chosen to increase the beta phase, which is very important for cybersecurity and piezoelectric properties. The results of the composites with PVDF, HA, and AgNO<sub>3</sub> are presented.

##### **3.1.1. Preparation of PVDF/HA/AgNO<sub>3</sub> composites**

Chemicals in the liquid can more easily penetrate holes for a better surface. There is less carrier transport resistance in thin film dielectrics with smoother surfaces [64, 83]. For this reason, the solvent casting process is used for sample preparation.

DMSO is used as a solvent at an ideal temperature of 90 °C to create films. To create a homogenous solution, PVDF beads and a DMSO solvent were first combined and dissolved at 90 °C for 5 hours. At room temperature, AgNO<sub>3</sub> and HA were similarly dissolved in a DMSO solvent and agitated for one to two minutes to ensure equal dispersion. After mixing all the ingredients and pouring the solution onto the basis, the film is created using forming rods and dried in an oven at 65 °C for 3 hours. The entire preparation process is depicted in Fig. 3.1, while Table 3.1 provides a list of the precursor values.



**Fig. 3.1.** Synthesis scheme of composite solid films with PVDF/HA/AgNO<sub>3</sub>

**Table 3.1.** Concentrations and recipes of samples with PVDF/HA/AgNO<sub>3</sub>

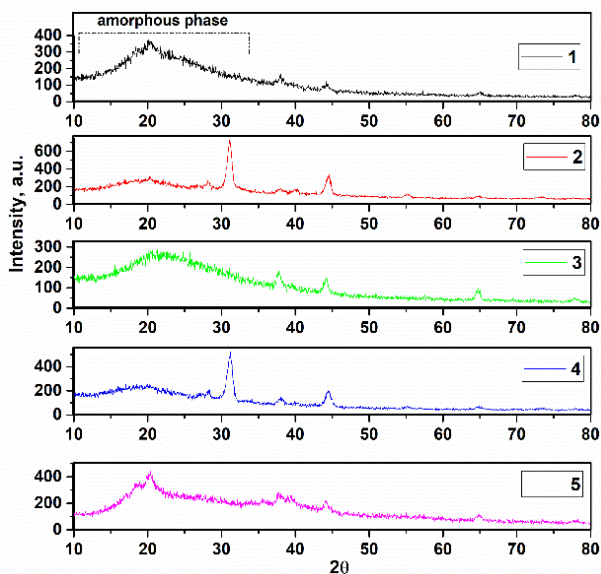
Sample No.	PVDF (g/ml)	HA (g/ml)	AgNO <sub>3</sub> (g/ml)
(1)	0.5g./2ml.	0.05g./1ml.	-
(2)	0.5g./2ml.	0.10g./1ml.	-
(3)	0.5g./2ml.	-	0.2g./1ml.
(4)	0.5g./2ml.	0.05g./1ml.	0.2g./1ml.
(5)	0.5g./2ml.	-	-

Five samples—0.05 g HA:0.5 g PVDF (1), 0.1 g HA:0.5 g PVDF (2), 0.2 g AgNO<sub>3</sub>:0.5 g PVDF (3), 0.5 g HA:0.5 g PVDF:0.2 g AgNO<sub>3</sub> (4), and 0.5 g PVDF (5)—were prepared at 90 °C for 5 hours until the colloidal phase was achieved, taking into consideration the initial characteristics of HA, PVDF, and AgNO<sub>3</sub>. After applying 200 µL of the liquid samples to create the films, the thin layer was rolled out and allowed to dry at 65 °C. DMSO proved effective, and because of its ice phase at ambient temperature, heat treatment was carried out at 90 °C. PVDF acted as a matrix, whereas HA and AgNO<sub>3</sub> served as reinforcements in the five types of produced composites (samples 1, 2, 3, 4, and 5). DMSO was used as a solvent due to its low toxicity and alternative nature [59, 60]. Large volumes of PVDF can dissolve in DMSO, a non-toxic solvent with low toxicity, at room temperature or slightly higher temperatures [60]. The production of composites with DMSO has a well-established history in the literature. For instance, a pleasantly scented form of DMSO was used to phase separate a compound based on polyethersulfone (PES) [59]. Additionally, kinetic and thermodynamic analyses, as well as the impact of various PVDF quantities on the physicochemical characteristics of the composite, have been investigated [3, 38].

### 3.1.2. Investigation of crystallinity parameters and particle size by X-ray diffraction

As shown in Fig. 3.2, X-ray diffraction of the samples in solid film mode was carried out in the 2θ range between 10° and 80°. It is important to note that samples 1, 3, and 5 show mixed amorphous and crystalline phases and did not exhibit complete crystallization. This could be attributed to the PVDF content and the low heat

treatment temperature of 80–90 °C [61, 65]. PVDF is divided into two phases:  $\alpha$  and  $\beta$ . The orthorhombic symmetry ( $Cm^2m$  space group) is associated with the  $\beta$ -phase, while the monoclinic symmetry ( $P21/c$  group) with the  $\alpha$ -phase [66]. The original  $\beta$ -phase of PVDF was used in this study, as confirmed by the sharp broad main peaks at  $2\theta = 19.89^\circ$ ,  $21.20^\circ$ , and  $20.38^\circ$  [68]. Additionally, the amorphous phase and the overlap with the  $\alpha$ -phase (020) can cause the  $\alpha$ -phase (020) to be monoclinic PVDF. The solute-solvent reaction is responsible for this [52]. The XRD patterns were consistent with the results of previous studies that used DMSO as a solvent and achieved the maximum percentage of  $\beta$ -phase in PVDF thin films when annealed at 90 °C for 5 hours [78]. Alternatively, Imtiaz Noor Bhatti et al. used acetone as a solvent and obtained a similar result to Satapathy, but they noted that  $2\theta = 20.3^\circ$  is part of the  $\beta$ -phase [44]. Dipolar interactions between C=O and CH<sub>2</sub>-CF<sub>2</sub> in DMSO and PVDF are responsible for the absence of the crystalline phase [45]. The  $\beta$ -phase of PVDF contributes to the faint peaks observed in samples 1, 3, and 5 at approximately  $37.92^\circ$  and  $44.05^\circ$ , respectively. Furthermore, the usage of HA as reinforcement leads to the mixed amorphous and crystalline phases observed in samples 2 and 4. The weak hydrogen bonds C=O...H-C may be the cause of this, as they both disrupt the interchain forces of PVDF:HA when the phases are combined [46]. The HA evidence is confirmed by the strong peaks at  $2\theta = 31.15^\circ$  and  $31.23^\circ$ , which are attributed to HA. Two peaks appear in this region because the amorphous phase is present in all XRD patterns, and the peak positions of AgNO<sub>3</sub> fall between  $20^\circ$  and  $25^\circ$ ; thus, the overlap of this amorphous region causes the AgNO<sub>3</sub> peaks to occur. However, quantitative X-ray EDAX analysis can be used to examine the presence of AgNO<sub>3</sub>.



**Fig. 3.2** X-ray diffraction results of samples with PVDF, HA, and AgNO<sub>3</sub>

### 3.1.3. Investigation of chemical properties and $\beta$ -phase transformation by Fourier transform infrared (FTIR) spectroscopy

The next stage of the study was analyzing the material's FTIR spectra, as shown in Fig. 3.3. These spectra indicated that bands associated with the  $\alpha$  and  $\beta$  phases of PVDF were more prevalent, particularly at 537, 724, 734, and 895  $\text{cm}^{-1}$  [25, 71]. The FTIR spectra of samples 1, 2, and 5 showed excellent agreement. However, there are minor variations in the transmittance percentage because sample 1 has more PVDF than samples 2 and 5. Considering the amorphous phases of the samples, the main HA compositions, such as  $\text{PO}_4^{3-}$ , can overlap with the PVDF  $\alpha$ - and  $\beta$ -phases due to the influence of  $\text{PO}_4^{3-}$  in the vibrational modes [47, 48]. When comparing the PVDF spectrum with the spectra of pure HA, a noticeable decrease in the strength of the bands in the  $\text{PO}_4^{3-}$  region formed by HA was observed, where the  $\alpha$ -phase was significantly reduced. The PVDF  $\beta$ -phase, located at 1193  $\text{cm}^{-1}$ , helped to strengthen the band at 1046  $\text{cm}^{-1}$ , which should have been present in the HA spectra of the composition from the beginning. In all samples, the spectra in the range of 1375–1982  $\text{cm}^{-1}$  are assigned to C–O bonds [49]. Additionally, the C–F bond may be responsible for the stretching band around 1340  $\text{cm}^{-1}$  [52]. Furthermore, the -OH groups of the HA components have shown that PVDF exists, which may account for the large range of wavenumber values from 2787 to 3548  $\text{cm}^{-1}$  [99]. Since both the composition content and crystallization temperature were low (90  $^{\circ}\text{C}$ ), and the sintering and crystallization temperatures of HA and  $\text{AgNO}_3$  were higher than  $\sim 500$   $^{\circ}\text{C}$ , their presence did not have a remarkable effect on the FTIR spectrum [100]. To transfer the phase and components of the composites, the FTIR results complied with the XRD results.

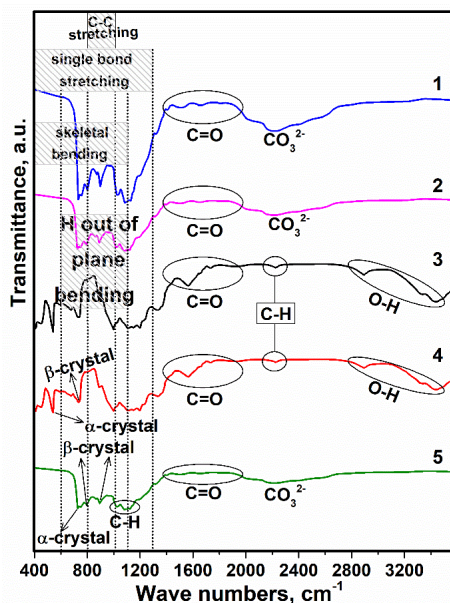


Fig. 3.3 FTIR spectrum results of deposited thin films

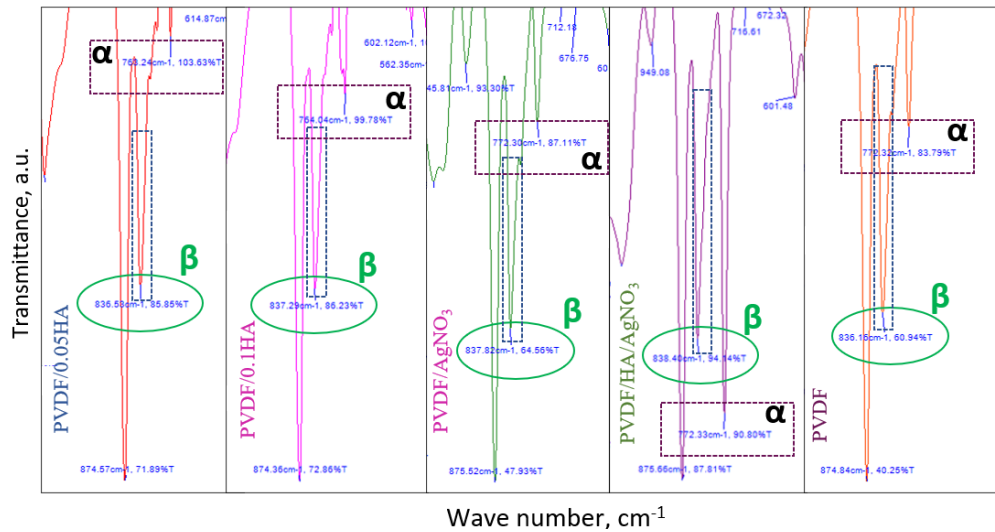


The presence of both phases ( $\alpha$  and  $\beta$ ) was observed in the FTIR diagrams. To determine the proportion of the  $\beta$ -phase present in each sample, the IR absorption bands at 763 and 840  $\text{cm}^{-1}$ , characteristic of the  $\alpha$ - and  $\beta$ - phases, respectively, were observed. Table 3.2 presents the  $\beta$ -phase concentrations and calculation data for the samples. Higher  $\beta$ -phase concentrations were observed in the PVDF/HA/AgNO<sub>3</sub> sample, while PVDF showed the lowest concentration of the  $\beta$ -phase. The results demonstrate that the addition of additional phases such as HA or AgNO<sub>3</sub> affects the  $\beta$ -phase transformation in the composites.

**Table 3.2.**  $\beta$  concentrations of samples with PVDF, HA, and AgNO<sub>3</sub>

Sample	$\alpha$ ( $\text{cm}^{-1}$ )	$\beta$ ( $\text{cm}^{-1}$ )	K (~840/763)	$\beta$ (%)
PVDF/0.05HA	103.63	85.85	~1.1	42.95
PVDF/0.1HA	99.78	86.23	~1.1	43.99
PVDF/AgNO <sub>3</sub>	87.11	64.56	~1.1	40.25
PVDF/HA/AgNO <sub>3</sub>	90.80	94.14	~1.1	48.52
PVDF	83.79	60.94	~1.1	39.80

The  $\beta$ -phase measurement was performed using IR absorption. According to the Lambert-Beer law, the relative fraction of the  $\beta$  phase was calculated for each sample. Fig. 3.4 presents the peaks of the  $\alpha$  and  $\beta$  phases for each specimen.



**Fig. 3.4** FTIR spectrum peaks of  $\alpha$  and  $\beta$  phases

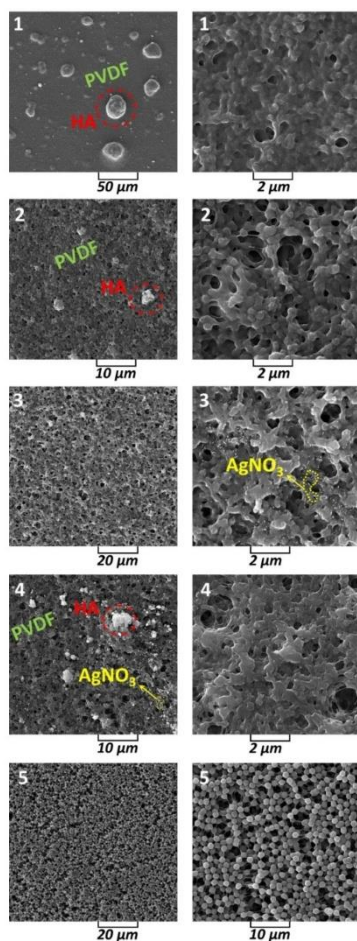
This calculation results in the ferroelectric phase accounting for about 50% of the total crystalline phase of the nanoparticles. From the combined analysis of X-ray diffraction and IR spectroscopy experiments, a ferroelectric response was observed.

#### 3.1.4. Morphology investigation with a scanning electron microscope (SEM)

SEM was used to examine the materials morphologically, and Fig. 3.5 shows the 3D images that were produced. As a result, it is evident that for sample 1, PVDF serves as both the matrix and the nucleation, and HA development on the PVDF

happens concurrently. Although X-ray diffraction could not be used to assess the size of the nanocrystallites because of the amorphous phases, the SEM images of samples 1 and 2 show spherical HA with diameters of approximately 25  $\mu\text{m}$  and 5  $\mu\text{m}$ , respectively, which can be predicted in comparison to pure PVDF. The HA:PVDF composite was made using an electrospinning technique, and it is important to note that the HA particles were nucleated on the PVDF and served as reinforcement [101]. Additionally, the comparable composition of samples 1 and 2 is linked to the similarity of their photographs. Since only a small amount of  $\text{AgNO}_3$  was used in the fabrication of sample 3, it was observed that the integration of  $\text{AgNO}_3$  was adequate, with good dispersion of these particles in the skeleton. The size of the nucleated particles in sample 4 decreased when all three constituents of the composites—PVDF, HA, and  $\text{AgNO}_3$ —were present. This phenomenon was noted for composites with PVDF as the primary component [21]. These minor variations between samples may be due to the evaporation rate and the use of DMSO as a solvent, which can alter conductivity and increase viscosity. The SEM image for sample 5 (PVDF alone) shows a uniform structure. When irregular porosities were created in the composites, the PVDF strand morphology was observed. The properties of the tetrahydrofuran solvent used (DMSO), particularly its polarity and the low temperature at which it was applied, may be the reason for the present results. This is because DMSO is a polar aprotic solvent that is miscible with various organic solvents and dissolves both polar and non-polar molecules, making it suitable for all the components that were chosen. In this case, the strong dipoles of the C-F bond in the molecular chain of PVDF and the amorphous phase rotate due to the polarity of DMSO, reducing the energy barrier for the development of the extended trans conformation [102, 103]. Therefore, during the thermal activation process, the PVDF may not be able to freely flow on the surface due to the high molecular weight of the composites.

Since the PVDF has a crystalline shape and the molecular chains are free to wander around and lack a stable structure, which adversely affects the electrical properties, it was desirable to create an amorphous phase in this study [105]. It is evident that at low temperatures (90  $^{\circ}\text{C}$ ), the reaction energy between the PVDF molecular chains is higher than the reaction energy of the PVDF:DMSO interaction. As a result, the crystalline region of PVDF remains essentially passive, and swelling occurs as the solvent permeates the amorphous region, as seen in the X-ray diffraction and SEM images.

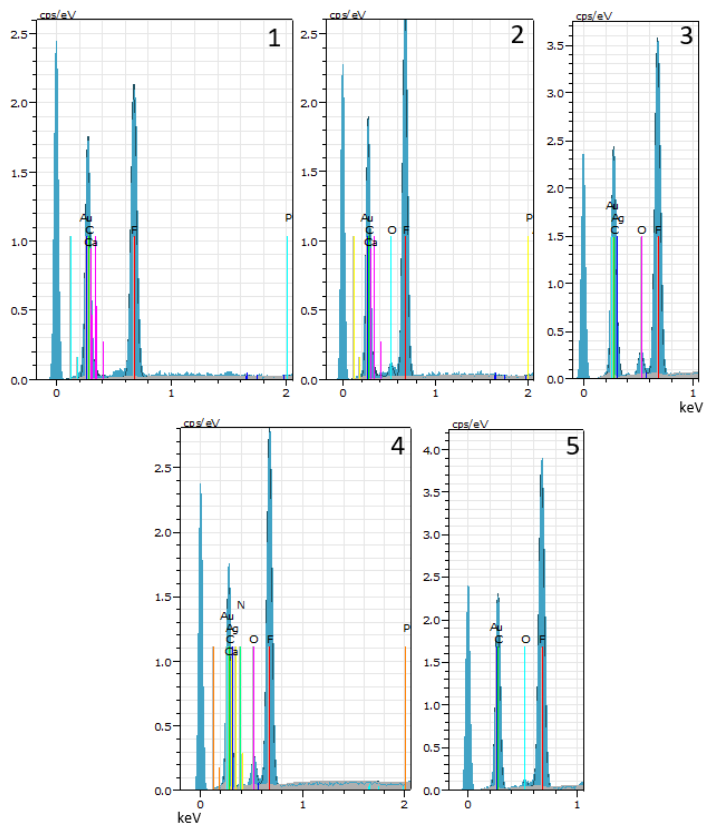


**Fig. 3.5** SEM images of PVDF/HA/AgNO<sub>3</sub> samples

### 3.1.5. Chemical components analysis by energy dispersive X-ray (EDX) method

EDX analysis was used to determine the chemical elements and their concentrations in the precursors. Fig. 3.6 shows the EDX spectra and quantitative ratios, with the obtained values listed in Table 3.3. In addition, in this study, the values presented in Table 4.2 confirmed that there were no impurities in the composite structure and they were consistent with the chemical compositions of the composites. A homogeneous distribution of elements is observed in the extracted EDX analysis values. Furthermore, the chemical elements predominant in the composites were detected in the EDX analysis: C, O, F, Ca, Ag, and P, which indicates a successful sample preparation. The small differences in values confirm that the presence of these elements must be taken into account when preparing the composites. As expected, the fluorine peak originating from PVDF is particularly intense and visible in all samples. The Ag spectra were detected in samples 3 and 4, confirming their presence in the samples. The gold phase detected corresponds to the Au coating required for the SEM

measurement process. Thus, Ca peaks are visible in the samples where the HA phase was injected.



**Fig. 3.6** EDX results: 1 – PVDF/0.05HA, 2 – PVDF/0.1HA, 3 –PVDF/AgNO<sub>3</sub>, 4 – PVDF/HA/AgNO<sub>3</sub>, 5 – PVDF

**Table 3.3** EDX results and component concentrations in samples

Element	1 – PVDF/ 0.05HA	2 – PVDF/ 0.1HA	3 –PVDF/ AgNO <sub>3</sub>	4 – PVDF/HA/ AgNO <sub>3</sub>	5 – PVDF
	Norm. [wt.%]	Norm. [wt.%]	Norm. [wt.%]	Norm. [wt.%]	Norm. [wt.%]
Fluorine	42.86	47.49	44.32	42.27	51.59
Carbon	39.75	37.27	28.97	23.95	36.78
Gold	16.78	12.57	7.48	7.69	10.43
Phosphorus	0.18	0.06		0.009	
Calcium	0.42	0.22		0.85	
Silver			15.52	20.42	

According to Table 4.2, when HA was used as reinforcement, the mass fraction of fluorine decreased to 42.86% (sample 1) and 47.49% (sample 2). The composition ratio of the main elements of HA was  $\text{Ca/P} = 2.33$  for sample 1 and  $\text{Ca/P} = 3.66$  for sample 2, respectively.  $\text{AgNO}_3$  as a reinforcement component was detected in composite 3. Furthermore, in sample 4, the addition of  $\text{AgNO}_3$  as an additional reinforcement decreased the Ca content, but the HA structure remained. These values were in good agreement with native HA ( $\text{Ca/P} = 1.67$ ) [45, 92, 97].

### 3.1.6. Study of electrical potential

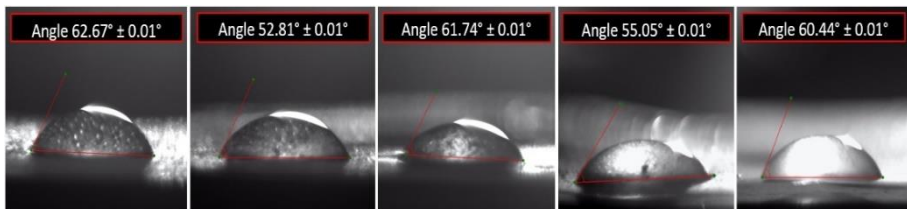
To investigate the electrical properties, five specimen-based devices (samples 1, 2, 3, 4, and 5) were constructed. Table 3.4 lists the values obtained from the electrical study. The absence of the active layer HA in samples 3 and 5 is responsible for the decrease in value. Sample 2 showed the highest energy level, with a value of approximately 0.12 W/A. Since the composites made from samples 3 and 5 (without HA) exhibited the lowest energy values, it is obvious that HA is suitable as a reinforcement to increase electrical durability. This is because of the initial fact that HA can display piezoelectric capabilities and the semi-empirical, automatically determined piezoelectric constants can be derived from the crystal structure of HA [116, 117]. Additionally, it is important to remember that the development of ferroelectric characteristics by PVDF can also increase mobility and the electric charge barrier at room temperature [118].

**Table 3.4** Energy values extracted for each sample

Energy (W/A)	Sample				
	1	2	3	4	5
	$0.08 \pm 0.01$	$0.12 \pm 0.01$	$0.06 \pm 0.01$	$0.09 \pm 0.01$	$0.05 \pm 0.01$

### 3.1.7. Hydrophilic analysis and results

The average angles between the spin-coated samples on the solid film and a drop of water are displayed in Fig. 3.7. The spin-coated sample 2 on the film had the lowest angle, with average angle values ( $\theta_{\text{Young}}$ ) ranging from  $52.81^\circ$  to  $62.67^\circ$ . For all samples, excellent wetting can be reported if  $\theta < 90^\circ$  [104]. It was observed that sample 2 exhibited the highest surface energy and best matches the liquid [106, 107]. The results indicate that the spin-coated surface of sample 2 has the highest uniformity and polarity on the solid film.



**Fig. 3.7** Droplet imaging and wetting angles of sample on solid films

### 3.1.8. Piezoelectric coefficient ( $d_{33}$ ) measurement results

As shown in Fig. 3.8, each sample was measured four times with increasing force in the range [2–5 N]. The PVDF sample had the lowest value on the piezoelectric meter, measuring 5.6 pC/N at a force of 2 N and steadily dropped. The PVDF/HA samples had the highest results, with a force of 2 N and a steady drop of 8.8–9 pC/N. The PVDF/HA/AGNO<sub>3</sub> sample also showed good results, with a  $d_{33}$  constant of 8.3 pC/N at a force of 2 N. A force of 2 N yielded the finest performance. The “x0.1” option on the  $d_{33}$  was selected for film metering. To prevent damage to the sample, the knob modifies the spacing between the two hemispherical probes, ensuring that the sample is held securely but not too tightly. Fig. 4.7 displays the meter’s reading of the  $d_{33}$  value for the samples. The meter shows the corresponding  $d_{33}$  values. The sample was then rotated 180 degrees and measured again in the opposite polling direction. The meter displayed  $d_{33}$  values with opposite polarization. The positive and negative results should be quite near; if they are not, the knob needs to be adjusted to obtain the right values. Quantitative analysis of soft polymer films is challenging. Therefore, the findings of the measurements must be qualitative, and the meter should be used to compare samples of comparable thicknesses.

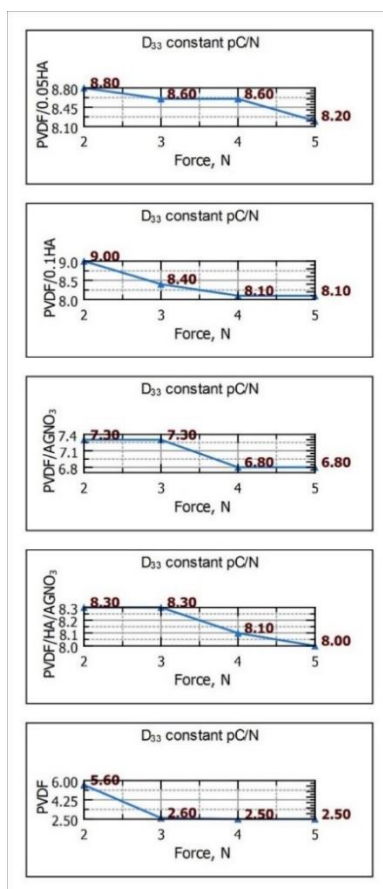
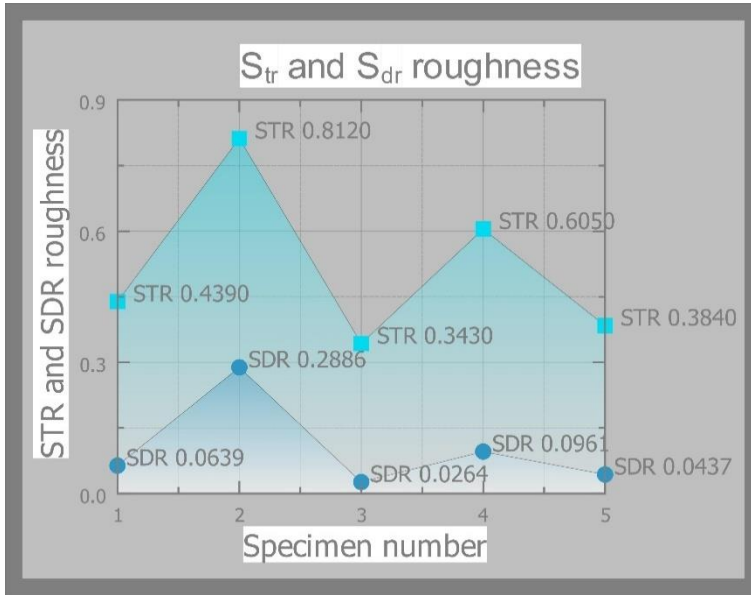


Fig. 3.8  $d_{33}$  measurement results of each sample

### 3.1.9. Surface roughness properties and results

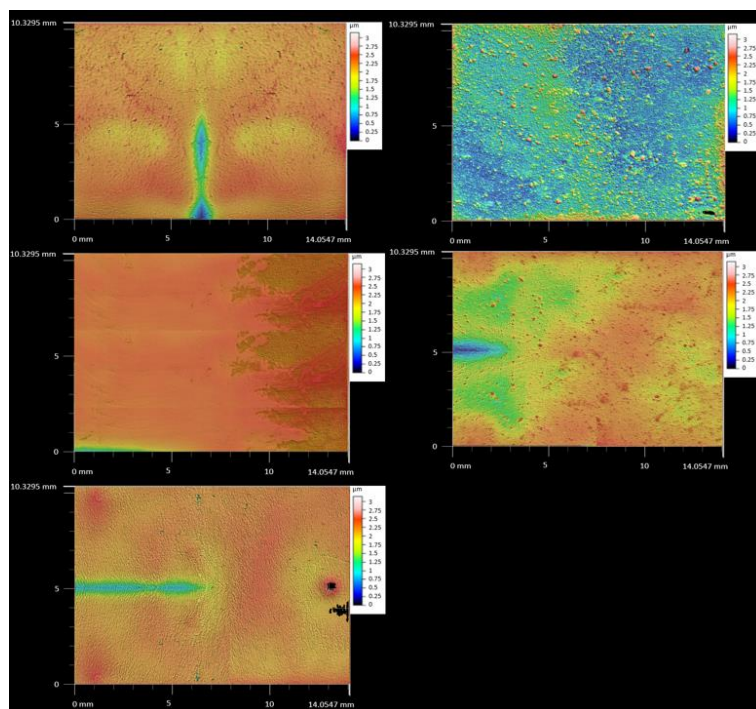
Str is the surface roughness level correlation measurement, as seen in Fig. 3.9. Sample 4 exhibited a Str roughness of 0.605, while sample 2 displayed the highest Str roughness at 0.814. The samples with the lowest surface roughness findings are 3 and 5. The addition of  $\text{AgNO}_3$  to the sample resulted in a decrease in both Str and Sdr roughness values.



**Fig. 3.9** Str (texture aspect ratio) and Sdr (developed interfacial area ratio)

The same pattern was observed in the Sdr results. The properties of thin films are often greatly influenced by surface roughness or the interaction between layers of different materials. Surface roughness affects many material properties, including dielectric. The electrical phenomenon can become more complicated if there is surface roughness or if the particles are unevenly distributed and form an uneven relief. To reduce the loss of optical and acoustic signals, it is necessary to reduce roughness and increase uniformity. The surface roughness evaluation is shown in Fig. 3.10. In sample 2, evenly distributed cluster points result in a higher value, which is influenced by the distribution of HA particles in the product. In image 1, the addition of the HA phase was twice as much and therefore it affected the lower surface roughness and the formation of aggregates, as confirmed by the Str and Sdr results. In samples 3 and 5, a small height distribution is visible because no solids were added, and the silver phase in sample 3 was successfully dissolved in the DMSO solvent. For samples 3 and 5, the height and roughness results were affected only by the forming method, which caused a slight change in film thickness.





**Fig. 3.10** Surface roughness images of samples 1–5

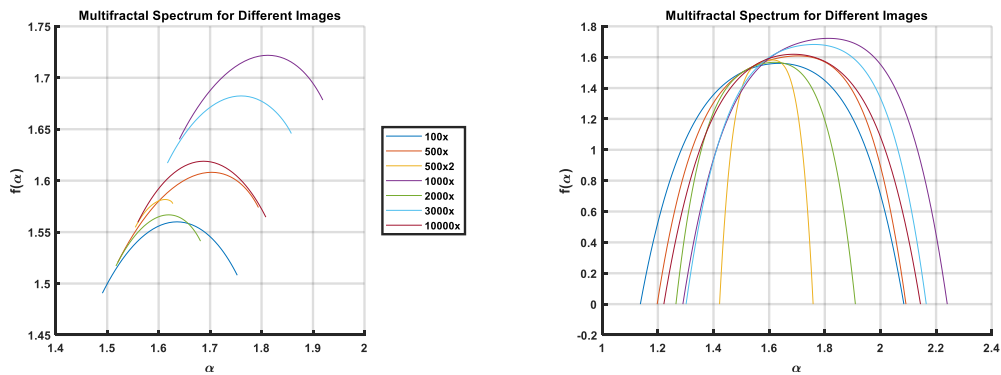
### 3.1.10. Multifractal spectra analysis

The singularity spectra for consecutively captured SEM images of materials are shown in Fig. 3.11. Several distinguishing characteristics can be observed. The slight differences between the samples may be related to the speed of evaporation and the use of DMSO as a solvent, which may cause a change in conductivity and an increase in viscosity. Sample 5 shows a uniform structure (PVDF alone) in the SEM image. PVDF fiber morphology was observed where uneven porosity was introduced to the composites. This might be related to the low drying temperature and polarity properties of the DMSO solvent. This is because DMSO dissolves both polar and non-polar molecules and is a polar solvent that blends well with a variety of organic solvents. In this case, the polarity of DMSO encompasses the amorphous phases and the strong dipoles of the C-F bond in the PVDF molecular chain, thereby lowering the energy barrier for creating the extended trans conformation.

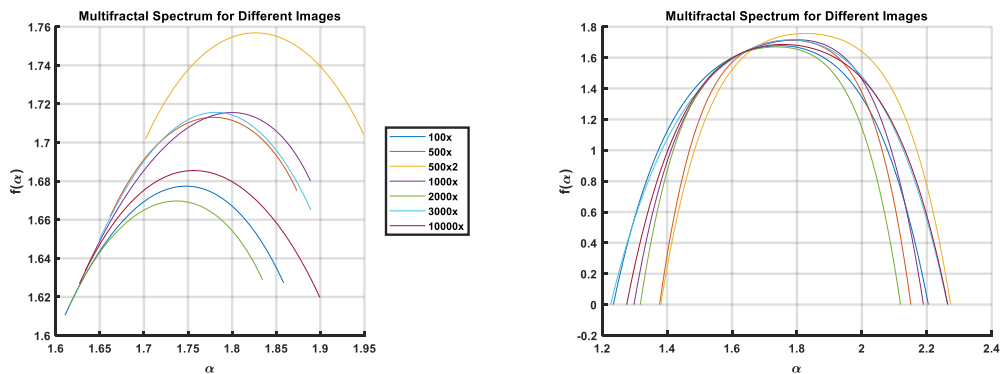
An amorphous phase was created for this study because PVDF is in a crystalline form and the molecular chains are allowed to wander without a defined structure, which negatively affects the electrical properties. The SEM images indicate that the reaction energy between the PVDF chains is higher than the contact reaction energy of PVDF and DMSO at low temperatures (around 90°C). Consequently, the crystalline portion of PVDF becomes passive when the solvent penetrates the amorphous portion, causing swelling. As a result, vaporized DMSO in the pores is evident in the SEM images of samples 1, 2, 3, and 4. The low (not too high)



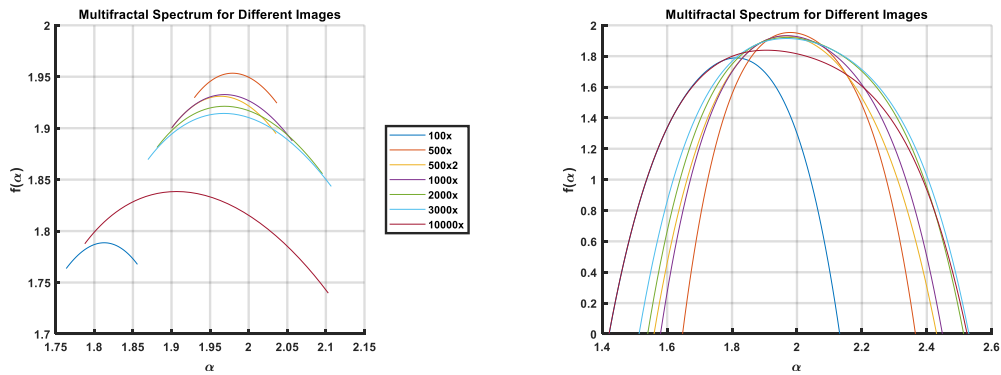
temperature promotes the formation of the  $\beta$ -phase in PVDF. A morphological study revealed that the constituent elements were not provided sufficient time or temperature to achieve crystallization.



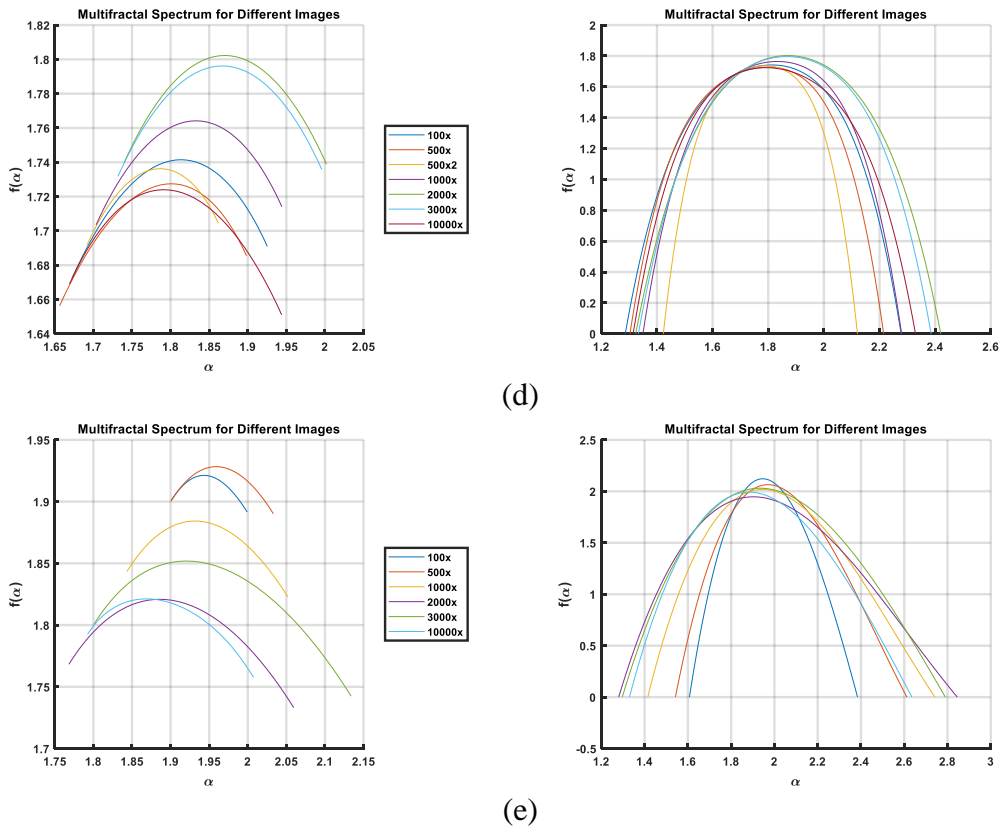
(a)



(b)



(c)



**Fig. 3.11** Multifractal spectra of individual images illustrating stable distributions that suggest a homogeneous structure for samples 1–5

Multifractal spectra for various samples are displayed in Fig. 3.11 to show the material's microscopic distribution and structural complexity. In the context of the  $\beta$ -phase of PVDF, these spectra demonstrate the distribution of local particle density moments, which directly affects the material's heterogeneity [93–95]. The even distribution of  $\text{AgNO}_3$  and HA in the PVDF matrix is indicated by the close spacing or overlap of the particle distribution curves, which is ideal for consistent ferroelectric and piezoelectric characteristics throughout the sample.

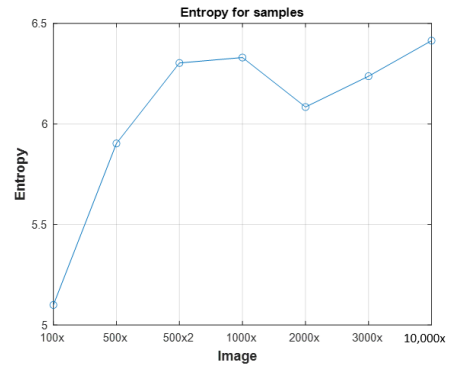
Achieving strong piezoelectric and ferroelectric activity requires the formation of an ordered  $\beta$ -phase, which may have been facilitated by the annealing process, according to this uniformity. For chemical and biosensing applications, where a precise reaction to mechanical or electrical stimuli is necessary, the stability of this phase is crucial.

At 100x magnification, Fig. 3.11a (100x) illustrates stable distributions of the spectrum, suggesting a homogeneous structure in the sample. The absence of notable variations indicates that the sample preparation procedure produced a homogeneous dispersion of nanoparticles within the matrix. In Fig. 3.11b (500x), the spectral value slightly increases, which can be a sign of increased structure heterogeneity at higher magnification. This could indicate that upon closer examination, local variations in

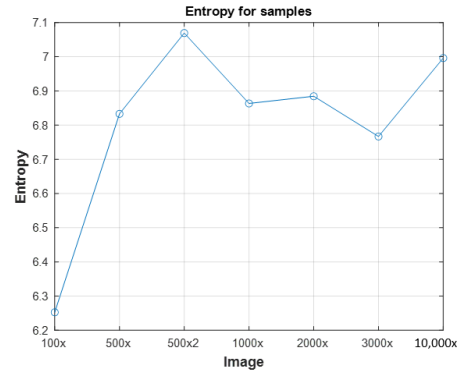
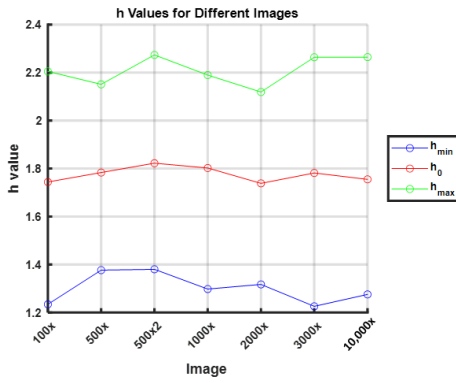
the distribution of molecules become apparent. A drop in the spectrum seen in Fig. 3.11c (500x2) indicates a change in the structure of the test sample compared to the earlier ones. The decline could be a sign of uneven distribution or agglomeration of nanoparticles, which would impact the material's homogeneity and possible qualities. Similar to the 100x sample, the spectrum recovers to more stable distributions in Fig. 3.11d (1000x). This would suggest that the material's structure is stabilizing, which might be the consequence of improved nanoparticle dispersion at this magnification level. The material structure gradually changes as a result of the sample preparation procedure and the impact of the added components (e.g.,  $\text{AgNO}_3$ , HA) on the PVDF structure, as shown in Fig. 3.11e (2000x, 3000x, 10,000x). The observed variations in the multifractal spectra at different scales can reveal information on how the distinct constituents affect the material's heterogeneity and characteristics.

Curves that are closely spaced from one another, even overlapping from left to right and up to down, indicate that the nanopowder particles in the sample's liquid are dispersed correctly. The fluid was improperly prepared if variations in the form and location of individual curves were observed. The SEM data are used to analyze multifractal spectra. The sample liquid contains properly distributed nanopowder particles if the curves overlap in both up and down and left to right directions [96]. If the liquid is not prepared properly, noticeable differences in the shapes and locations of the various curves will appear. The liquid was almost homogeneous, resulting in fairly consistent data. However, noticeable areas of accumulation were present, which may have caused some curves to shift positions.

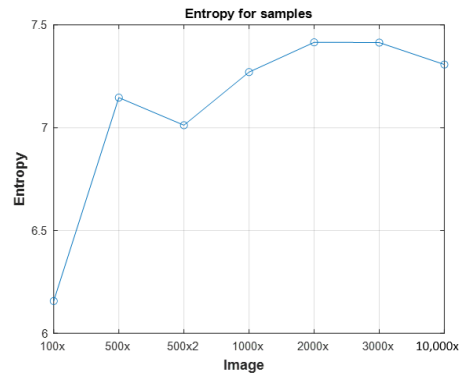
Fig. 3.12 presents the multifractal analysis results, which show consistent singularity spectra in a single plot for each sample. Several distinctive characteristics can be observed. Significant variations in the form and location of individual curves are visible in sample 1, where the spectra are displayed. This suggests that there are accumulations, damaged and transparent parts, or poorly prepared fluid. In sample 2, multifractal spectra are situated close to one another, even overlapping. In the up-down and left-to-right directions, the  $h_{\min}$ ,  $h_{\max}$ , and  $h^0$  values in Fig. 3.12 do not differ significantly from one another, suggesting that the nanopowder particles are evenly dispersed throughout the liquid in the sample. The same outcomes are observed in samples 3, 4, and 5, where the values in both directions remain consistent, suggesting that the nanopowder particles are dispersed throughout the liquid as intended. However, due to breakage or transparent portions in some samples, several curves have varied orientations.



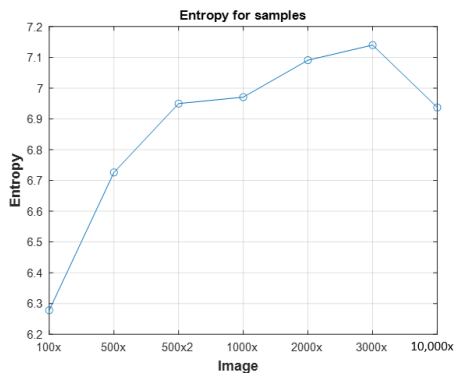
(a)



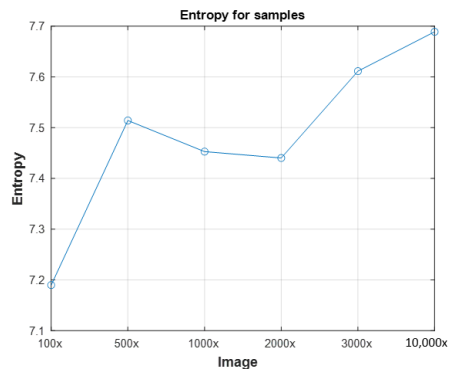
(b)



(c)



(d)



(e)

**Fig. 3.12** Graphs showing the juxtaposition of three key points in the multifractal spectrum ( $h_{\min}$ ,  $h^0$ , and  $h_{\max}$ ) and a graph showing the change in entropy with each increment for samples 1–5 (a–e)

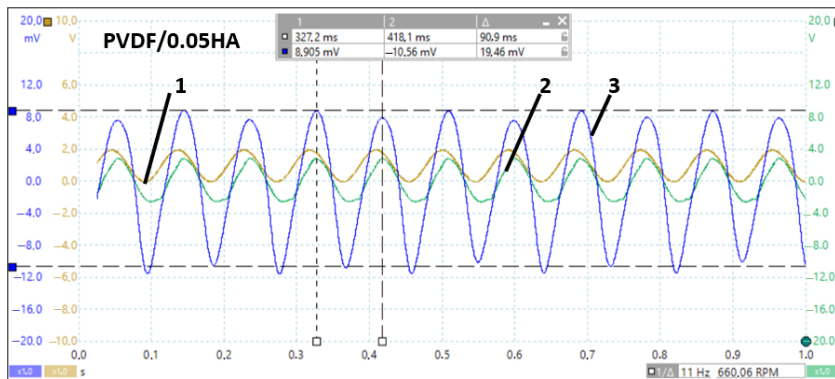
The numerical data are displayed in Fig. 3.12. The better the mixing and dispersion of the nanopowder particles, the smaller the  $h_{\min}$  value.

The characteristic values of the multifractal spectrum ( $h_{\min}$ ,  $h^0$ , and  $h_{\max}$ ) and entropy variations are displayed in Fig. 3.12. These values reveal details about the complexity and structure of the samples. Low  $h_{\min}$  and high  $h_{\max}$  values may indicate regions with high and low particle densities, affecting the local heterogeneity of the sample. The majority of the sample region is characterized by a moderate uniformity of particle distribution, as shown by high values of  $h^0$  relative to  $h_{\min}$  and  $h_{\max}$ . Entropy change: Entropy is a measure of a system's disorder or complexity that shows how annealing alters the structure of the  $\beta$ -phase. A decrease in entropy suggests a more ordered structure, which is advantageous for ferroelectric and piezoelectric capabilities. The uniformity of the sensor qualities may suffer from a high entropy, which could be a sign of a more disordered structure. A steady and uniform  $\beta$ -phase is essential for attaining the best ferroelectric and piezoelectric characteristics. Through a suitable distribution of  $\text{AgNO}_3$  and HA particles in the PVDF matrix, the annealing process is crucial for fostering this phase, as the observations indicate. The consistency and dependability of the sensor's reaction to stimuli are influenced by the

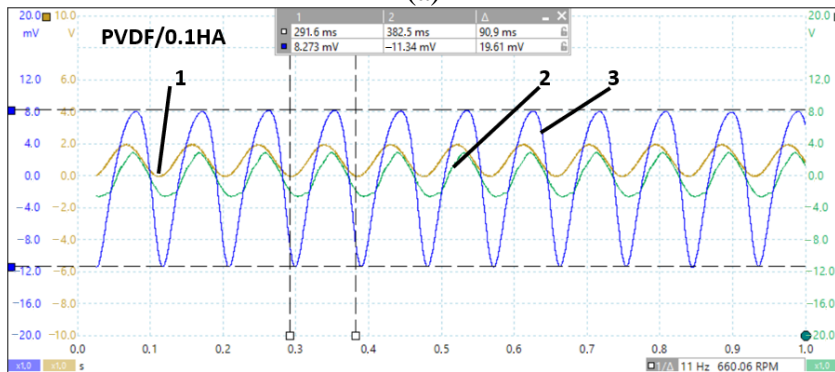
homogeneity of the  $\beta$ -phase. Structural stability and homogeneity are crucial characteristics because chemical sensors must accurately detect changes in the environment. A decrease in the  $h_{\min}$  value of the 500x2 signifies a drop in local homogeneity findings and suggests that the structure of the sample has changed. The presence of regions with greater heterogeneity may be indicated by an increase in the  $h_{\max}$  value, which is important for comprehending how operations like annealing affect the material. The degree of disorder and structural complexity is reflected in changes in entropy for individual samples. The observed decrease in entropy and concurrent fall in  $h_{\min}$  values in sample 500x2 may suggest that the structure becomes more organized, but with a greater degree of local particle aggregation.

### 3.1.11. Dynamic investigation results

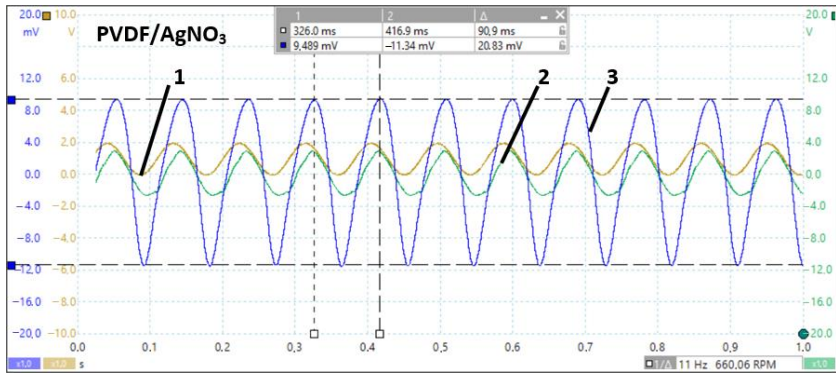
The data were collected using various sensors, including an accelerometer, a laser distance meter, and both contacts from our recently developed sensor. Five plates with different PVDFs were examined experimentally. They were all evaluated under the same conditions, which included measuring the output signal for each one and utilizing a sinusoidal signal with a first resonance frequency of 11 Hz (the plate's frequency). The findings are displayed in Fig. 3.13.



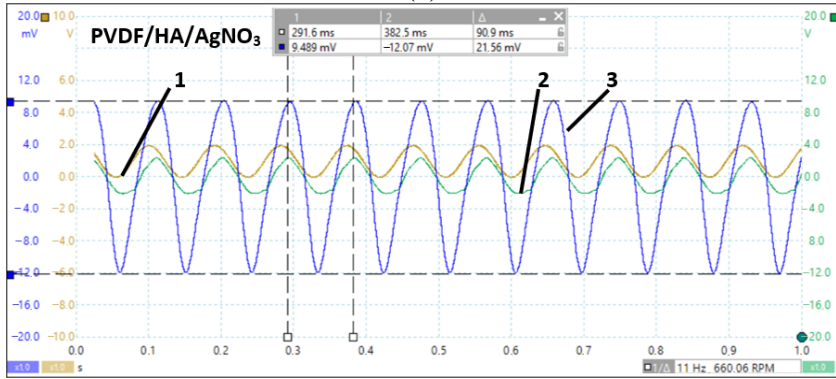
(a)



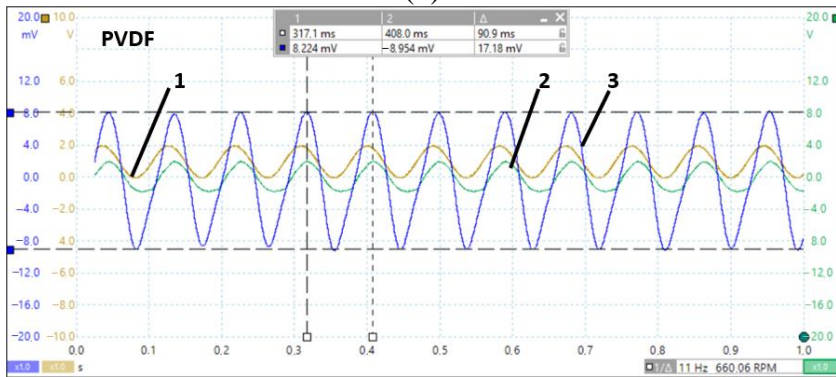
(b)



(c)



(d)



(e)

**Fig. 3.13** Data collection from three sensors: accelerometer (1), laser rangefinder (2), and both contacts from our newly created sensor (3); (a) signals using the 1st newly created sensor, (b) signals using the 2nd newly created sensor, (c) signals using the 3rd newly created sensor, (d) signals using the 4th newly created sensor, (e) signals using the 5th newly created sensor

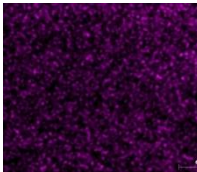
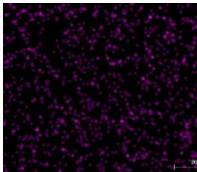
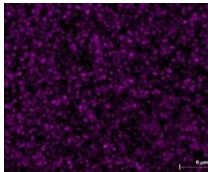
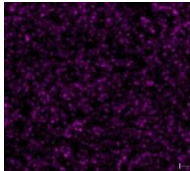
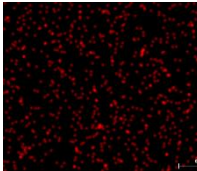
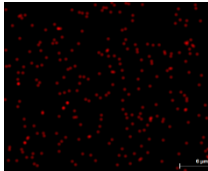

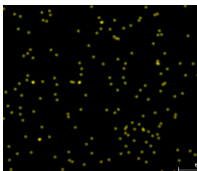
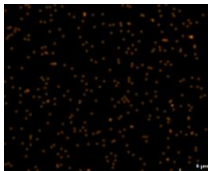
The results show that our recently developed functional elements are operational and capable of vibration detection. The lowest signal, 17.18 mV, can be produced using the PVDF functional element. Sample 2 (PVDF/0.1HA) can generate a slightly

higher signal at 19.46 mV. The functional element in sample 4 (PVDF/HA/AgNO<sub>3</sub>) may produce the highest signal at 21.56 mV, while the PVDF/AgNO<sub>3</sub> functional element may provide a signal with an amplitude of 20.83 mV. The PVDF/HA/AgNO<sub>3</sub> functional element produced the strongest signal. AgNO<sub>3</sub> and HA are two other substances that progressively boost the signal. All samples were subjected to the same tests.

### 3.1.12. Chemical components analysis by mapping method

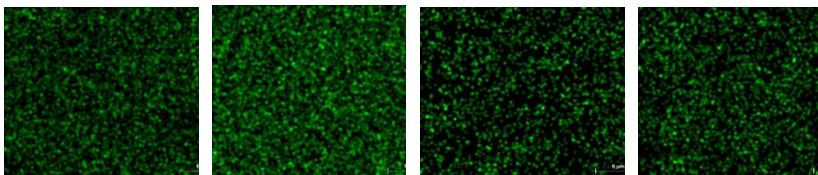
Table 3.5 shows the distribution of components F, Ag, Ca, and C on the surface of the sample. The results revealed that the top layer of the analyzed samples consisted of major chemical elements such as carbon, fluorine, silver, calcium, carbon, and phosphorus. In addition, no impurities or additional elements were detected. Further analysis revealed that the sample without HA (sample 1) was free of calcium and phosphorus. It was also found that the sample without AgNO<sub>3</sub> (sample 2) did not contain elemental silver. The observed results support the idea that the proposed solvent casting method (using DMSO as a solvent) is suitable for the development of PVDF/0.05HA, PVDF/0.1HA, PVDF/AgNO<sub>3</sub>, PVDF/HA/AgNO<sub>3</sub>, and PVDF composites. The distribution of particles, such as Ag, shows a uniform distribution, indicating good preparation of the composite. However, the distribution of the HA phase, while uniform, is not completely homogenous. This is due to the phase's insolubility in the solvent, causing these particles to distribute in the sample according to the principle of mixing, which may result in clustering.

**Table 3.5** Mapping results of four specimens

Ch. El.	Specimens			
	2 PVDF/0.1HA	4 PVDF/HA/Ag NO <sub>3</sub>	4 PVDF/HA/AgNO <sub>3</sub>	5 PVDF
F				
Ag				
Ca				

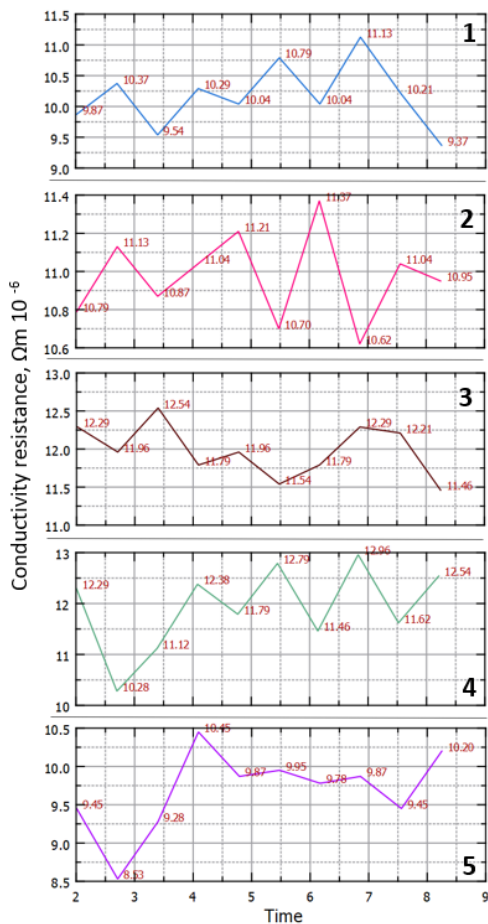


C



### 3.1.13. Conductivity resistance investigation

This subsection discusses the impact of PVDF, HA, and  $\text{AgNO}_3$  on the electrical resistance of composite films. Fig. 3.14 displays the electrical measurement results of four-point probe pulses.



**Fig. 3.14** Results of electrical measurement of four-point probe pulses: sample 1 – PVDF/0.05HA, sample 2 – PVDF/0.1HA, sample 3 – PVDF/ $\text{AgNO}_3$ , sample 4 – PVDF/HA/ $\text{AgNO}_3$ , sample 5 – PVDF

Four-point probe pulse measurement of the composite containing PVDF/0.01HA (sample 1) showed an average electrical resistivity of this composite of  $10.16 \times 10^{-6} \Omega\text{m}$  and a peak of  $11.13 \times 10^{-6} \Omega\text{m}$ . The incorporation of HA into the

composite increases the electrical resistivity. A larger change was observed with the addition of the AgNO<sub>3</sub> additive, with the highest peak recorded at  $12.54 \times 10^{-6} \Omega\text{m}$ .

The maximum increase in electrical resistance, reaching  $12.96 \times 10^{-6} \Omega\text{m}$ , was observed after adding all the materials. These results indicate that both AgNO<sub>3</sub> and HA can influence the electrical properties of the composite. In addition, AgNO<sub>3</sub> can lead to the formation of ionic species that can contribute to the overall conductivity. The results of sample 5 also show that the absence of phases had an impact on the decrease in electrical resistance. The sample containing only PVDF showed the highest result of  $10.45 \times 10^{-6} \Omega\text{m}$ . It is important to note that the conductivity resistance can also be influenced by other factors, such as the dispersion of additives in the composite and the processing conditions used. However, further studies are needed to elucidate the exact mechanisms responsible for the observed changes in electrical properties.

### 3.1.14. Mathematical model of dynamic investigation

The dynamic mathematical model uses COMSOL Multiphysics software. The goal is to determine the electrical potential of a frequency-stimulated material and compare it with the physical results obtained. A piezoelectric composite simulation is selected. The mathematical model consists of a deformed polymer composite model and a mathematically described composite. According to the provided geometric design parameters, a 2D finite element parametric model is performed in COMSOL, as shown in Figure 3.15. The composite material parameters are calculated according to the material property formulas. The piezoelectric cantilever 2D models are created using the Solid Mechanics module. The piezoelectric material PVDF parameters are sourced from COMSOL, and the composite additive material parameters were calculated. For the geometric model, fixed constraint boundary conditions are added to the fixed end of the beam, while the other ends remain free. The numerical model was created using the parameters determined for the PVDF/0.05HA/AgNO<sub>3</sub> sample, as shown in Table 3.6. Other models were determined and calculated based on their composition in the same way.

**Table 3.6** Parameters for the numerical model of the PVDF/0.05HA/AgNO<sub>3</sub> sample

Sample	Specimen thickness (piezoelectric layer), mm	Extracted energy (W/A)	$d_{33}, 10^{-12} \text{ C/N}$ (Force, 2 N)	$d_{31}$	Mass, g	Density kg/m <sup>3</sup>	Size of specimens, mm
PVDF/HA/AgNO <sub>3</sub>	0.18	0.09	8.3	3.32	0.19	0.08	30x80

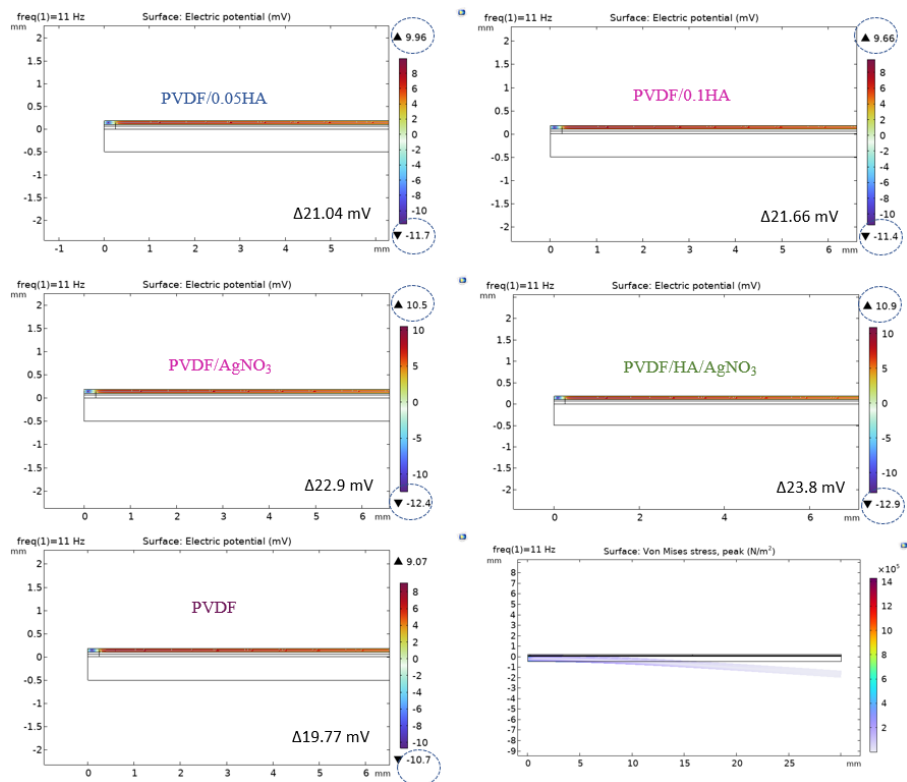
Natural frequency and deformation analyses were used to verify the model. The produced samples, with a thickness of 300  $\mu\text{m}$ , exhibit low resonant frequencies. Accordingly, at 11 Hz, the sample was stimulated to create the first eigenvalue, with the dynamic results indicating vibration at 11 Hz vibration mode 1. The theoretical results from COMSOL Multiphysics are presented in Fig. 3.15, which shows the electrical potential of the samples. Table 3.7 presents a comparison of the theoretical

and practical dynamic results, as well as the error in the theoretical and practical electric potential for each sample.

**Table 3.7** Theoretical and practical values comparison of dynamic investigation and electrical potentials

Model/ Samples	PVDF/ 0.05HA	PVDF/ 0.1HA	PVDF/ AgNO <sub>3</sub>	PVDF/HA/ AgNO <sub>3</sub>	PVDF
Measured electrical potential results	Δ19.46 mV	Δ19.61mV	Δ20.83 mV	Δ24.56 mV	Δ17.18 mV
Comsol theoretical electrical potential results	Δ21.04 mV	Δ21.66 mV	Δ22.9 mV	Δ23.8 mV	Δ19.77 mV
Error %	7.5%	9.46%	9.03%	3.19%	13.10%

The error in the results ranged from 3.19% to 13.10%, with the lowest error observed in the PVDF/HA/AgNO<sub>3</sub> sample.



**Fig. 3.15** Surface electrical potential of samples at a frequency of 11 Hz and deformation of the functional element

The simulation results showed an electric potential ranging between 19.77 to 23.8 mV. The composite can detect vibration. The highest electric potential results were shown by the PVDF/HA/AgNO<sub>3</sub> sample, reaching 23.48 mV. Therefore, the addition of the additional phase affects the electric potential. The PVDF sample alone showed an electric potential of 19.77 mV.

### 3.2. Development of PVDF-based materials with hydroxyapatite (HA), graphene oxide (GO), and silver nitrate (AgNO<sub>3</sub>)

This section investigates the influence of GO on the piezoelectric, electrical, and morphological properties of a PVDF-based composite for sensing applications. The focus is on the fabrication process of a functional element composed of PVDF, HA, GO, and AgNO<sub>3</sub>. The solvent casting method and non-toxic solvent DMSO were chosen for the fabrication of the functional element. This fabrication method and materials were chosen to increase the beta phase, which is very important for data protection and piezoelectric properties. The results of composites with PVDF, HA, GO, and AgNO<sub>3</sub> are presented in this section.

#### 3.2.1. Preparation of PVDF/HA/GO/AgNO<sub>3</sub> composites

The films were prepared using DMSO as a non-toxic solvent at 90 °C. The PVDF beads and DMSO solvent were first dissolved at 90 °C for about 5 hours until a homogeneous solution was formed. The AgNO<sub>3</sub>, GO, and HA components were then dispersed in the DMSO solvent at room temperature and stirred for 1–2 minutes until evenly distributed or dissolved. Finally, all components were mixed and poured onto the electrode substrate. The film was then formed using forming rods and dried in an oven at 65 °C for about 3 hours. The schematic representation of the sample preparation process is shown in Fig. 3.16.



**Fig. 3.16** Schematic methods of sample preparation

Table 3.8 presents the recipes for the specimens. Four different composites were prepared to evaluate the effect of each filler.

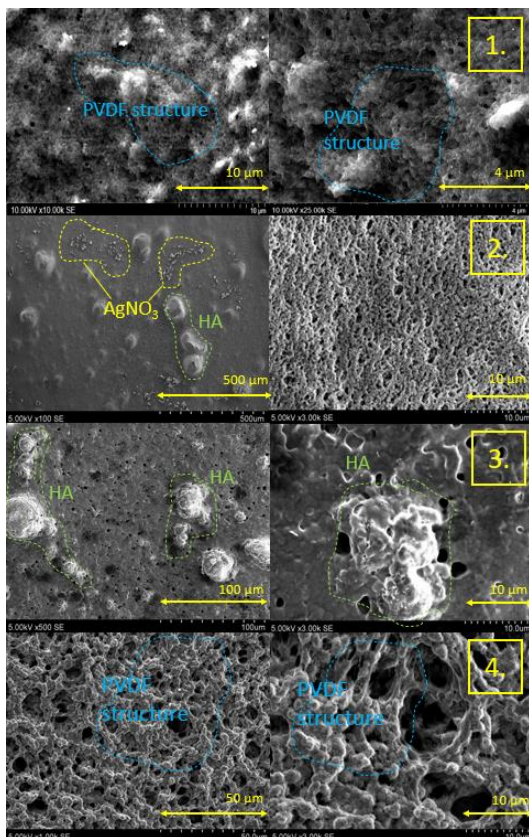
**Table 3.8** Concentrations of samples with PVDF/HA/GO/AgNO<sub>3</sub>

Sample No.	PVDF (g/ml)	HA (g/ml)	GO (g/ml)	AgNO <sub>3</sub> (g/ml)
(1)	0.3 g./2 ml.	-	0.3 g./1ml.	0.2 g./1ml.
(2)	0.3 g./2 ml.	0.1 g./1ml.	0.3 g./1ml.	-

(3)	0.3 g./2 ml.	0.1 g./1ml.	-	0.2 g./1ml.
(4)	0.3 g./2 ml.	0.1 g./1ml.	0.3 g./1ml.	0.2 g./1ml.

### 3.2.2. Morphology investigation with a scanning electron microscope (SEM)

The goal of this experiment was to create an amorphous phase, as PVDF is in a crystalline form, and the molecular chains are freely moving and do not have a stable structure, which negatively affects the electrical and piezoelectric properties. The reaction energy between the molecular chains of PVDF is higher than the reaction energy of the PVDF:DMSO interaction at low temperature (90 °C). According to X-ray diffraction and SEM images, the solvent enters the amorphous part of PVDF, while the crystalline part remains practically passive. The low temperature encourages the production of the  $\beta$  phase of PVDF, and the pores seen in the SEM images are the remains of evaporated DMSO. The topography of materials, which reveals surface textures, contours, and shapes, can be visualized at the nanometer scale. Detailed observations of a sample's surface structure are provided by SEM images, which are essential for studying materials such as metals, ceramics, and biological tissues. Fig. 3.17 shows the images acquired using SEM.

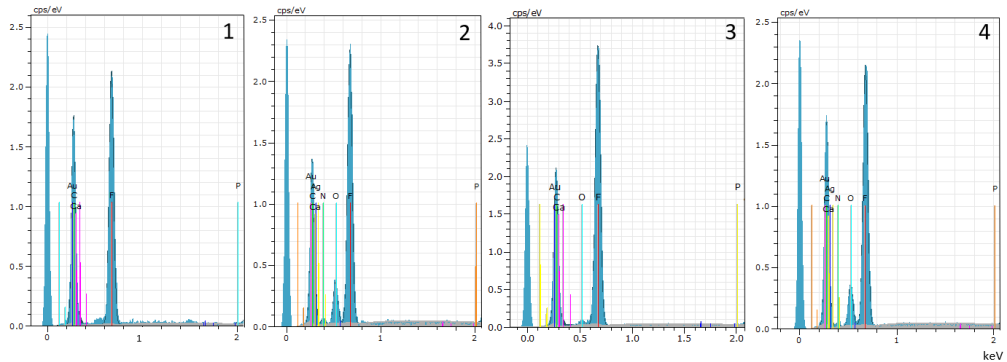


**Fig. 3.17** SEM analysis of each sample

Fig. 3.17 SEM images display the surface morphology of each sample, enabling the examination of various particles and revealing their size, shape, and arrangement. This aids in describing the uniformity of the sample and locating flaws. PVDF nanoparticles in sample 1 ranged in size from approximately 4  $\mu\text{m}$  to 10  $\mu\text{m}$ . Sample 2 showed a porous surface structure with HA and silver nanoparticles. HA nanoparticles ranging in size from 15  $\mu\text{m}$  to 40  $\mu\text{m}$  can be seen on the porous surface of sample 3. Additionally, a thin film in sample 4 contains a network of tiny, connected holes or pores throughout the substance. These pores, which typically vary in size and distribution, contribute to the high surface area, benefiting applications such as filtration or sensors that require more interaction with the surrounding media. Because thin films are porous, the material can be flexible and lightweight while maintaining strong mechanical stability and chemical resistance. The degree of porosity can also affect characteristics such as hydrophobicity, ion permeability, and dielectric behavior, making it adaptable for a range of applications.

### 3.2.3. Chemical components analysis by energy dispersive X-ray (EDX) and mapping methods

The surface chemical composition of the samples was determined using EDX analysis, which can detect concentrations as low as 0.001 percent. The normal concentration (mass %) of chemical components is presented in Table 3.9. Fig. 3.18 shows the chemical element peaks for each sample.



**Fig. 3.18** EDX graph results of each sample

**Table 3.9** Chemical composition of specimens

Content of chemical elements	Specimens											
	1			2			3			4		
	PVDF/AgNO <sub>3</sub> /GO			PVDF/HA/AgNO <sub>3</sub>			PVDF/HA/GO			PVDF/HA/AgNO <sub>3</sub> /GO		
	wt.%	at.%	error (%)	wt.%	at.%	error (%)	wt.%	at.%	error (%)	wt.%	at.%	error, %
Carbon	32.22	54.12	2.97	24.60	39.07	2.79	36.36	50.07	5.18	29.49	44.82	2.80
Oxygen	5.09	6.42	0.77	8.15	9.71	1.29	1.37	1.42	0.46	8.22	9.38	1.09
Fluorine	30.19	32.07	2.85	43.83	44.01	4.25	54.56	47.49	7.03	40.72	39.13	3.59
Silver	25.39	4.75	0.67	10.99	1.94	0.43	-	-	-	8.39	1.42	0.30



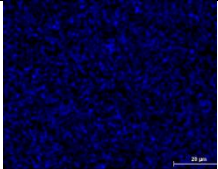
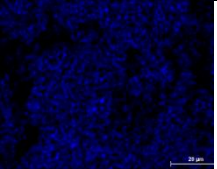
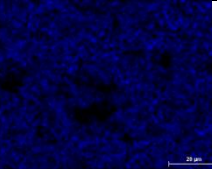
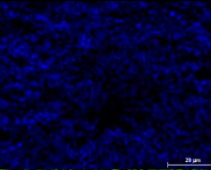
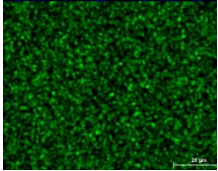
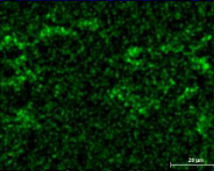
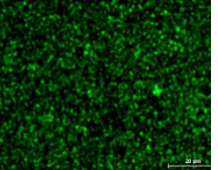
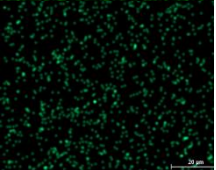
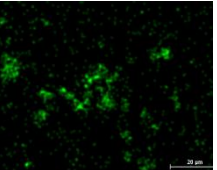
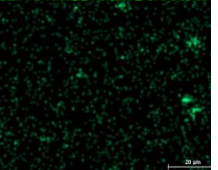
Gold	5.68	0.58	0.23	6.62	0.64	0.31	6.63	0.56	0.40	5.87	0.54	0.24
Calcium	-	-	-	3.71	1.77	0.24	0.92	0.38	0.14	5.68	2.59	0.24
Nitrogen	1.43	2.06	0.41	2.10	2.86	0.69	-	-	-	1.62	2.11	0.48
Phosphorus	-	-	-	0.00	0.00	0.00	0.16	0.08	0.05	0.00	0.00	0.00

*The composition is given for chemical elements of normal concentration (wt.%) and atomic concentration (at.%) without the chemical element hydrogen (hydrogen cannot be detected using the EDX method).*

The results showed that the primary chemical elements—carbon, oxygen, fluorine, silver, gold, calcium, nitrogen, and phosphorus—composed the top layer of the examined specimens, as shown in Table 4.7. Furthermore, no new components or contaminants were found. Subsequent investigation showed that sample 1, the specimen devoid of HA, was phosphate and calcium-free. Additionally, it was discovered that elemental silver and nitrogen were absent from sample 3, the specimen that lacked AgNO<sub>3</sub>. As a result, the EDX analysis verified that the four distinct specimens had been prepared successfully. The observed results lend credence to the notion that PVDF/AgNO<sub>3</sub>/GO, PVDF/HA/AgNO<sub>3</sub>, and PVDF/HA/AgNO<sub>3</sub>/GO composites free of unwanted impurities can be produced utilizing the suggested solvent casting process (as a solvent employing DMSO).

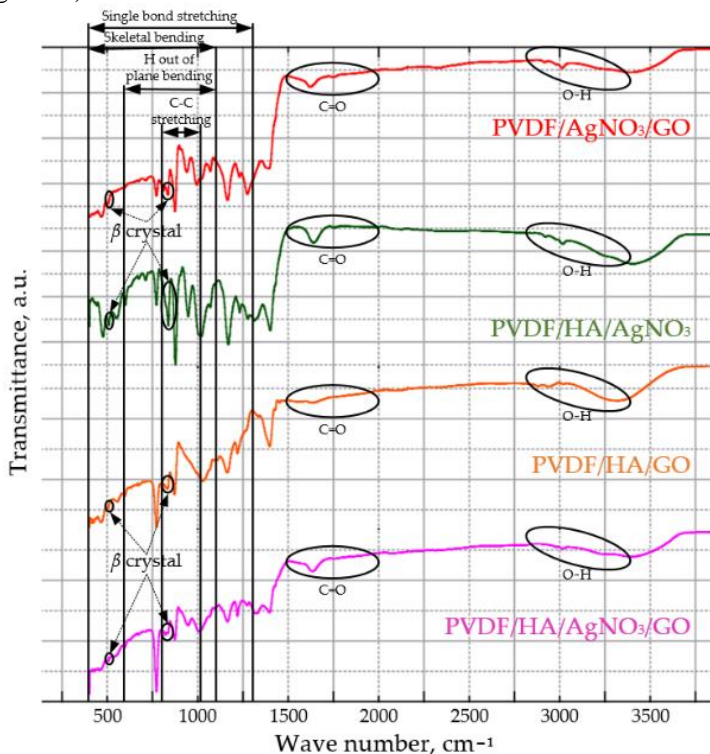
The EDX analysis identified chemical elements including C, O, F, Ag, Au, Ca, N, and P, indicating that the samples were successfully produced. The elements C, O, N, and P were evenly spaced. Nevertheless, not every sample had the same distribution of F, Ag, and Ca elements on the composite's surface. Table 3.10 presents the mapping findings of four specimens.

**Table 3.10** Mapping results of four specimens

Specimens				
	1 PVDF/AgNO <sub>3</sub> /GO	2 PVDF/HA/AgNO <sub>3</sub>	3 PVDF/HA/GO	4 PVDF/HA/AgNO <sub>3</sub> /GO
Fluorine				
Silver				
Calcium				

### 3.2.4. Investigation of chemical properties and $\beta$ -phase transformation

The next stage of the study involved investigating the FTIR spectra of the four specimens (Fig. 3.19).



**Fig. 3.19** FTIR spectrum of PVDF/AgNO<sub>3</sub>/GO, PVDF/HA/AgNO<sub>3</sub>, PVDF/HA/GO, and PVDF/HA/AgNO<sub>3</sub>/GO specimens

The FTIR spectra of the samples exhibit a strong association with one another. Bands associated with the  $\alpha$  and  $\beta$  phases of PVDF are most frequently found in the spectra at 537, 724, 734, and 895 cm<sup>-1</sup> [71, 74]. The main basic compositions of HA, such as PO<sub>4</sub><sup>3-</sup>, might overlap with the  $\alpha$ - and  $\beta$ -phases of PVDF when considering the amorphous phases of the specimens. This occurs because PO<sub>4</sub><sup>3-</sup> has an impact on the vibrational modes of 731, 1024, and 1088 cm<sup>-1</sup> [47, 81]. According to the observed spectra, the vibrational bands of the PVDF  $\beta$ -phase were located at 510 and 840 cm<sup>-1</sup> [49]. Furthermore, every sample in the 1375–1982 cm<sup>-1</sup> range contains C–O bonds [43]. The C–F bond is responsible for the stretching bond at 1340 cm<sup>-1</sup>. The presence of -OH groups is indicated by the broad range of wavenumber values from 2787 to 3548 cm<sup>-1</sup>. The FTIR spectrum did not reveal any discernible effects of GO, AgNO<sub>3</sub>, and HA due to their low concentration and the low crystallization temperature (90 °C). In essence, the components of the composites were validated by FTIR spectra, and all specimens were shown to exhibit the PVDF  $\beta$  crystalline phase.

The presence of both phases ( $\alpha$  and  $\beta$ ) was observed in the FTIR diagrams. To determine the proportion of the  $\beta$ -phase present in each sample, the IR absorption

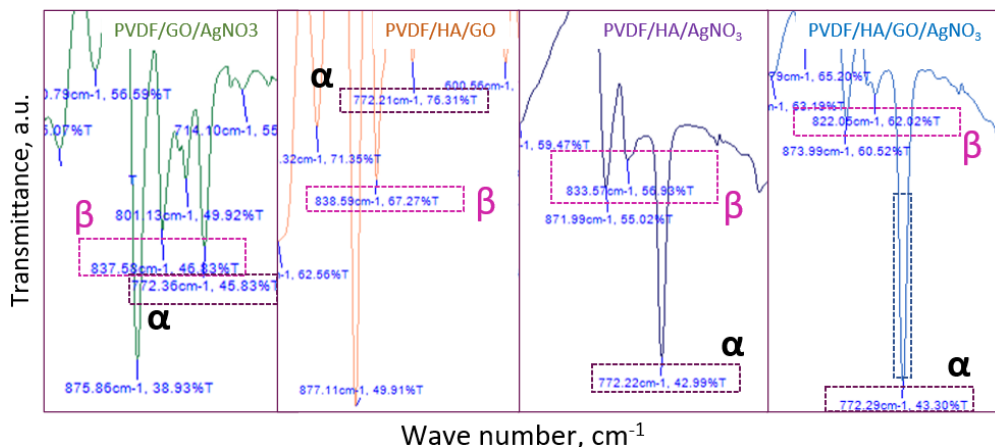


bands at 763 and 840  $\text{cm}^{-1}$ , characteristic of the  $\alpha$ - and  $\beta$ -phases, respectively, were examined. Table 3.11 presents the  $\beta$ -phase concentrations and calculation data for the samples. Higher  $\beta$ -phase concentrations were observed in the PVDF/HA/AgNO<sub>3</sub> and PVDF/HA/GOAgNO<sub>3</sub> samples. The results demonstrate that the addition of additional phases such as HA, GO, or AgNO<sub>3</sub> affects the  $\beta$ -phase transformation in the composites.

**Table 3.11.**  $\beta$  concentrations of samples with PVDF, HA, GO, and AgNO<sub>3</sub>

Sample	$\alpha$ ( $\text{cm}^{-1}$ )	$\beta$ ( $\text{cm}^{-1}$ )	$\sim K$ (840/763)	$\beta$ (%)
PVDF/GO/AgNO <sub>3</sub>	45.83	46.83	$\sim 1.1$	48.15
PVDF/HA/GO	76.31	67.27	$\sim 1.1$	44.48
PVDF/HA/AgNO <sub>3</sub>	42.99	56.93	$\sim 1.1$	54.63
PVDF/HA/GO/AgNO <sub>3</sub>	43.30	62.02	$\sim 1.1$	56.76

The  $\beta$ -phase measurement was performed using IR absorption. According to the Lambert-Beer law, the relative fraction of the  $\beta$  phase was calculated for each sample. Fig. 3.20 presents the peaks of the  $\alpha$  and  $\beta$  phases for each specimen.



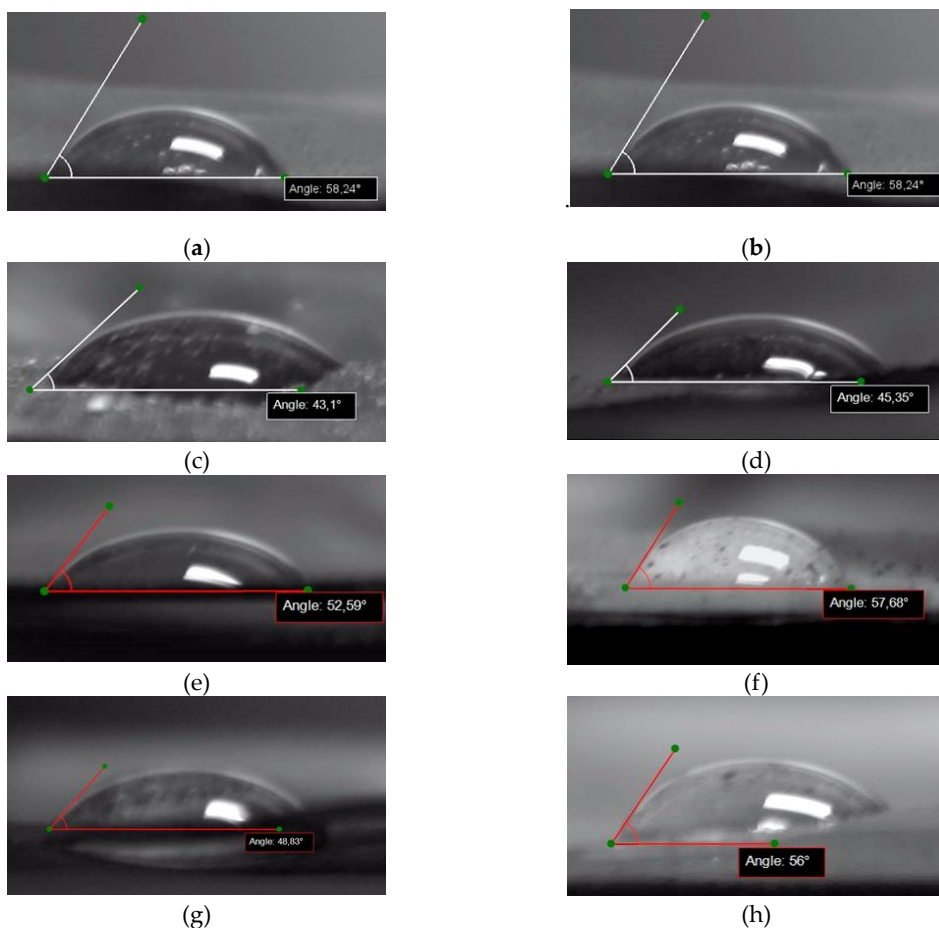
**Fig. 3.20** FTIR spectrum of  $\alpha$ - and  $\beta$ -phases in PVDF/AgNO<sub>3</sub>/GO, PVDF/HA/AgNO<sub>3</sub>, PVDF/HA/GO, and PVDF/HA/GO/AgNO<sub>3</sub>

This calculation results in the ferroelectric phase accounting for approximately 50% of the total crystalline phase of the nanoparticles. A ferroelectric response is observed from the combined analysis of X-ray diffraction and IR spectroscopy experiments.

### 3.2.5. Hydrophilic properties analysis and results

The contact angle between a drop of water and a drop of glycerol on the surfaces of several samples was measured using a contact angle goniometer. Distilled water is commonly used in drop liquid contact angle measurements to evaluate hydrophilicity for several reasons: water's high surface tension highlights the distinction between hydrophilic and hydrophobic interactions; its high polarity makes it sensitive to surface energy changes, allowing it to spread well on hydrophilic surfaces; and it is free of impurities, ensuring that contaminants do not interfere with measurements. As

a result, water is a perfect testing medium for real-world relevance in many applications involving hydrophilic surfaces, such as in biomedical or environmental domains. Glycerol, the other liquid used in the experiment, was chosen for its unique qualities that enhance water measurements. It is less volatile than water, forms a stable droplet that does not evaporate quickly, and, in certain situations, allows for a more thorough analysis of surface properties, increasing the accuracy of hydrophilicity measurements. Additionally, glycerol has a higher surface tension than water, making it more sensitive to subtle surface energy variations on the substrate, helping to provide a clearer contrast between hydrophilic and hydrophobic surfaces. Fig. 3.21 shows the angles measured during the experiment between a drop of water and glycerol on thin solid film samples.



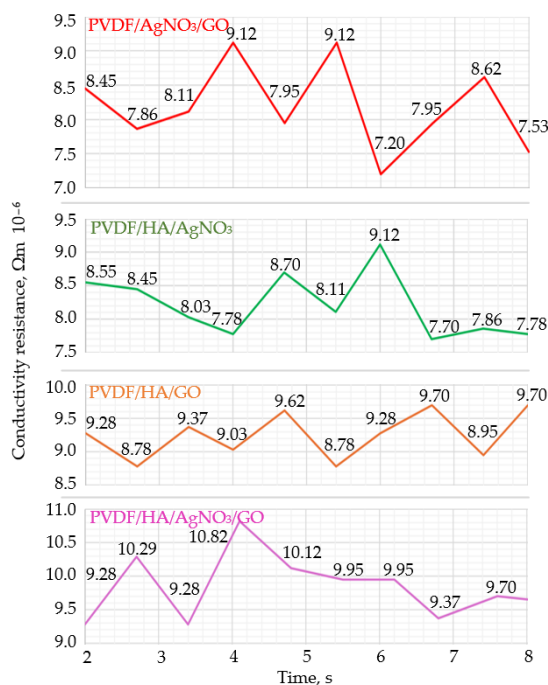
**Fig. 3.21** Drop liquid angle measurements: (a) water drop on sample 1, (b) sample 2, (c) sample 3, (d) sample 4, and (e) glycerol drop on sample 1, (f) sample 2, (g) sample 3, (h) sample 4

Every measured angle falls within a range that defines the related processes. For example, the adhesion phenomenon occurs when the contact angle is less than 90 degrees. There is no adhesion between the liquid and solid surfaces if the contact angle

is 90 degrees or greater. As indicated by the results, the hydrophilicity of all measured samples using distilled water and glycerol was confirmed. Sample 1 had an average contact angle of  $\approx 58^\circ$  for water and  $\approx 52^\circ$  for glycerol; sample 2 had an average contact angle of  $\approx 53^\circ$  for water and  $\approx 58^\circ$  for glycerol; sample 3 had an average contact angle of  $\approx 43^\circ$  for water and  $\approx 49^\circ$  for glycerol; sample 4 had an average contact angle of  $\approx 45^\circ$  for water and  $\approx 56^\circ$  for glycerol. The high hydrophilicity of the newly developed composite thin films is crucial for biodegradation, tissue engineering, and drug delivery applications because it affects water entry, fluid transport, and pharmacokinetics.

### 3.2.6. Electrical investigation of four-point probe pulses

This subsection discusses the impact of PVDF, HA,  $\text{AgNO}_3$ , and GO on the electrical resistance of composite films. Fig. 3.22 presents the findings of the electrical measurements obtained using four-point probe pulses.



**Fig. 3.22** Results of electrical measurements using four-point probe pulses

The composite including PVDF/ $\text{AgNO}_3$ /GO had an average electrical resistance of  $8.20 \times 10^{-6} \Omega\text{m}$ , according to four-point probe pulse measurements. The addition of HA to the composite, while removing GO, did not cause any notable modifications, with an average resistance of  $8.21 \times 10^{-6} \Omega\text{m}$ . However, when GO was added and the  $\text{AgNO}_3$  additive was eliminated, a more significant change was observed, with the composite's average electrical resistivity increasing to  $9.25 \times 10^{-6} \Omega\text{m}$ .

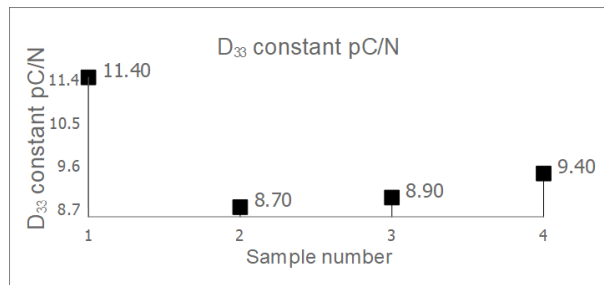
When all the materials were added, the electrical resistance increased the most, reaching  $10.82 \times 10^{-6} \Omega\text{m}$ . These findings suggest that GO and  $\text{AgNO}_3$ —particularly GO—may have a more significant impact on the composite's electrical characteristics

than HA. One possible explanation for these trends is the interaction between the minerals and the PVDF polymer chains. GO can help with charge transmission in the composite because it is a highly conductive substance with a wide surface area. Furthermore,  $\text{AgNO}_3$  may introduce ionic species that can increase the total conductivity.

It is crucial to remember that other elements, such as the way additives are distributed throughout the composite and the processing conditions employed, can also affect the conductivity resistance. Nevertheless, further research is required to pinpoint the precise processes causing the noted modifications in electrical characteristics.

### 3.2.7. Piezoelectric coefficient ( $d_{33}$ ) measurement results

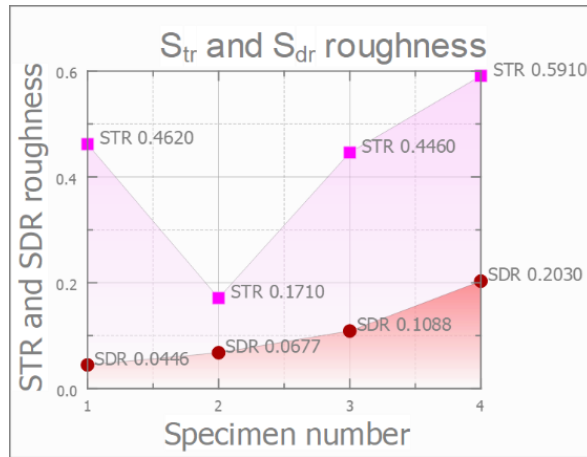
A static piezoelectric meter was used to measure the  $d_{33}$  values of the developed piezoelectric composites. When an electric field acts in the polarization direction (typically in three directions), a material with a high  $d_{33}$  value can induce high mechanical stress. In this study, all samples were measured under the same force [ $\pm 1$ – $2$  N]. For sample 2, the piezoelectric meter displayed the lowest reading of 8.70 pC/N. Sample 1 exhibited the highest findings, with a temperature of 11.40 pC/N. The addition of graphene results in slight variations in the constant, while the addition of silver in sample 3 (8.90 pC/N) causes an increase in the constant in a proportion of 0.20 pC/N. The addition of the sample including GO and  $\text{AgNO}_3$  phases continues to produce the highest result, even though Sample 4, which has all the components, exhibits a steady increase, reaching 9.40 pC/N. Sample results for piezoelectric  $d_{33}$  constants are presented in Fig. 3.23.



**Fig. 3.23**  $d_{33}$  measurement results: sample 1 – PVDF/ $\text{AgNO}_3$ , GO, sample 2 – PVDF/HA/ $\text{AgNO}_3$ , sample 3 – PVDF/HA/GO, and sample 4 – PVDF/HA/ $\text{AgNO}_3$ /GO

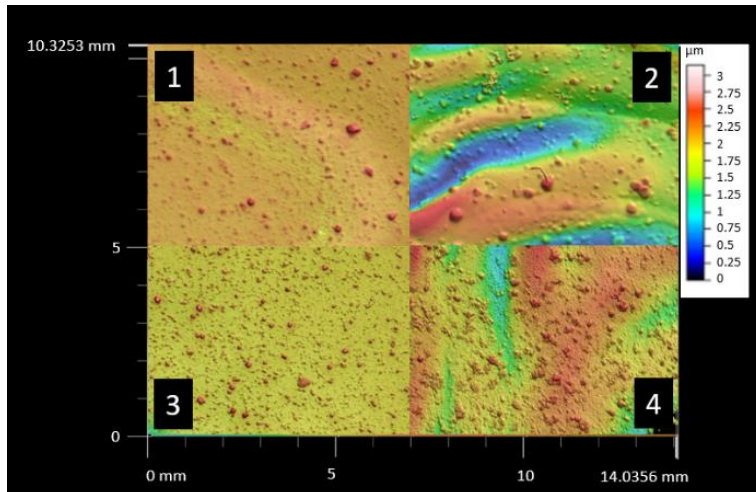
### 3.2.8. Surface roughness properties and results

Fig. 3.24 shows the correlation between surface roughness levels as measured by Str. Sample 4 exhibited the highest Str value of 0.5910 among all samples, which was influenced by the addition of GO and HA phases. In contrast, Sample 2 had the lowest Str value of 0.1710. The Sdr results followed a similar trend; however, sample 1, which did not contain HA nanoparticles, showed the lowest roughness. Sample 4 showed the highest Sdr value of 0.2030.



**Fig. 3.24** Str (texture aspect ratio) and Sdr (developed interfacial area ratio)

The interaction of different material layers or surface roughness often has a significant impact on the properties of thin films, such as dielectric characteristics. Surface roughness can complicate electrical phenomena and affect their consistency and stability. In general, less roughness is needed to reduce the loss of both acoustic and optical signals. Fig. 3.25 shows the surface estimation of the surface roughness. The addition of phases affects the surface roughness of HA and GO, as these materials do not dissolve in DMSO but rather disperse, showing more pronounced areas of dispersion and aggregation. The distribution of these details is fairly even. In sample 2, the largest height changes, but this is not due to the influence of particles; instead, it results from the differentiation in the thicknesses of the forming film.



**Fig. 3.25** Surface roughness images of samples 1–4

### 3.3. Chapter conclusions

1. The films (with PVDF, HA, and AgNO<sub>3</sub>) were obtained using DMSO as a solvent at 90 °C. FTIR spectra confirmed that the  $\beta$  phase of PVDF at 1193 cm<sup>-1</sup> helped to enhance the 1046 cm<sup>-1</sup> band. The electrical characteristics of the prepared samples were investigated, and the samples containing all components (PVDF/HA/AgNO<sub>3</sub>) exhibited the highest energy recovery values, ranging from 56.50 to 125.20 mV. For PVDF, the piezoelectric meter showed the lowest result of 5.6 pC/N at a force of 2 N, which was continuously decreasing. Similarly, the PVDF/HA/AgNO<sub>3</sub> sample exhibited good results, with a  $d_{33}$  constant of 8.3 pC/N at a force of 2 N. The loading force of 2 N provided the best results. The dynamic results showed that the PVDF/HA/AgNO<sub>3</sub> functional element generated the highest signal. Additional components, such as AgNO<sub>3</sub> and HA, gradually increased the signal. Four-point probe measurement revealed that the inclusion of HA in the composite increased the electrical resistance. A larger change was observed with the addition of the AgNO<sub>3</sub> additive, with the highest peak recorded at  $12.54 \times 10^{-6} \Omega\text{m}$ . After adding all the materials, the maximum increase in electrical resistivity was  $12.96 \times 10^{-6} \Omega\text{m}$ . These results suggest that AgNO<sub>3</sub> and HA can affect the electrical properties of the composite.

2. At an ideal temperature of 90 °C, DMSO was used as a solvent to create films containing PVDF, HA, GO, and AgNO<sub>3</sub>. All samples with CO and OH bonds had the PVDF  $\beta$  crystalline phase, as confirmed by FTIR studies. According to the results of electrical measurements, the maximum increase in electrical resistance was observed in the PVDF/HA/AgNO<sub>3</sub>/GO sample (sample 4), with a value of  $10.82 \times 10^{-6} \Omega\text{m}$ . However, sample 1 (PVDF/AgNO<sub>3</sub>/GO) showed the best piezoelectric results ( $d_{33}$ ), with a value of 11.40 pC/N, while sample 4 (PVDF/HA/AgNO<sub>3</sub>/GO) had a  $d_{33}$  of 9.40 pC/N. Based on the obtained results, new composite materials consisting of AgNO<sub>3</sub>, HA, GO, and PVDF were developed, exhibiting excellent piezoelectric properties and high hydrophilicity. These materials also exhibit  $\beta$  phase transformation.

## 4. APPLICATION AND INTEGRATION OF A PIEZOELECTRIC COMPOSITE MATERIAL

The composite being developed holds potential for use in information security applications. Since attackers can compromise sensing technology, it is necessary to first analyze the possible threats and identify ways to protect the information flow in the application. Biosensors handle confidential information, which must be protected against potential attacks. Therefore, the following section discusses the threats that can be detected in sensors and their devices used in medicine, as well as strategies for protecting information flow from attackers.

After manufacturing and measuring the characteristics of both composites, the FTIR peaks and SEM morphology results are compared to assess the  $\beta$ -phase transformation and the influence of solid particles. The electrical results from the four-point probes and piezoelectric measurements are also compared. One of the goals of the dissertation is to evaluate the application and integration possibilities of a functional element that ensures cybersecurity. Therefore, the integration possibilities of this functional element are presented.

### 4.1. Comparison of the results of the created composites and the influence of graphene oxide (GO) on their properties

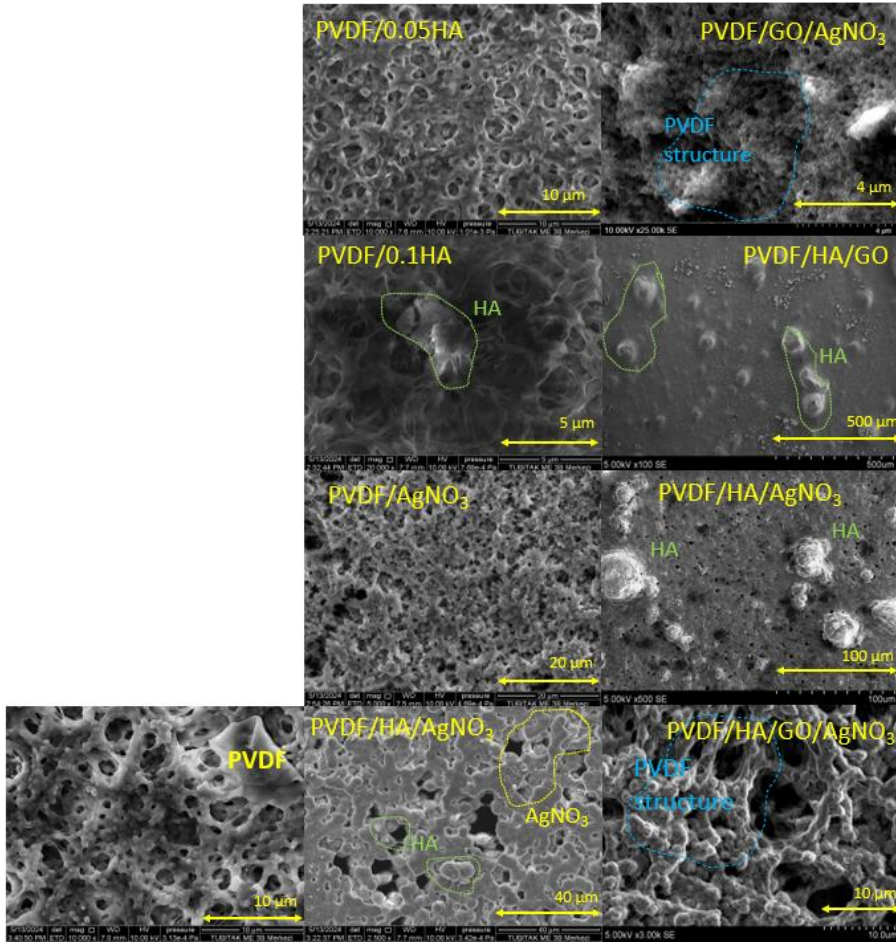
Table 4.1 presents the composites and their concentrations that were produced, while this section compares several measurement results.

**Table 4.1.** Concentrations and recipes of samples

Sample	Recipes (g/ml)
PVDF/0.05HA	PVDF 0.5 g / 2 ml, HA 0.05 g / 1 ml
PVDF/0.1HA	PVDF 0.5 g / 2 ml, HA 0.10 g / 1 ml
PVDF/AgNO <sub>3</sub>	PVDF 0.5 g / 2 ml, AgNO <sub>3</sub> 0.2 g / 1 ml
PVDF/HA/AgNO <sub>3</sub>	PVDF 0.5 g / 2 ml, HA 0.05 g / 1 ml, AgNO <sub>3</sub> 0.2 g / 1 ml
PVDF	PVDF 0.5 g / 2 ml
PVDF/GO/AgNO <sub>3</sub>	PVDF 0.3 g / 2 ml, GO 0.3 g / 1 ml, AgNO <sub>3</sub> 0.3 g / 1 ml
PVDF/HA/GO	PVDF 0.3 g / 2 ml, HA 0.1 g / 1 ml, GO 0.3 g / 1 ml
PVDF/HA/AgNO <sub>3</sub>	PVDF 0.3 g / 2 ml, HA 0.1 g / 1ml, AgNO <sub>3</sub> 0.3 g / 1 ml
PVDF/HA/GO/AgNO <sub>3</sub>	PVDF 0.3 g / 2 ml, HA 0.1 g / 1 ml, GO 0.3 g / 1 ml, AgNO <sub>3</sub> 0.3 g / 1 ml

According to the SEM photographs, PVDF is in crystalline form; however, the solvent penetrates the amorphous portion of PVDF, as the experiment aims to produce an amorphous phase. The crystalline portion, on the other hand, remains essentially inactive. The pores observed in the SEM images are the remains of evaporated DMSO, as low temperatures encourage the formation of the  $\beta$  phase of PVDF. SEM images of the PVDF/HA/AgNO<sub>3</sub> and PVDF/HA/GO/AgNO<sub>3</sub> composites, shown in Fig. 4.1, demonstrate that the amorphous phase predominates in both composites and that all the samples exhibit developed pores.

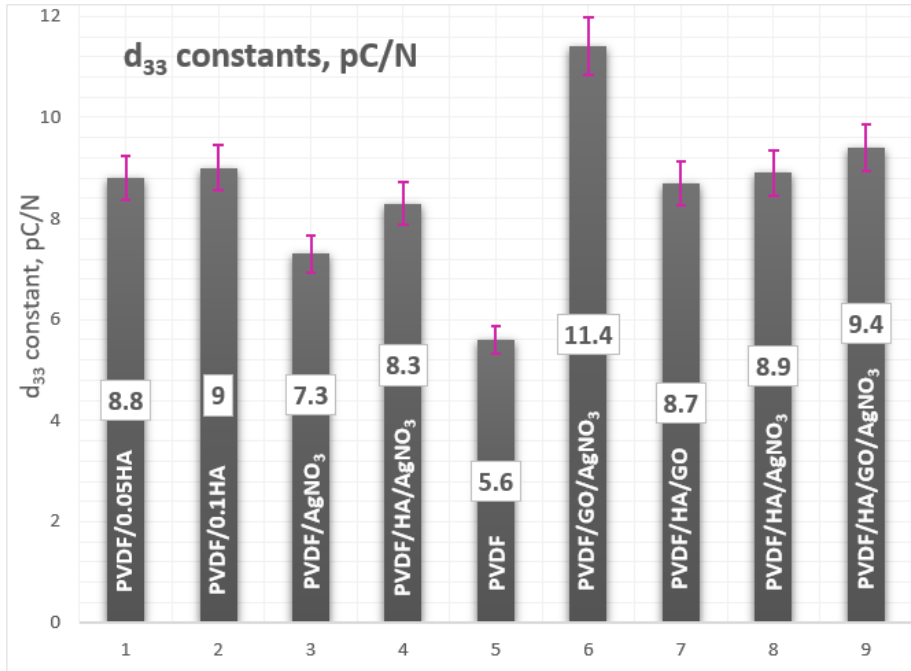




**Fig. 4.1** Comparison of SEM images of composites

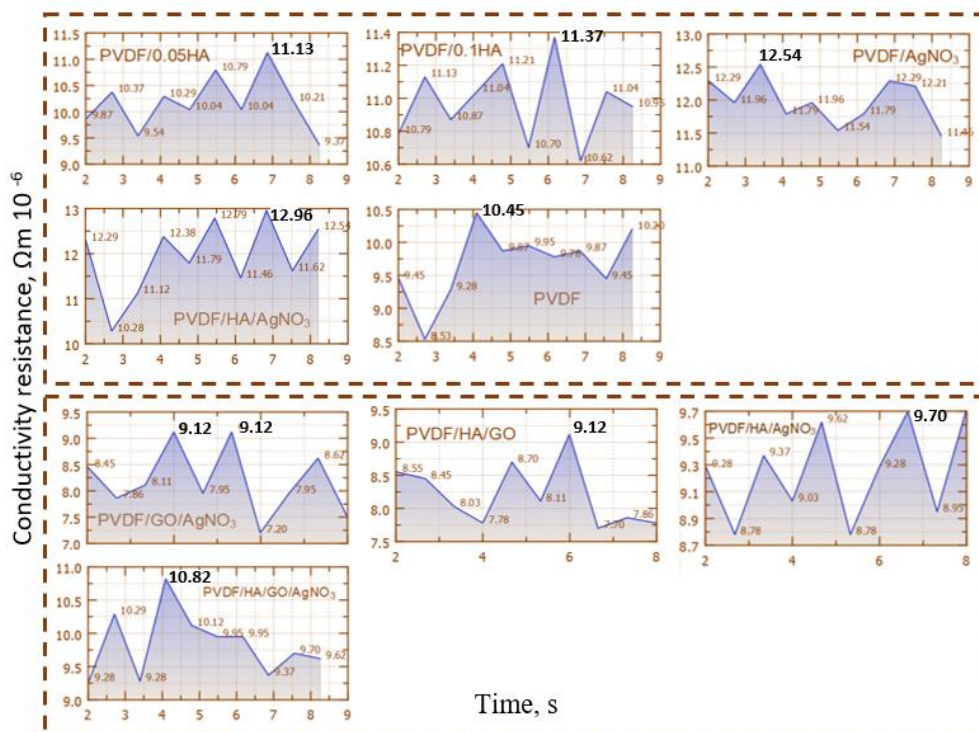
Fig. 4.2 shows the  $d_{33}$  constant results for both composites. The highest constant, 11.40 pC/N, is found in the PVDF/GO/AgNO<sub>3</sub> composite. The PVDF/HA/GO/AgNO<sub>3</sub> sample also shows good results, with a  $d_{33}$  of 9.40 pC/N. The lowest results are observed for the sample containing pure annealed PVDF, indicating that the addition of phases such as GO, AgNO<sub>3</sub>, and HA affects the  $d_{33}$  constant results.





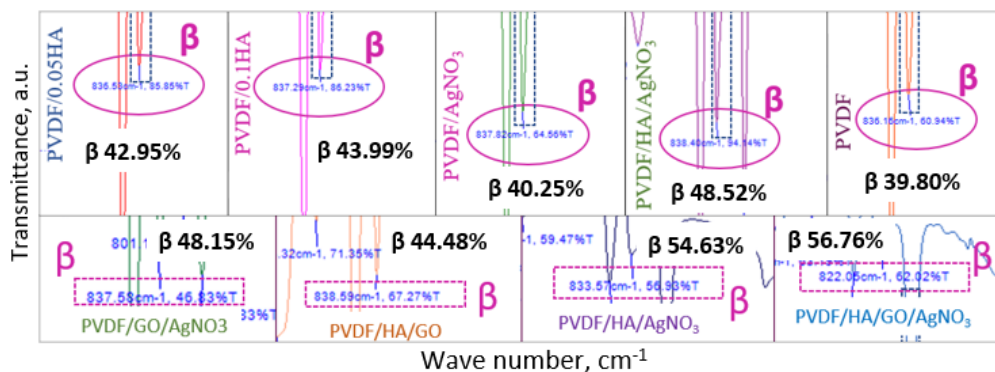
**Fig. 4.2** Comparison of  $d_{33}$  piezoelectric constants for all samples

Fig. 4.3 shows the electrical results of the four-probe measurements. The highest results were demonstrated by samples with PVDF/HA and samples with PVDF/AgNO<sub>3</sub>. The maximum increase in electrical resistance of  $12.96 \times 10^{-6} \Omega\text{m}$  was observed after adding all materials. The incorporation of HA into the composite increased the electrical resistivity. When all the materials were added to the PVDF/HA/AgNO<sub>3</sub>/GO sample, the electrical resistance increased by  $10.82 \times 10^{-6} \Omega\text{m}$ . AgNO<sub>3</sub> can lead to the formation of ionic species that can contribute to the overall conductivity.



**Fig. 4.3** Electrical conductivity results from four-probe measurements; comparison of all samples

The FTIR spectrum did not reveal a significant effect of  $\text{AgNO}_3$ , GO, and HA due to their low concentration and the low crystallization temperature ( $90^\circ\text{C}$ ). The components of the composites were essentially confirmed by the FTIR spectra. All samples were found to contain the PVDF  $\beta$ -crystalline phase according to the visible FTIR peaks. The  $\beta$ -phase concentrations were calculated and are presented in Fig. 4.4. The highest  $\beta$ -phase concentrations were found in the PVDF/HA/AgNO<sub>3</sub> and PVDF/HA/GO/AgNO<sub>3</sub> samples, ranging from 54.63% to 56.76%.

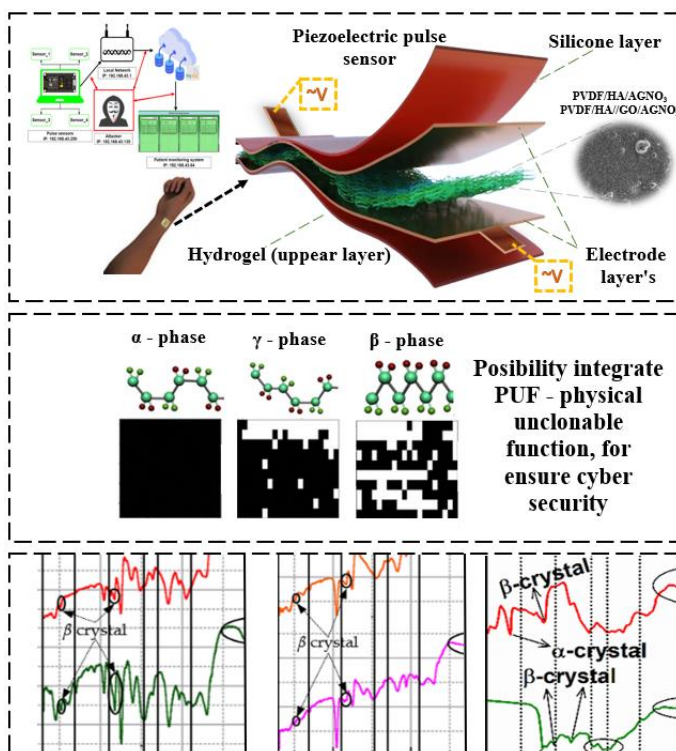


**Fig. 4.4** Comparison of FTIR spectrum results for all samples

## 4.2. Application and integration of a functional element

The study presented focuses on the final application: the multilayer biosensor design. In addition to the design of the biosensor functional element itself, it is also important to consider the whole with which it will interact. Fig. 4.5 shows the design of the biosensor in a sensing device application. One layer of the biosensor is a functional element with two electrodes. The properties of the hydrogel, such as high flexibility, were determined. The hydrogel helps the sensor to come into closer contact with human skin, and the PVDF/HA/AgNO<sub>3</sub> or PVDF/HA/GO/AgNO<sub>3</sub> sensing material was chosen for its excellent piezoelectricity and plasticity. Two copper strips of silver paste were placed on both sides of the electrode conductor to ensure good conductivity and a wire was soldered on them for connection. The entire device was completely covered with a layer of silicone on both sides to increase mechanical strength and protect against dust and water.

The developed functional element is perfectly suited for pulse measurement. The FTIR peaks and results perfectly revealed the existence of the  $\beta$  phase in the samples, which means that the additional materials and the chosen processing method are perfectly suited to increase the  $\beta$  phase and the properties required for the functional element application. The  $\beta$  phase is also needed to integrate a PUF key, which would ensure secure use of the functional element and protect patient data.



**Fig. 4.5** Piezoelectric pressure sensor structure, PUF in  $\beta$ -phase, and FTIR peaks of  $\beta$ -phase in created functional elements

### 4.3. Chapter conclusions

1. The comparison results showed that the electrical characteristics of the prepared samples were investigated. The highest energy recovery values were observed in the samples containing the PVDF/HA/AgNO<sub>3</sub> components, ranging from 56.50 to 125.20 mV. The PVDF sample showed the lowest result of 5.6 pC/N, while the constant of the PVDF/HA/AgNO<sub>3</sub> sample was 8.3 pC/N. These results demonstrate the influence of the added phases. PVDF/AgNO<sub>3</sub>/GO showed the best piezoelectric findings ( $d_{33}$ ), with a value of 11.40 pC/N. The four-point probe measurement revealed that the inclusion of HA and AgNO<sub>3</sub> in the composite increased electrical resistance to  $12.96 \times 10^{-6} \Omega\text{m}$ . The addition of GO also increased electrical resistance, reaching  $10.82 \times 10^{-6} \Omega\text{m}$  in the PVDF/HA/AgNO<sub>3</sub>/GO sample. FTIR spectra showed that all samples contained the PVDF  $\beta$ -crystalline phase according to the visible FTIR chemical peaks, with the additional phases contributing to the increase in the peaks.

2. The combination of PVDF, GO, HA, and AgNO<sub>3</sub> shows great potential for the development of composites due to its stability in this study. This leads to the creation of new high-performance composites that can be applied in wearable electronics, energy harvesting, self-propelled sensors, and, most importantly, biomedicine or its products. The  $\beta$  phase is also needed to integrate the PUF key, which would ensure the safe use of the functional element and protect patient data.

## 5. CONCLUSIONS

1. After investigating the security gaps in the wireless infrastructure of piezoelectric biosensors used in the medical field, it was found that the information used in these sensors is a target for attacks. In medicine, flexible and implantable sensors handle various types of data that can be detected and changed. By integrating the PUF key into the PVDF  $\beta$  phase, it is possible to protect the information obtained through sensors. However, the functionality and applicability of the piezoelectric composite in forming biomechanical sensors are equally important. HA, GO, and AgNO<sub>3</sub> nanoparticles were selected to enhance functionality and control mechanical, electrical, morphological, and hydrophobic properties. In piezoelectric composites, HA ensures biocompatibility and increases the piezoelectric effect, GO improves electrical properties and promotes the  $\beta$ -phase transformation in a PVDF polymer, and AgNO<sub>3</sub> has not only antibacterial properties but also improves charge transfer. Such composites have not been previously analyzed; therefore, this study aims to develop a functional element that ensures mechanical, electrical, and piezoelectric properties and ensures the security of transmitted data.

2. A synthesis methodology for a piezoelectric composite based on PVDF with HA, GO, and AgNO<sub>3</sub> nanoparticles was developed to ensure the integration of piezoelectric properties and  $\beta$ -phase transformation in the composite material. The synthesis procedure was developed on solvent casting with DMSO (90 °C, 5 h). Samples of various materials and concentrations were prepared on 0.05 mm steel electrodes. The film was deposited on an electrode with a thickness of 0.17 mm. Surface roughness analysis and multifractal spectra confirmed the good quality of the sample preparation.

3. The investigation showed the influence of HA and AgNO<sub>3</sub> nanoparticles on the electrical, mechanical, and morphological properties of the piezoelectric composite and the provision of  $\beta$ -phase transformation. In the PVDF/HA/AgNO<sub>3</sub> composite, the constant  $d_{33}$  was 8.3 pC/N and increased by 33%. Electrical characteristics analysis showed that the highest energy values were observed in the PVDF/HA/AgNO<sub>3</sub> component, ranging from 56.50 to 125.20 mV. The four-point probe measurements indicated that the inclusion of HA and AgNO<sub>3</sub> in the composite increased electrical resistance to  $12.96 \times 10^{-6} \Omega\text{m}$ . The highest  $\beta$ -phase transformation was recorded in the PVDF/HA/AgNO<sub>3</sub> samples.

4. The investigation revealed the influence of GO on the piezoelectric, electrical, and morphological properties of the PVDF-based composite. The PVDF/AgNO<sub>3</sub>/GO sample exhibited the best piezoelectric findings at 11.40 pC/N. FTIR results demonstrated that the additional phases, such as HA, GO, or AgNO<sub>3</sub>, affect the  $\beta$ -phase transformation in the composites, reaching the highest  $\beta$ -phase concentration at 56.76%. Electrical measurements showed that the maximum increase in electrical resistance occurred in the PVDF/HA/AgNO<sub>3</sub>/GO sample, reaching  $10.82 \times 10^{-6} \Omega\text{m}$ . The  $\beta$  phase is also required to integrate the PUF key, which would ensure the safe use of the functional element and protect patient data. The developed  $\beta$ -phase-transformed piezoelectric composite is suitable for the development of biomechanical sensors.

## 6. SANTRAUKA

### IVADAS

Aptikimo technologijoje naudojama informacija gali būti užpuoliko taikiny. Užpuolikas gali nustatyti, ar žmogus nešioja implantą, ir sužinoti implanto tipą. Užpuolikas gali ne tik užfiksuoti pranešimus, bet ir siųsti jiems komandas keisti informaciją ir ją išsiųsti. Todėl kuriamam funkciniam elementui pirmiausia reikia parinkti medžiagų gamybos technologiją, o tada nagrinėti saugumo užtikrinimo galimybes.

Polimerinių medžiagų arba kompozitų naudojimas tampa vis reikalingesnis dėl jų įperkamumo ir plataus prieinamumo. Polimerai paprastai turi didelį lauko stiprumą ir didelį dielektrinį stiprumą. Pjezoelektriniai polimerai idealiai tinka įvairioms įrenginių konfigūracijoms, taip pat techninėms ir inžinerinėms reikmėms. Pjezokeraminės medžiagos yra pagrindinių techninių komponentų pagrindas biomedicinos prietaisų, akustikos, mikroelektronikos ir kitų jutiklių srityse, todėl polimerų ir keramikų kompozicija yra labai paklausia.

Dėl puikaus stabilumo ir elektrinių savybių polivinilideno fluoridas (PVDF) yra viena naudingiausių fluoro polimerinių medžiagų pramonėje ir dėl puikių feroelektrinių savybių plačiai naudojamas elektrotechnikoje. Pjezoelektrinė PVDF savybė priskiriama  $\beta$  ir  $\gamma$  fazėms, kurios yra polinės kristalinės fazės.  $\beta$  fazė turi didžiausią elektrinį dipolio momentą iš visų kristalinių fazių, todėl PVDF  $\beta$  fazės kiekio padidėjimas yra veiksmingas būdas pagerinti PVDF pagrindu veikiančių jutiklių pjezoelektrines savybes. Gali būti naudojami keli apdirbimo metodai: tempimas, poliarizacija elektriniame lauke, terminis atkaitinimas ir užpildo įterpimas, siekiant padidinti dipolio stiprumą ir padidinti  $\beta$  fazės frakciją PVDF.

Padidinus PVDF  $\beta$  fazę, galima sustiprinti jo pjezoelektrinį atsaką. Akyta keramika, tokia kaip HA, gali būti naudojama kaip armatūra, siekiant pagerinti PVDF pjezoelektrines savybes. PVDF polimeras ir  $\alpha$ -PVDF/HA kompozitai pasižymi dielektrinėmis, mechaninėmis, šiluminėmis ir fizinėmis savybėmis.

Grafeno pagrindu pagamintos medžiagos gali būti plačiai taikomos biomedicinos inžinerijoje. Grafas turi labai didelį mechaninį stiprumą, paviršiaus plotą ir šilumos bei elektros laidumą. GO galima pridėti prie daugelio polimerinių matricių, siekiant pagerinti jų mechanines, šilumines ir elektrines charakteristikas. Biomedicinoje GO įtraukimas neturėtų sumažinti biologinio suderinamumo ir, pageidautina, turėtų slopinti bakterijų augimą ant paviršių ir sumažinti trombogeniškumą.

Sidabro nanodalelės ( $\text{Ag}^0$ ) išskiria sidabro jonus ( $\text{Ag}^+$ ), kurie sąveikauja su DNR fosforo dalimis. Dėl šių priežasčių laidžios fazės, tokios kaip sidabras, pridėjimas gali būti naudingas, nes, padidinus pjezoelektrinio atsako jautrumą, laidžioji fazė pagerina krūvio perdavimą.

Dielektrinės plėvelės plačiai naudojamos farmacijos, organinių tranzistorių, kondensatorių, jutiklių, mikroelektronikos ir galios elektronikos sektoriuose. Šioje jutiklių taikymo srityje yra daug kibernetinių atakų siekiant gauti ar valdyti asmeninę informaciją, todėl biojutikliai yra potenciali sritis, kurioje galima peržvelgti atakų

galimybes ir jų apsaugos būdus. Dėl plačiai paplitusio naudojimo ir saugos funkcijų trūkumo interneto įrenginiuose kibernetinis saugumas yra pagrindinis tikslas.

Kuriamas kompozitas yra potenciali medžiaga informacijai apsaugoti tikslinėje funkcinio elemento taikymo srityje. PUF – fizinė neklonuojama funkcija, dažnai randama kibernetinėse fizinėse sistemose. Naudojant šio tipo PUF, būtų galima pridėti saugos funkcijų neinvestuojant į brangią naują aparatinę įrangą, todėl kuriant funkcinį elementą bus pasitelkta šio funkcionalumo galimybės integruoti.

**Darbo tikslas** – sukurti pjezoelektrinę kompozitinę medžiagą, pagamintą beta fazės polivinilideno fluorida pagrindu, skirtą biomechaniniams jutikliams su duomenų apsaugos galimybėmis.

### **Uždaviniai**

1. Ištirti duomenų apsaugos metodus ir medžiagas, naudojamas nešiojamuosiuose ir implantuojamuose biomechaniniuose jutikliuose.
2. Susintetinti pjezoelektrinį kompozitą su beta fazės transformacija, į PVDF įtraukiant HA, GO ir AgNO<sub>3</sub> nanodaleles.
3. Įvertinti HA, AgNO<sub>3</sub> nanodalelių ir skirtingos jų sudėties įtaką pjezoelektrinio kompozito elektrinėms, mechaninėms ir morfologinėms savybėms.
4. Įvertinti GO įtaką PVDF pagrindu pagaminto kompozito pjezoelektrinėms, elektrinėms ir morfologinėms savybėms jutimo taikymui.

### **Metodai ir priemonės**

Plėvelėms paruošti buvo naudojamas tirpiklio liejimo metodas su DMSO tirpikliu. Vibracijos eksperimentams naudojamas vibracijos akselerometras KD35 (RFT GmbH, Schwabmünchen, Vokietija). Metalinės plokštės ir vibracijos amplitudei gauti buvo naudojamas lazerinis atstumo matuoklis (Keyence), o informacijai gauti buvo naudojamas PicoScope 3424 osciloskopas. Jis buvo prijungtas prie kompiuterio, o duomenys buvo analizuojami naudojant PicoScope 6.14.69. Paviršiaus šiurkštumui analizuoti buvo naudojama plataus ploto 3D matavimo sistema. Elektriniams matavimams buvo naudojama 4200-SCS puslaidininkių charakteristikų sistema. SEM matavimams mėginiai buvo paruošti e-Beam metodu. Mėginiai buvo įdėti į elektronų pluošto fizinę garų nusodinimo kamerą (Nanovak – NVEB 600), įdėti iki  $9 \times 10^{-6}$  Torr slėgio kamerą ir padengti auksu, kad būtų išgautas laidas paviršius SEM analizei. Aukso sluoksnis buvo išgautas naudojant 56 mA srovę, o sluoksnio storis buvo pastovus 5 nm. Skenuojamosios elektroninės mikroskopijos (SEM) vaizdai buvo gauti naudojant FEI QUANTA 250 modelį.  $d_{33}$  konstanta buvo išmatuota naudojant PolyK Quasi Satic Piezoelectric  $d_{33}$  Meter. Teoriniai vibracijos modeliai buvo modeliuojami naudojant COMSOL multifizikos programinę įrangą. Hidrofiliskumui matuoti buvo naudojamas kontaktinio kampo geometras, skirtas skysčio lašo ant kieto paviršiaus sąlyčio kampui nustatyti (Kauno technologijos universiteto Mechanikos inžinerijos ir dizaino fakultetas). EDX matuoti buvo naudojama Bruker 127 eV ir Esprit programinė įranga analizei. Įranga Perkin Elmer UATR Two FT-IR spektrometras naudojamas FTIR analizei.

### **Mokslinis naujumas**

1. PVDF pagrindu sukurti pjzoelektriniai kompozitai su HA, GO ir AgNO<sub>3</sub> dalelėmis yra biologiškai suderinami ir tinkami sudėtingos geometrijos biomechaniniams jutikliams formuoti.
2. Pjzoelektrinių savybių ir beta fazės transformacijos integracija kompozitinėje medžiagoje užtikrina duomenų saugumą ir gali būti taikoma kuriant daiktų internetą.

### **Praktinė darbo vertė**

1. Sukurta pjzoelektrinio kompozito PVDF pagrindu su HA, GO ir AgNO<sub>3</sub> nanodalelėmis sintetavimo metodika, užtikrinanti pjzoelektrinių savybių ir beta fazės transformacijos integraciją kompozitinėje medžiagoje.
2. Susintetinto pjzoelektrinio kompozito pagrindu sukurti funkciniai elementai gali būti naudojami fizikiniams impulsams matuoti, kartu užtikrinant įvesties ir išvesties informacijos saugumą.

### **Ginamieji teiginiai**

1. Susintetintas pjzoelektrinis kompozitas pasižymi pjzoelektrinėmis savybėmis mikrometriniu lygiu, o jo mechaninės, elektrinės, morfologinės ir hidrofobinės savybės yra valdomos keičiant pridedamas nanodaleles.
2. Sukurtas beta fazės transformacija pasižymintis pjzoelektrinis kompozitas yra tinkamas biomechaninių jutiklių kūrimui.

### **Darbo aprobavimas**

Disertacijos rezultatai paskelbti dviejuose straipsniuose recenzuojamuose mokslo leidiniuose Web of Science duomenų bazėje indeksuotuose leidiniuose su cituojamumo rodikliu tarptautinėse (užsienio) leidyklose, viename straipsnyje nacionalinės leidyklos žurnale ir rezultatai paskelbti viename Web of Science duomenų bazėje indeksuotame leidinyje be cituojamumo rodiklio. Rezultatai pristatyti penkiose tarptautinėse mokslinėse konferencijose (Mechanika 2021, Advanced materials and technologies 2022, Mechanika 2023, Engineering mechanics 2023, Mechanika 2024). Taip pat 2024 metais rezultatai pristatyti trijose tarptautinėse konferencijose (IEEE MEMSTECH'2024, Mechanika 2024 ir 2024 Innovations in Intelligent Systems and Applications Conference (ASYU)).

### **Disertacijos struktūra**

Disertaciją sudaro įvadas, literatūros apžvalga, keturi pagrindiniai skyriai, bendrosios baigiamosios darbo išvados, santrauka lietuvių kalba, literatūros sąrašas, gyvenimo aprašymas, padėka. Iš viso 132 puslapiai, 74 paveikslai, 16 lentelių ir 120 literatūros šaltiniai.



## 6.1. Duomenų apsauga biojutikliuose

Užpuolikai jau įrodė, kad jiems būtų labai patogu nusitaikyti į daiktų interneto įrenginius [1]. Dėl plačiai paplitusio naudojimo ir saugumo funkcijų trūkumo interneto įrenginiai yra pagrindinis užpuolikų tikslas [1].

Kuriamas kompozitas yra potenciali medžiaga informacijos apsaugai taikomųjų programų srityje. PUF – fizinė neklonuojama funkcija, dažnai randama kibernetinėse fizinėse sistemose. Naudojant PUF, būtų galima pridėti saugos funkcijų neinvestuojant į brangią naują aparatinę įrangą [2].

Kadangi užpuolikai gali paveikti jutimo technologiją, pirmiausia reikia išanalizuoti galimas grėsmes ir būdus, kaip apsaugoti informacijos srautą taikomoje srityje.

Biojutikliai naudoja konfidencialią informaciją, kuri labai svarbi siekiant apsisaugoti nuo galimų atakų, todėl toliau apžvelgsime, kokias grėsmes galima aptikti medicinoje naudojamuose jutikliuose ir jos įrenginiuose.

Saugumo pažeidėjus galima suskirstyti į dvi pagrindines kategorijas: aktyvius ir pasyvius. Pasyvi ataka gali klausytis tik kanale ir gauti prieigą prie pranešimų. Darant prielaidą, kad radijo kanalas yra nesaugus, pasyvus užpuolikas kelia tiesioginę grėsmę konfidencialumui. Pasyvus užpuolikas gali nustatyti, ar žmogus nešioja implantą, sužinoti, kokio tipo implantą ir kitą informaciją, tokią kaip jo modelis, serijos numeris ir kt. Tačiau aktyvus užpuolikas gali ne tik užfiksuoti pranešimus, bet ir siųsti jiems komandas keisti pranešimus. Jis taip pat gali bandyti pakeisti prietaiso konfigūraciją, išjungti gydymą ar net sukelti pacientui šoko būseną [5].

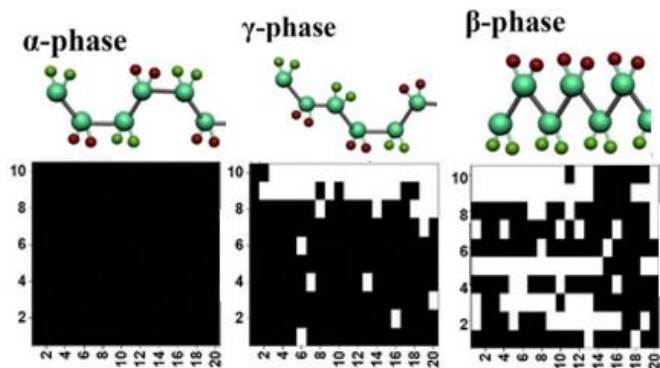
Keraminiai PZT ir polimeriniai PVDF keitikliai sukuria įtampą, proporcingą taikomam mechaniniam įtempiui, jėgai ar slėgiui. Pjezoelektriniai keitikliai, sumontuoti konsolinėje padėtyje, svyruoja veikiami mechaninės jėgos, sukurdami elektrinį išėjimo signalą, kuris svyruoja keitiklio rezonanso dažniu. Preliminari duomenų analizė parodė, kad rezonanso dažnio matavimai gali būti potencialūs PUF kandidatai [7].

PUF yra daug žadantys aparatinės įrangos saugumo įrenginiai. PUF gali generuoti neklonuojamus atsakymus, pagrįstus proceso pokyčiais, kurie neišvengiamai atsiranda gaminant lustą. Perspektyviausias variantas yra *Physical Unclonable Functions* (PUF) – aparatūros pagrindu sukurtų saugumo primitivų klasė, kuri sukuria atsitiktinius ir netikėtus kriptografinius raktus, pasinaudodama specialiomis fizinėmis elektroninių prietaisų savybėmis [4].

Kadangi PUF gali pasiūlyti saugų ir patikimą identifikavimą, autentifikavimą ir raktų generavimą įvairiose programose, įskaitant įrenginio autentifikavimą, saugų ryšį ir apsaugą nuo padirbinėjimo, jie yra labai paklausūs informacijos saugumo pramonėje. Pagrindinė PUF funkcija yra sukurti saugos raktą arba pasiūlyti atskirą identifikaciją, kuri gaunama specialiai fiziškai pakeitus elektroninį įrenginį. PUF yra ypač saugūs ir naudojami programose, kurioms reikia patikimų ir tvirtų saugos funkcijų, nes jų fizinės savybės dažnai sunku arba neįmanoma kopijuoti. Metalų oksidai pastaruoju metu sulaukė didelio susidomėjimo kuriant PUF, naudojant patikimas, nusistovėjusias puslaidininkines medžiagas dėl jų pranašumų, įskaitant didelio ploto sintezę, apdorojimą žemoje temperatūroje ir suderinamumą su standartiniais gamybos įrankiais.

PVDF ir jo dariniai buvo naudojami daugelyje prietaisų, tokių kaip fotodetektoriai, jutikliai, baterijos ir triboelektriniai nanogeneratoriai. Be to, PUF įrenginiai, kuriems reikia elektrinių savybių, gali būti suprojektuoti naudojant skirtingas PVDF fazių perėjimo charakteristikas.

Sukurtas  $\beta$  fazės PVDF-HFP elektrinis įtaisas parodė, kad atkaitinimo temperatūra PVDF-HFP patyrė fazių perėjimą, sudarydama  $\alpha$ -,  $\beta$ - ir  $\gamma$ -fazes. Skaitmeniškai segmentuotos reikšmės buvo panaudotos kuriant saugos raktą, panašų į QR kodą, kaip parodyta 6.1 pav. Ribotas PVDF-HFP sąsajos dipolio momentas, kuris rodo, kad ji pirmiausia yra 0 būsenoje. Priežastis, kodėl  $\alpha$  fazės PVDF-HFP dengtų įrenginių VON reikšmės yra mažos, žiūrint į saugos raktą 1.1 pav., nevienodas polinių dipolių išsidėstymas, palyginti su iš anksto nustatyta standartine verte, lėmė pastebėtą netolygiai pasiskirsčiusių 0 ir 1 būsenų maišymąsi  $\beta$  fazėje. Nors 0 būseną dominuoja visame masyve dėl didesnio mažo VON tankio įrenginių tankio, akivaizdu, kad 0 ir 1 būsenos taip pat yra sumaišytos  $\gamma$  fazėje, todėl seka yra labiau nuspėjama nei  $\beta$  fazėje. Kadangi veiksmingas PUF diegimas priklauso nuo nuspėjamumo, PUF įrenginio saugos charakteristikos buvo įvertintos naudojant pagrindinį našumo rodiklį, tokį kaip vienodumas.



**6.1 pav.** Sukurtas saugos raktas fazės perėjimu  $\alpha$  fazėje,  $\beta$  fazėje ir  $\gamma$  fazėje

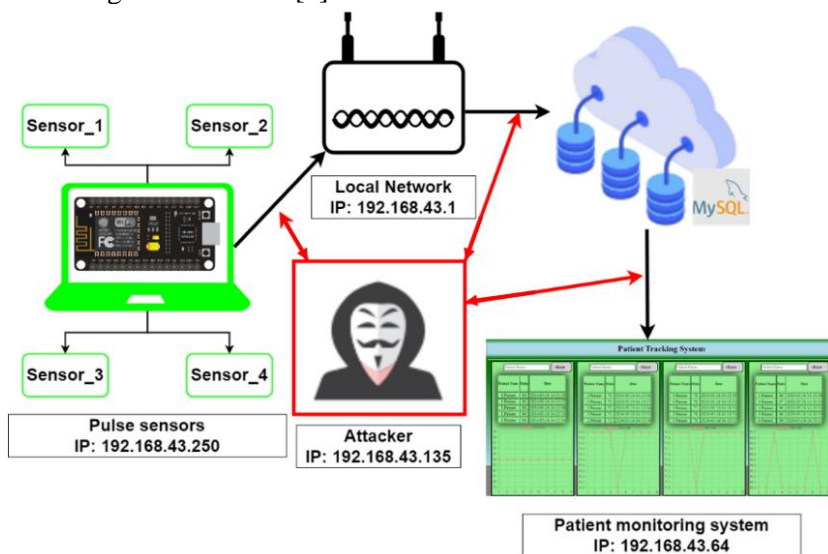
### 6.1.1. Nešiojamųjų ir implantuojamųjų biojutimų duomenų apsaugos įvertinimas

Biojutikliai naudoja konfidencialią informaciją, kuri yra labai svarbi siekiant apsaugoti nuo galimų atakų, todėl dabar apžvelgsime metodus, leidžiančius identifikuoti pulso informacijos srautą. Kadangi užpuolikai gali paveikti jutimo technologiją, pirmiausia reikia išanalizuoti galimas grėsmes ir rasti būdų, kaip apsaugoti informacijos srautą taikomųjų programų srityje. Peržiūrėsime informacijos nuskaitymo, paieškos metodus ir geriausią metodo pasirinkimą tikslinėje taikomųjų programų srityje.

Pacientų sekimo sistema yra svarbi technologija, naudojama sveikatos priežiūros sektoriuje. Tinklo topologija 6.2 pav. iliustruoja paciento sekimo sistemos organizavimą ir jutiklių integravimą. Jutikliai naudojami pacientų pulso reikšmėms matuoti ir perduoti šiuos duomenis tinklu. Tinklo topologija parodo, kaip jutikliai bendrauja su paciento sekimo sistema ir kaip perduodami duomenys. MITM (žmogus

viduryje) ataka gali aptikti informaciją trijuose taškuose, kurie paveikslėlyje pažymėti raudonai, taip pat, kaip galime pamatyti, užpuolikas gali ne tik aptikti, bet ir pakeisti informaciją ir išsiųsti ją atgal, pakeitęs norimą informaciją.

Jutimo metodas suteikia techninį pranašumą, palyginti su signalo stebėjimu, perduodant tikslią informaciją į nuskaitomą išvestį. Pasyvus užpuolikas tiesiogiai kelia grėsmę konfidencialumui ir gali kelti pavojų autentifikavimui, jei radijo kanalas yra nesaugus. Pasyvus užpuolikas gali sužinoti, ar kas nors turi implantą, koks jis yra, ir kitus parametrus, pvz., modelį ir serijos numerį. Jie taip pat gali gauti daugiau informacijos ir atskleisti asmens duomenis apie pacientą, įskaitant vardą, amžių, būklę, sveikatos įrašo ID ir kitą informaciją. Pagal šį scenarijų, aktyvus užpuolikas gali perduoti komandas, kad pakeistų pranešimus, prieš jiems pasiekiant įrenginį, ir perimti radijo kanalu siunčiamus pranešimus. Kadangi tai gali turėti įtakos ne tik asmeninei informacijai, bet ir gydymo ar taikymo spektrui, labai svarbu apsaugoti tokius duomenis nuo galimos rizikos [5].



**6.2 pav.** Tinklo topologija

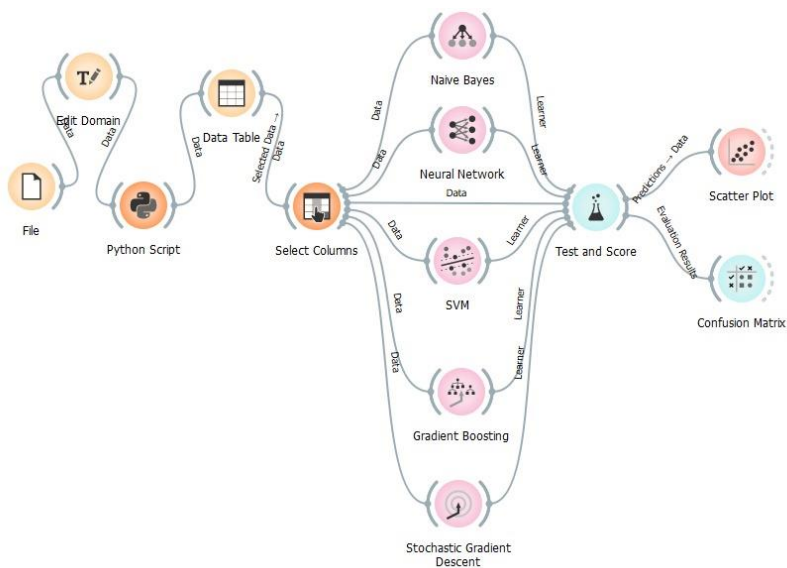
Pulsui matuoti prie paciento riešo tvirtinamas jutiklis, o jį pritvirtinus, pulso duomenys siunčiami į paciento sekimo sistemą.

Paleidus sistemą, jutiklio reikšmė TCP ryšio protokolu perduodama į kompiuterio aplinką, o perduota reikšmė įtraukiama į duomenų bazę. Naudojant MySQL duomenų bazę, įrašomas kiekvienos gaunamos reikšmės laikas, pulso dažnis ir paciento vardas. Šie duomenys rodomi lentelėje ir grafike, kuriuose rodomos pulso jutiklių, prie kurių pacientai yra prijungti, reikšmės. Sistema kartą per sekundę matuoja pulso dažnį, perduoda šiuos duomenis į sistemą ir užtikrina jų atvaizdavimą.

Šiandien sveikatos priežiūros sektoriuje naudojamos technologijos atlieka itin svarbų vaidmenį stebint ir valdant pacientų sveikatos būklę. Tačiau dėl didesnio šių technologijų naudojimo jie tapo labiau pažeidžiami kibernetinio saugumo grėsmių. Sveikatos duomenų saugumas yra itin svarbus pacientų privatumui, ypač tikslų gydymo procesų užtikrinimui. Šiame kontekste, norint užtikrinti sveikatos priežiūros

sistemų saugumą, būtina išnagrinėti kibernetinių atakų tipus ir apsaugos nuo šių atakų priemonės.

Tinklo srauto atakų aptikimas buvo atliktas naudojant dirbtinio intelekto algoritmus. Siekiant padidinti algoritmo tikslumą, tinklo srauto duomenys pirmiausia buvo iš anksto apdoroti į atitinkamą duomenų rinkinį ir padalyti į 10 milisekundžių dalis. Antra, 30 % duomenų rinkinio buvo naudojami patvirtinimui, o 70 % – mokymui. Kryžminis patvirtinimas buvo naudojamas analizuojant kelis algoritmus. Vėliau SGD buvo pasirinktas atakoms aptikti realiuoju laiku dėl geriausio tikslumo (6.3 pav.).



**6.3 pav.** Atakų aptikimas naudojant dirbtinio intelekto algoritmus

Dirbtinis neuroninis tinklas, pagrįstas SGD (Stochastic Gradient Descent), efektyviai analizuoja duomenis, todėl jis naudingas aptikus įsibrovimą. Duomenys treniruočių metu pateikiami į įvesties sluoksnį, o klaidų reikšmės apskaičiuojamos lyginant išvestį. SGD gali labai tiksliai aptikti įsibrovimus, mokydamasis sudėtingų modelių dideliuose duomenų rinkiniuose. SGD buvo geriausias įsibrovimų aptikimo realaus laiko duomenims metodas, pasižymintis didžiausiu tikslumu.

## 6.2. Pjezoelektriniai kompozitai

Kaip buvo aptarta ankstesniame skyriuje, jutikliams dažnai naudojamas pjezoelektrinis efektas, todėl žemiau apžvelgiamos populiariausios šių savybę turinčios medžiagos. Kadangi polimero / keramikos kompozitai yra plačiai naudojami ir aptariamais, toliau taip pat bus apžvelgti jau sukurti ir ištirti kompozitai.

Dėl puikių mechaninių savybių pjezoelektriniai polimerai, tokie kaip poli(L-laktidas) (PLLA), poli(vinilideno fluoridas) (PVDF), poli(vinilidenfluorido trifluoretilenas) (P(VDF-TrFE)), poliamidai (PI), poliakrilnitrilas (PAN) ir kt., sudaro daugumą organinių pjezoelektrinių medžiagų. Šios medžiagos dažnai naudojamos lanksčiuose jutikliuose. Labiausiai paplitusi organinė pjezoelektrinė medžiaga yra

PVDF, kuri yra lengviau pritaikoma nei pjezoelektrinė keramika. Todėl polimerai turi pranašumų, palyginti su pjezoelektrine keramika, nes juos galima integruoti į bet kokios reikiamos formos plonas plėveles [16, 26]. Siekiant pagerinti pjezoelektrinių polimerų jutiklių veikimą, pjezoelektriniai kompozitai buvo pagaminti naudojant įvairias įprastas neorganines pjezoelektrines medžiagas, įskaitant PZT ar ZnO. Pjezoelektriniai polimerai pasižymi geromis mechaninėmis savybėmis, tačiau maži jų pjezoelektriniai koeficientai riboja jų veikimą jutikiliuose [16, 26].

Pb [ZrxTi1-x] O<sub>3</sub> (PZT) yra dažniausiai naudojama pjezoelektrinė keramika. Tačiau bario titanatas buvo viena iš pirmųjų medžiagų, naudousių pjezoelektrą. Šios medžiagos laidumas yra išskirtinai didelis, nepaisant mažos pjezoelektrinės konstantos [16, 26]. Švino magnio niobato-švino titanatas (PMN-PT) ir ličio niobatas (LiNbO<sub>3</sub>) taip pat dažnai naudojami pjezoelektrinėse medžiagose. Biologiškai suderinama keramika, tokia kaip KNbO<sub>3</sub>, NaNbO<sub>3</sub> ir kt., gali būti naudojama įvairiuose jutikliuose [19].

Taip pat buvo analizuojami HA ir PVDF kompozitų pranašumai. PVDF pluoštų pagaminimas tirpalu lėmė didesnę pluošto gamybos greitį ir β fazės susidarymą nei elektrinis verpimas [21].

Taip pat kuriamo kompozito Ag/C dalelės buvo tolygiai paskirstytos PVDF matricioje, o tai turėjo įtakos Ag/C/PVDF kompozitų kristalizacijos procesui ir dielektrinėms savybėms. Kompozitų kristališkumas sumažėjo, nes padidėjo Ag/C dalelių kiekis. Didėjant Ag/C dalelių kiekiui, dėl pagerėjusios sąsajos poliarizacijos padidėjo ir Ag/PVDF kompozitų elektrinis laidumas. Taigi, kompozitai, kurių sudėtyje yra Ag, pagerina PVDF beta fazės buvimą bei elektrines savybes [22].

Buvo sukurtas Ag-NBCTO-PVDF kompozitas, ir rezultatai parodė, kad Ag nanodalelės buvo labai svarbios didinant medžiagos dielektrinį laidumą [115].

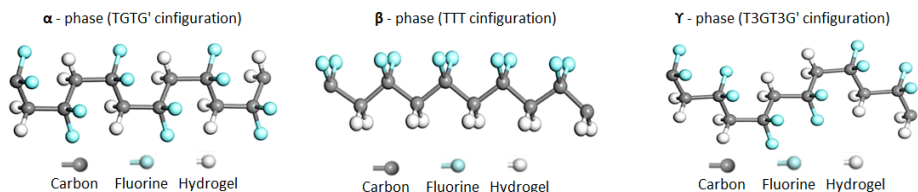
Didelė β fazė (β = 95%) buvo sėkmingai sukurta PVDF naudojant H<sub>2</sub>SO<sub>3</sub>. Todėl PVDFBDS plėvelės pasižymėjo puikiais feroelektrinėmis ir pjezoelektrinėmis savybėmis [82].

PVDF/Ag/BaTiO<sub>3</sub>, pagamintas tirpalo liejimo būdu, palyginti su įprastais PVDF/BaTiO<sub>3</sub> kompozitais, pasižymi geresnėmis dielektrinėmis savybėmis. PVDF/Ag/BaTiO<sub>3</sub> kompozitų dielektrinė konstanta smarkiai padidėjo didėjant Ag kiekiui [75].

### **6.2.1. PVDF β fazės poveikis pjezoelektriniams jutikliams**

Palyginti su pjezoelektrine keramika, PVDF yra plačiausiai naudojama organinė pjezoelektrinė medžiaga, nes ji yra universalesnė. PVDF plėvelės turi 98,8 % β fazės gaminant idealioje 60 °C temperatūroje, naudojant tirpiklį dimetilsulfoksidą (DMSO). PVDF plėvelė pasižymi išskirtinėmis feroelektrinėmis ir pjezoelektrinėmis savybėmis dėl stiprios β-fazės sudėties. Galiausiai, PVDF plėvelėms kurti galima naudoti liejimo būdą tirpikliu. PVDF plėvelės gali būti gaminamos esant įvairioms kristalizacijos temperatūroms (50–160 °C), naudojant idealų DMSO (dimetilsulfoksido) tirpiklį, siekiant nustatyti, kaip temperatūra veikia β fazės kiekį [77]. Reguliuojant tirpalo temperatūrą DMSO (dimetilsulfoksido) tirpikliu, galima sukurti keletą PVDF fazių. Viena fazė gali virsti kita PVDF faze dėl atkaitinimo sąlygų. β fazė aptinkama naudojant polinį tirpiklį ir tinkamą atkaitinimą, kuris yra būtinas feroelektrinėms

reikmėms. Po penkių valandų atkaitinimo 90 °C temperatūroje PVDF plėvelės pasiekia maksimalią  $\beta$  fazę [78, 37]. Medžiaga PVDF yra perspektyvus pasirinkimas nešiojamiesiems, lankstiesiems ir implantuojamiems elektroniniams jutikliams, nanogeneratoriams, energijos surinkėjams, dirbtinei odai ir biomedicinos reikmėms dėl mechaninio ir cheminio stabilumo, lankstumo, netoksiškumo, terminio stabilumo ir biologinio suderinamumo. Kaip matyti 6.4 pav., tik dvi iš trijų polimorfinių kristalinių PVDF modifikacijų ( $\alpha$ ,  $\beta$  ir  $\gamma$ ) sudaro polines fazes. Labiausiai pageidaujama PVDF polimero fazė yra  $\beta$  fazė dėl didžiausio elektrinio dipolio momento. Paprastai PVDF  $\beta$ -fazės sustiprinimas pasiekiamas termiškai apdorojant, mechaniniu tempimu, elektropoliravimu ir užpildo pridėjimu [37, 79, 80].



**6.4 pav.** PVDF molekulinė struktūra, vizualinis  $\alpha$ ,  $\beta$  ir  $\gamma$  fazių vaizdas

Kai PVDF yra veikiamas išorinės mechaninės jėgos, jis gali pagaminti daug energijos. PVDF medžiaga yra praktiškesnė nei keramika dėl nepaprasto lankstumo ir ilgaamžiškumo. Nepaisant daugelio privalumų, pagrindinė kliūtis PVDF polimerų naudojimui yra iššūkis pasiekti  $\beta$  fazę [88][79].

### 6.2.2. HA-hidroksiapatito medžiaga

Kadangi keramika turi geras pjezoelektrines savybes, kaip aptarėme ankstesniuose skyriuose, HA (hidroksiapatitas) yra viena iš potencialių medžiagų. Hidroksiapatitas (HAp) yra puiki medžiaga biomedicinoje dėl savo savybių, tokių kaip biologinis suderinamumas ir pjezoelektra. Šis biokeraminis junginys, kalcio fosfato forma, natūraliai randamas žmogaus audiniuose ir yra pagrindinis dantų ir kaulų neorganinis mineralinis komponentas. Sintetiniai metodai plačiai naudojami HAp gamybai, nes sintetinis HAp turi gerą pjezoelektrinį efektą, todėl tinkamas elektromechaniniams signalams aptikti. HAp plonų plėvelių sintezė yra efektyvus būdas gaminti jutiklius technologinėms reikmėms [35].

Pjezoelektriniai kompozitai buvo sukurti naudojant daugybę populiarių neorganinių pjezoelektrinių medžiagų, tokių kaip HA, siekiant pagerinti pjezoelektrinių polimerų jutiklių veikimą. Mažas kristališkumas ir didelis poringumas buvo pagaminto hidroksiapatito (HA) savybės. HA, pagamintas iš gyvūnų kaulų ir kalcinuotas 800 °C temperatūroje, pasižymi didžiausiu kristališkumu. Hidroksiapatitas (HA) gali sukurti cheminį ryšį su aplinkiniais mineralais, kai susidaro HA sąsajos sluoksnis [4, 37].

Kita vertus, hidroksiapatitas (HA) yra kalcio fosfatas, kurio cheminė formulė  $\text{Ca}_{10}(\text{PO}_4)_6(\text{OH})_2$ , kuris yra ištirtas biokeramikos srityje ir yra vienas dažniausiai naudojamų biomedicinoje ir klinikinėje veikloje, nes labai primena kristalinę kaulinio audinio fazę. Hidroksiapatitas yra osteokondukcija, biologiškai suderinama, bioaktyvi ir termodinamiškai stabili medžiaga, kuri kartu su biologiškai suderinamais

polimerais (PVDF, polipieno rūgštimi (PLA), polikaprolaktonu (PCL) ir kt.) tampa medžiaga, turinčia didelį kompozito kūrimo potencialą [3].

Atsižvelgiant į tai, kad HA turi gerą hidrofilumą ir gali sudaryti kaulų ryšius su kauliniu audiniu, galima paruošti HA/polimero kompozitus. HA įterpimas į PVDF pjezoelektrinę dangą gali pagerinti dangos hidrofilumą ir suteikti pjezoelektrines savybes ir gerą biologinį suderinamumą [38].

### 6.2.3. GO – grafeno oksido medžiaga

Grafenas turi labai didelį mechaninį stiprumą, paviršiaus plotą ir šilumos bei elektros laidumą, todėl tai potenciali medžiaga kuriamam kompozitui. Grafeno oksidas (GO) pasižymi išskirtinėmis mechaninėmis, elektrinėmis, optinėmis, šiluminėmis ir biologiskai suderinamomis savybėmis. GO pasižymi antibakterinėmis savybėmis dėl elektrostatinės adsorbcijos ir fizinės izoliacijos. Jo antibakterinės savybės buvo plačiai ištirtos, o duomenys rodo, kad GO antibakterinės savybės yra nestabilios ir priklauso nuo daugelio kintamųjų, įskaitant struktūrą, aplinką, temperatūrą ir magnetinį lauką. Norint įveikti šiuos veiksnius, GO pagrindu pagaminti antibakteriniai kompozitai gali būti sukurti derinant GO su polimerais [119].

Pjezoelektriniai kompozitai, sudaryti iš poli (3-hidroksibutirato-ko-3-hidroksivalerato) (PB) ir grafeno oksido (GO), buvo sėkmingai pagaminti naudojant elektros verpimo technologiją. Buvo ištirtos pagamintų kompozitų morfologinės, fizinės, cheminės, pjezoelektrinės ir biologinės savybės. GO pridėjimas padidina pjezoelektrinį koeficientą ( $d_{33}$ ) [39].

Taip pat buvo ištirtas GO/rGO (rGO – redukuotas grafeno oksidas) poveikis PVDF-(BZT-BCT) kompozitinės plėvelės elektrinėms savybėms. GO ir rGO kompozicinės plėvelės pasižymi geresnėmis dielektrinėmis, feroelektrinėmis ir pjezoelektrinėmis savybėmis. Kompozitinės plėvelės su optimizuota GO koncentracija (0,16 masės%) laidumas 2 kartus didesnis už gryno PVDF. Rezultatai rodo, kad poliarizacija pagerinama šešis kartus, o pjezoelektrinės savybės – tris kartus, todėl kompozicija idealiai tinka pjezoelektrinės dirbtiniams širdies stimulatoriams ir mažos galios elektronikai [40].

### 6.2.4. AgNO<sub>3</sub> – sidabro nitrato medžiaga

Laidi fazė, tokia kaip sidabras, gali būti naudinga, nes, padidinus pjezoelektrinio atsako jautrumą, laidžioji fazė pagerina krūvio perdavimą, o tai yra labai svarbus aspektas projektuojant pjezoelektrinius kompozitus. Sidabro nanodalelės (AgNP) gali būti naudojamos kaip PVDF užpildas β fazės kiekiui padidinti ir kaip antibakterinė priemonė pramonėje ar chirurgijoje. Nustatyta, kad kai AgNP kiekis buvo nuo 0,4 % iki 0,6 %, PVDF β kiekis padidėjo beveik 8 % [%] [41].

Sidabro nanodalelės yra labai baktericidinės, gana nekenksmingos žmonėms ir netoksiškos. Laidžios fazės, tokios kaip sidabras, pridėjimas gali būti naudingas, nes; pirma, laidžioji fazė pagerina krūvio perdavimą padidindama pjezoelektrinio atsako jautrumą, o atitinkamas Ag nusėdimo kiekis suteikia pjezoelektrinį aktyvumą [20, 17]. Pažymėtina, kad sustiprintas lokalizuotas Ag nanodalelių (Ag NP) elektromagnetinis laukas gali būti racionaliai sukeltas paspaudžiant arba lenkiant PVDF plėvelę, kad būtų galima nustatyti itin didelį jautrumą [42].



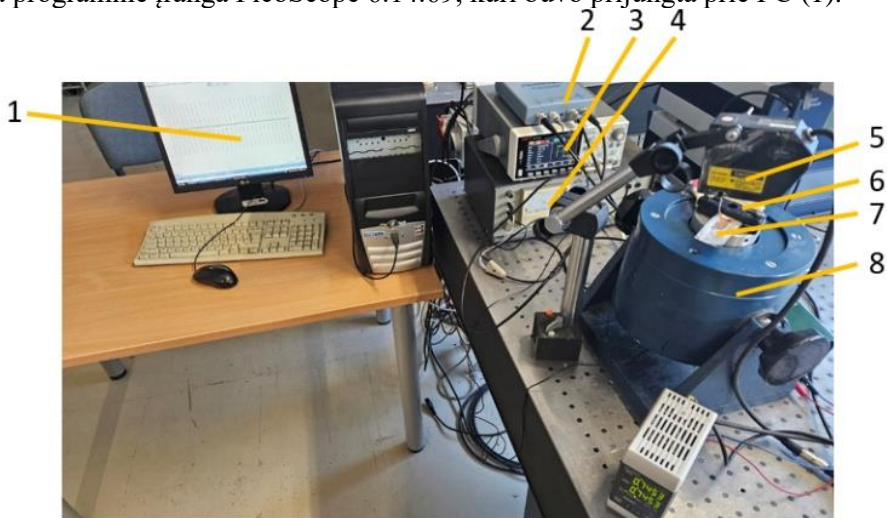
### 6.3. Medžiagos ir eksperimentinė metodika

Norint nustatyti kompozicines medžiagas kaip tinkamas naudoti jutikliuose, reikalingi matavimo ir taikymo metodai. Pagrindinės elektrinės charakteristikos, pvz., pjezoelektrinės konstantos, ir kitos charakteristikos yra būtinos norint nustatyti funkcinę medžiagą kaip jutiklio sluoksnį. Todėl toliau apžvelgsime tyrimo metodiką, naudojamą kuriant kompozitus.

#### 6.3.1. Dinaminis tyrimas

Vibracijos matavimams buvo paruošos penkios metalinės plokštelės, padengtos įvairiomis PVDF medžiagomis. Pridėti ploni vario sluoksniai ant viršaus ir sulituoti du laidai su kontaktais abiejose pusėse – ant varinės plokštės ir metalinės plokštės. Naudojant multimetrą izoliacijai patikrinti, trumpųjų jungimų nerasta.

6.5 pav. parodyta eksperimentinė konfigūracija. Bandinys (7) tvirtinamas prie vibratoriaus (8), ir buvo naudojami spautukai (6). Vibratoriui buvo sukurtas sinusinis signalas, naudojant signalų generatorių (3), ir signalo stiprintuvą (4). Vibracijos parametrai nustatyti naudojant vibracijos akselerometrą KD35. Metalinės plokštės vibracijos amplitudė buvo išmatuota naudojant Keyence 5 lazerinį atstumo matuoklį. Duomenys rinkti naudojant PicoScope 3424 osciloskopą 2. Duomenims analizuoti naudota programinė įranga PicoScope 6.14.69, kuri buvo prijungta prie PC (1).



**6.5 pav.** Eksperimento paruošimas matavimams, parodant pagrindines naudojamos techninės įrangos dalis: 1 – kompiuteris, 2 – PicoScope 3424 osciloskopas (Pico Technology, Kembridžšyras, JK), 3 – signalų generatorius UNI-T UTG1022X (Uni-Trend Technology Ltd., Kinija), 4 – signalo stiprintuvas VEB Metro LV103, 5 – LK-G82 lazerio nuotolis metras (Keyence, Elmwood Park, Naujasis Džersis, JAV), 6 – spautukai, 7 – plieninė plokštė, padengta PVDF medžiagomis, ir vario laidžioji fazė, 8 – vibratorius



### 6.3.2. Pjezoelektrinio koeficiento $d_{33}$ matavimas

Pjezoelektrinis efektas yra sąveika tarp mechaninio ir elektrinio medžiagos elgesio, šią sąveiką galima apibūdinti išraiškomis [80]:

$$S = S^E T + dE; \quad (17)$$

$$D = \varepsilon^T E + dT; \quad (18)$$

čia  $E$  – elektrinio lauko stipris,  $D$  – dielektrinis poslinkis,  $T$  – taikomas įtempis,  $S$  – deformacija,  $s$  – atitiktis,  $\varepsilon$  – laidumas.

Konstanta  $d$  yra susijusi su trimis svarbiomis medžiagos savybėmis pagal šią lygtį [80]:

$$d = k\sqrt{\varepsilon_0 k^T s^E} \quad (C \text{ N}^{-1}); \quad (19)$$

čia  $k$  yra elektromechaninis sujungimo koeficientas,  $k^T$  yra dielektrinė konstanta esant pastoviam įtempimui, o  $s^E$  yra tamprus atitikimas pastoviam elektriniame lauke. Toliau pateikiamos dvi pagrindinės konstantos [80]:

$$d_{31} = k_{31}\sqrt{\varepsilon_0 k_3^T s_{11}^E} \quad (C \text{ N}^{-1}); \quad (20)$$

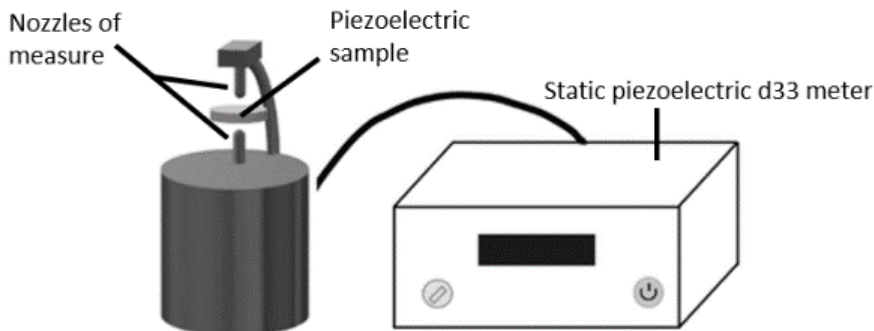
$$d_{33} = k_{33}\sqrt{\varepsilon_0 k_3^T s_{11}^E} \quad (C \text{ N}^{-1}). \quad (21)$$

$D$  konstantos yra susijusios su dideliais mechaniniais poslinkiais, esančiais judesio keitiklių įrangoje. Ir, atvirkščiai, koeficientas gali būti laikomas susietu su apkrova, sumontuota ant elektrodų veikiant mechaniniam įtempimui,  $d_{33}$  taikomas, kai jėga veikia trimis kryptimis – lygiagrečiai poliarizacijos ašiai – ir veikia tą patį paviršių, nuo kurio imama apkrova,  $d_{31}$  taikomas, kai apkrova surenkama nuo to paties paviršiaus, kaip ir  $d_{33}$ , tačiau jėga veikia statmenai poliarizacijos ašiai. Yra žinoma, kad jie turi tokį empirinį ryšį [80]:

$$d_{33} \approx -2,5 \times d_{31}. \quad (22)$$

Pjezoelektrinio krūvio koeficientas, jungiantis elektros krūvį, susidarantį bandinio plote su mechanine jėga, taikomas ir apskaičiuojamas kulonais – Niutono vienetais ( $C \text{ N}^{-1}$ ).

$d_{33}$  konstanta buvo išmatuota naudojant PolyK Quasi Satic Piezoelectric  $d_{33}$  Meter (6.6 pav.).

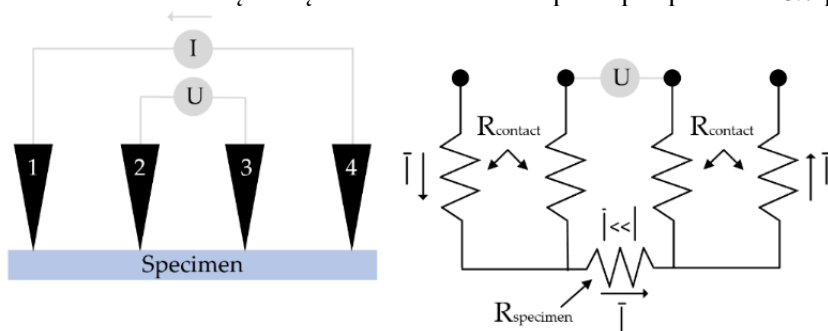


**6.6 pav.** Pjezoelektrinės konstantos  $d_{33}$  matavimo schema, naudojant PolyK statinį pjezoelektrinį  $d_{33}$  matuoklį

### 6.3.3. 4 zondų matavimas

Medžiagų ir puslaidininkių moksle keturių taškų zondo apibūdinimas yra tipiškas kietųjų medžiagų ir plonų plėvelių elektrinių charakteristikų tyrimo metodas. Didelės varžos voltmetras naudojamas įtampos kritimui per vidinę zondo grandinę aptikti po to, kai srovė praeina per jo išorinę grandinę. Dėl to išmatuotas įtampos kritimas ( $V$ ) daugiausia atsiranda puslaidininkio paviršiuje dėl srovės ( $I$ ), tekančios per mėginį. Matuojant puslaidininkinius kristalus arba plonas plėveles, srovė iš esmės tekės trimis kanalais [25].

Van der Pauw režimas, kvadratinis režimas, kolinearinis režimas, dvigubo zondo konfigūracijos režimas ir kiti režimai yra tarp daugybės sukurtų tradicinio keturių taškų zondo matavimo režimų [25, 57, 58]. Plačiai naudojamas kolinearinis režimas, o kolinearinio keturių taškų zondavimo metodo principas pateiktas 6.7 pav.



**6.7 pav.** Keturių taškų zondo metodo principas:  $I$  yra srovė, taikoma tarp išorinių zondų,  $U$  yra įtampos pokytis tarp zondų 2 ir 3,  $R$  yra lakšto varža

Įtampos kritimui ( $V$ ) vidinėje zondo grandinėje matuoti gali būti naudojamas voltmetras su didele varža, o srovė ( $I$ ) teka per išorinę zondo grandinę. Vadinasi, per bandinį tekanti srovė sukelia išmatuotą įtampos kritimą puslaidininkio paviršiuje. Tada 4 taškų zondo varža ( $R$ ) yra [25]:

$$R = \frac{V}{I}; \quad (23)$$

$$R_{2D}^{4pp} = \frac{1}{\pi\sigma_s} \ln\left(\frac{2s-r}{s+r}\right); \quad (24)$$

$$R_{3D}^{4pp} = \frac{1}{\pi\sigma_b} \ln\left(\frac{1}{s+r} - \frac{1}{2s-r}\right); \quad (25)$$

čia  $s$  – atstumas tarp gretimų taškų kontaktų,  $r$  – spindulys tarp gretimų taško kontaktų,  $\sigma_s/\sigma_b$  – vienodas matuojamo bandinio lakštinis laidumas.

Skaičiuojant galima naudoti šias formules [25]:

$$R_{2D}^{4pp} = \frac{U}{I} = \frac{\ln 2}{\pi\sigma_s}; \quad (26)$$

$$R_{3D}^{4pp} = \frac{U}{I} = \frac{1}{2\pi\sigma_b}. \quad (27)$$

Šiame tyrime 4200-SCS puslaidininkių charakteristikų sistema naudojama keturių taškų zondui matuoti. Įranga pateikta 6.8 pav.



**6.8 pav.** Keturių taškų zondo metodo matavimo įranga: a) mėginio matavimas; b) 4200-SCS modelio puslaidininkių charakteristikų sistema

Matavimo proceso metu keturi vienodais atstumais išdėstyti zondai liečiasi su medžiaga. Tūrio varžą galima apskaičiuoti pagal formulę [25]:

$$\rho = \frac{\pi}{\ln 2} \cdot \frac{V}{I} \cdot t \cdot k; \quad (28)$$

čia  $\rho$  – tūrinė savitoji varža,  $\Omega \cdot \text{cm}$ ,  $V$  – išmatuota įtampa,  $V$ ,  $I$  – šaltinio srovė,  $A$ ,  $t$  – bandinio storis,  $\text{cm}$ ,  $k$  – koeficientas, pagrįstas zondo ir plokštelės skersmens santykiu bei storio ir zondo santykiu.

#### 6.4. Pjezoelektrinių PVDF kompozitinių medžiagų sintezė ir analizė

Šiame skyriuje aptarsime funkcinio elemento gamybos procesą. Funkciniam elementui parinktos tinkamos medžiagos yra PVDF, HA ir  $\text{AgNO}_3$ , o gamybai pasirinktas tirpiklio liejimo būdas. Bus naudojamas netoksiškas tirpiklis DMSO. Šis gamybos būdas ir medžiagos buvo pasirinkti siekiant padidinti beta fazę, kuri yra labai svarbi kibernetiniam saugumui ir pjezoelektrinėms savybėms. Aptarsime kompozitų su PVDF, HA ir  $\text{AgNO}_3$  rezultatus.

#### 6.4.1. Kompozitų PVDF/HA/AgNO<sub>3</sub> paruošimas

Skystoje fazėje esančios cheminės medžiagos gali lengviau prasiskverbti į poras, kad būtų geresnė paviršiaus apdaila. Plonasluoksniuose dielektrikuose su lygesniais paviršiais nešiklio transportavimo varža yra mažesnė [64, 83]. Dėl šios priežasties mėginys ruošiamas liejimo tirpikliu būdu.

Dimetilsulfoksidas (DMSO) naudojamas kaip tirpiklis idealioje 90 °C temperatūroje plėvelėms gaminti. Norint sukurti homogeninį tirpalą, PVDF ir DMSO tirpiklis pirmiausia buvo sumaišyti ir penkias valandas kaitinami, tirpinami 90 °C temperatūroje. Kambario temperatūroje sidabro nitratas ir hidroksiapatitas buvo ištirpinti DMSO tirpiklyje ir maišomi 1–2 minutes, kad būtų užtikrinta vienoda dispersija. Sumaišius visus komponentus ir išliejus ant pagrindo, formavimo strypais suformuojama plėvelė ir tris valandas džiovinama 65 °C temperatūroje. Visas paruošimo procesas pavaizduotas 6.9 pav. Be to, 6.1 lentelėje yra nurodytos bandinių medžiagų koncentracijos kiekvienam bandiniui.



**6.9 pav.** Kompozitinių kietųjų plėvelių su PVDF/HA/AgNO<sub>3</sub> sintezės schema

**6.1 lentelė.** Mėginių su PVDF/HA/AgNO<sub>3</sub> koncentracijos ir receptūros

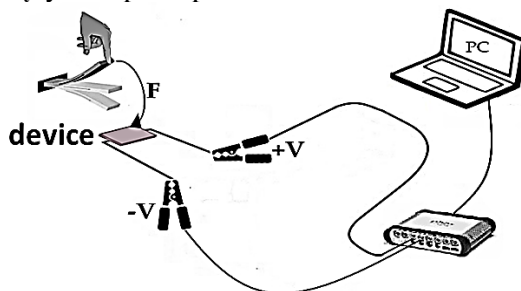
Sample No.	PVDF (g/ml)	HA (g/ml)	AgNO <sub>3</sub> (g/ml)
(1)	0,5g/2ml	0,05g/1ml	-
(2)	0,5g/2ml	0,10g/1ml	-
(3)	0,5g/2ml	-	0,2g/1ml
(4)	0,5g/2ml	0,05g/1ml	0,2g/1ml
(5)	0,5g/2ml	-	-

Buvo pagaminti penki mėginiai – 0,05 g HA:0,5 g PVDF (1), 0,1 g HA:0,5 g PVDF (2), 0,2 g AgNO<sub>3</sub>:0,5 g PVDF (3), 0,5 g HA:0,5 g PVDF: 0,2 g AgNO<sub>3</sub> (4) ir 0,5 g PVDF (5).

#### 6.4.2. Elektros potencialo tyrimas

Elektrinėms savybėms ištirti buvo sukonstruoti penki bandiniai (1, 2, 3, 4 ir 5 pavyzdžiai). Bandiniai buvo sudaryti iš trijų sluoksnių: plieno, funkcinio sluoksnio (kuriami kompozitai) ir aliuminio. Be to, buvo atliktas panašus tyrimas ir išmatuota

įtampa atviroje grandinėje [98]. 6.10 pav. pavaizduotas schematinis prietaisų elektrinių charakteristikų tyrimo principas.



**6.10 pav.** Mėginių elektrinių savybių matavimo schema

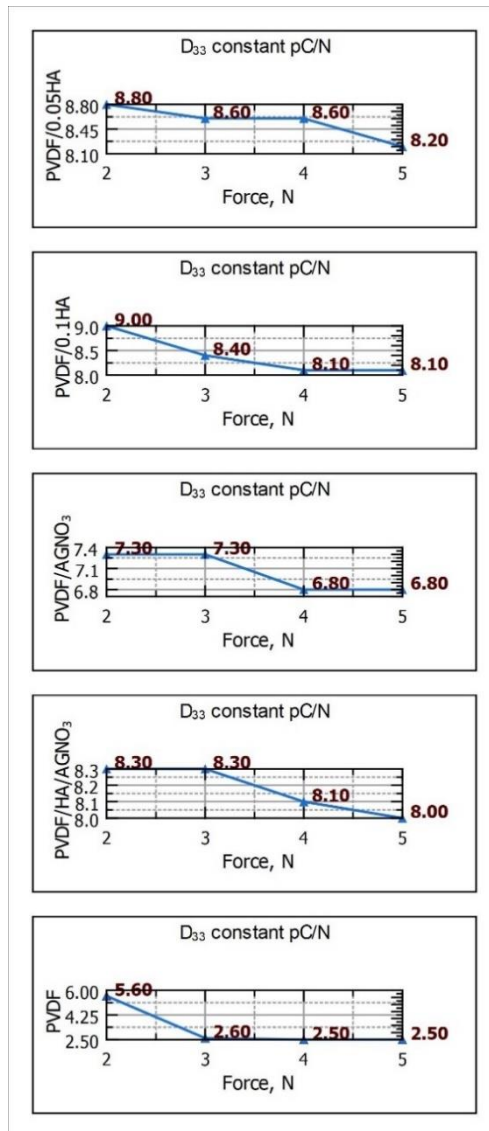
6.2 lentelėje pateikiamos vertės, elektros tyrimo rezultatai. Aktyvus sluoksnis HA, kurio nėra 3 ir 5 pavyzdžiuose, yra vertės sumažėjimo priežastis. Rezultatai 2-ame mėginyje ir parodė aukščiausią energijos lygį. Kadangi pagaminti kompozitai 3 ir 5 (be hidroksiapatito-HA) turėjo mažiausias energetines vertes, akivaizdu, kad HA tinkama medžiaga, siekiant padidinti elektrines savybes. Svarbu paminėti, kad PVDF feroelektrinių charakteristikų vystymas taip pat gali padidinti elektros krūvio perdavimą [118].

**6.2 lentelė** Kiekvieno mėginio išskirtos energijos vertės rezultatai

Sample					
Energy	1	2	3	4	5
(W/A)	$0,08 \pm 0,01$	$0,12 \pm 0,01$	$0,06 \pm 0,01$	$0,09 \pm 0,01$	$0,05 \pm 0,01$

#### 6.4.3. Pjezoelektrinio koeficiento $d_{33}$ matavimo rezultatai

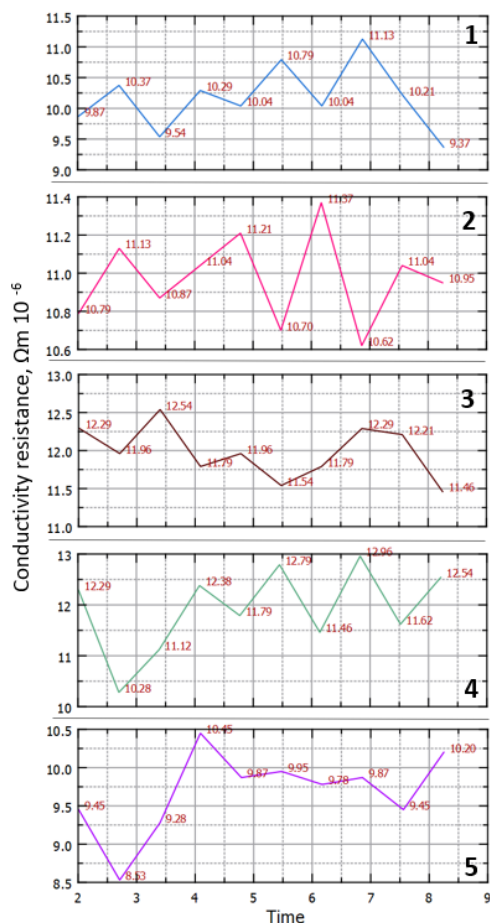
Kaip parodyta 6.11 pav., kiekvienas mėginys buvo matuojamas 4 kartus, didinant apkrovos jėgą [2–5 N] diapazone. PVDF (5 bandinys) vertė buvo mažiausia, ji buvo 5,6 pC / N su 2 N jėgos apkrova ir palaipsniui mažėjo – didinant apkrovą. Didžiausius rezultatus, 8,8–9 pC/N, pasiekė PVDF/HA mėginiai– esant 2 N jėgai, ir palaipsniui mažėjo – didinant apkrovą. Geri rezultatai taip pat gauti mėginio PVDF/HA/AGNO<sub>3</sub>, kurio  $d_{33}$  konstanta yra 8,3 pC/N esant 2 N jėgai. 2-jų N jėgos apkrova užtikrina geriausią našumą. 6.11 pav. parodo mėginių  $d_{33}$  reikšmes.



**6.11 pav.**  $d_{33}$  konstantos mėginių matavimo rezultatai

#### 6.4.4. Elektrinių savybių matavimas (4 zondų)

Šiame skyriuje aptariama PVDF, HA ir AgNO<sub>3</sub> įtaka kompozitinių plėvelių elektrinei varžai. 6.12 pav. rodomi keturių taškų zondo impulsų elektriniai matavimo rezultatai.



**6.12 pav.** Keturių taškų zondo impulsų elektrinio matavimo rezultatai, 1 pavyzdys – PVDF/0,05HA, 2 pavyzdys – PVDF/0,1HA, 3 pavyzdys – PVDF/AgNO<sub>3</sub>, 4 pavyzdys – PVDF/HA/AgNO<sub>3</sub>, 5 pavyzdys – PVDF

Kompozito, kurio sudėtyje yra PVDF/0,01HA (1 pavyzdys), keturių taškų zondo impulsų matavimas parodė, kad šio kompozito vidutinė elektrinė varža yra  $10,16 \times 10^{-6} \Omega m$ , o didžiausė reikšmė –  $11,13 \times 10^{-6} \Omega m$ . HA įtraukimas į kompozitą padidina elektrinę varžą. Didesnis pokytis buvo pastebėtas pridėjus AgNO<sub>3</sub> priedo, o didžiausia smailė užfiksuota ties  $12,54 \times 10^{-6} \Omega m$ .

Pridėjus visas medžiagas, didžiausias elektrinės varžos padidėjimas buvo  $12,96 \times 10^{-6} \Omega m$ . Šie rezultatai rodo, kad AgNO<sub>3</sub> ir HA gali turėti įtakos kompozito elektrinėms savybėms. Be to, dėl AgNO<sub>3</sub> gali susidaryti joninės jungtys, kurios gali prisidėti prie bendro laidumo. 5 mėginio rezultatai taip pat rodo, kad, kai nėra papildomų komponentų, matoma įtaka elektrinės varžos kritimui. Svarbu pažymėti, kad laidumo varžai įtaką gali daryti ir kiti veiksniai, pvz., priedų sklaida kompozite ir naudojamos apdorojimo sąlygos. Tačiau reikalingi tolesni tyrimai, siekiant išsiaiškinti tikslus mechanizmus, atsakingus už pastebėtus elektrinių savybių pokyčius.

## 6.5. PVDF pagrindu pagamintų medžiagų su HA, GO ir AgNO<sub>3</sub> užpildais kūrimas

Šiame skyriuje aptarsime funkcinio elemento gamybos procesą. Funkciniam elementui parinktos tinkamos medžiagos yra PVDF, HA, GO ir AgNO<sub>3</sub>, o gamybai pasirinktas tirpiklio liejimo būdas. Bus naudojamas netoksiškas tirpiklis DMSO. Šis gamybos būdas ir medžiagos buvo pasirinkti siekiant padidinti beta fazę, kuri yra labai svarbi kibernetiniam saugumui ir pjezoelektrinėms savybėms. Aptarsime kompozitų su PVDF, HA, GO ir AgNO<sub>3</sub> rezultatus.

### 6.5.1. Kompozitų PVDF/HA/GO/AgNO<sub>3</sub> paruošimas

Plėvelės buvo paruoštos naudojant dimetilsulfoksidą (DMSO) kaip netoksišką tirpiklį 90 °C temperatūroje. PVDF ir DMSO tirpiklis buvo sumaišomi ir atkaitinami 90 °C temperatūroje maždaug 5 valandas, kol susidarys vienalytis tirpalas. Sidabro nitratas, grafeno oksidas ir hidroksiapatito komponentai buvo disperguoti DMSO tirpiklyje kambario temperatūroje ir maišomi 1–2 minutes, kol tolygiai pasiskirsto arba ištirpsta. Galiausiai visi komponentai buvo sumaišyti ir supilti ant elektrodo pagrindo, plėvelė suformuota naudojant formavimo strypus ir džiovinama 65 °C temperatūroje apie 3 valandas. Mėginio paruošimo schema parodyta 6.13 pav.



**6.13 pav.** Mėginių PVDF/HA/GO/AgNO<sub>3</sub> paruošimo schema

Mėginių receptai ir koncentracijos pateikti 6.3 lentelėje. Buvo paruošti 4 skirtingi kompozitai.

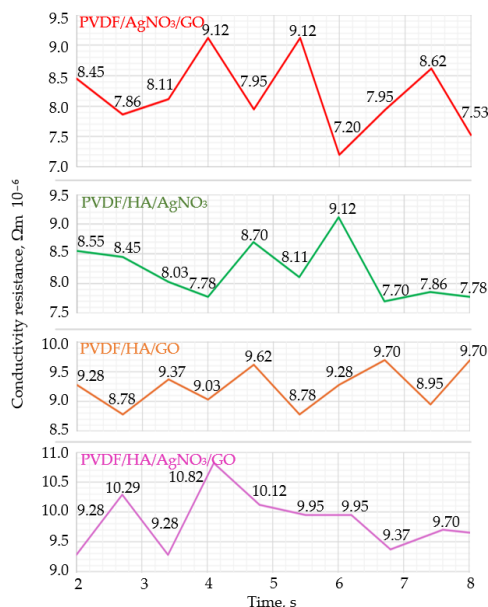
**6.3 lentelė.** Mėginių su PVDF/HA/GO/AgNO<sub>3</sub> koncentracijos ir receptūros

Sample No.	PVDF (g/ml)	HA (g/ml)	GO (g/ml)	AgNO <sub>3</sub> (g/ml)
(1)	0,3 g/2 ml	-	0,3 g/1ml	0,2 g/1ml
(2)	0,3 g/2 ml	0,1 g/1ml	0,3 g/1ml	-
(3)	0,3 g/2 ml	0,1 g/1ml	-	0,2 g/1ml
(4)	0,3 g/2 ml	0,1 g/1ml	0,3 g/1ml	0,2 g/1ml

### 6.5.2. Elektrinis keturių taškų zondo impulsų matavimas

Šiame skyriuje aptariama PVDF, HA, AgNO<sub>3</sub> ir GO įtaka kompozitinių plėvelių elektrinei varžai. 6.14 pav. pateikiami keturių taškų zondo impulsų elektrinio matavimo rezultatai.





**6.14 pav.** Keturių taškų zondo impulsų elektrinio matavimo rezultatai: PVDF/AgNO<sub>3</sub>/GO, PVDF/HA/AgNO<sub>3</sub>, PVDF/HA/GO ir PVDF/HA/AgNO<sub>3</sub>/GO

Kompozito PVDF/AgNO<sub>3</sub>/GO (1 pavyzdys) vidutinė elektrinė varža  $8,20 \times 10^{-6} \Omega m$ . Kai vidutinis atsparumas yra  $8,21 \times 10^{-6} \Omega m$ , HA pridėjimas prie kompozito ir GO pašalinimas nesukėlė jokių pastebimų pakeitimų. Pridėjus GO ir pašalinus AgNO<sub>3</sub> priedą, buvo pastebėtas didesnis pokytis. Vidutinė kompozito elektrinė varža buvo  $9,25 \times 10^{-6} \Omega m$ .

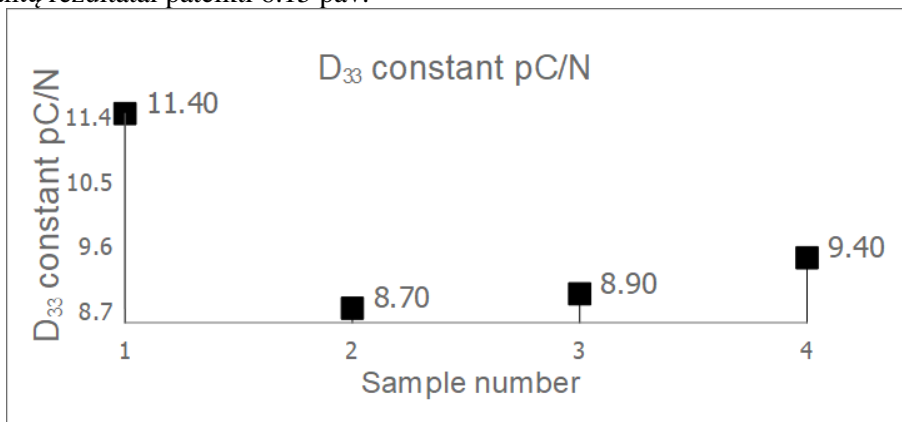
Esant visiems komponentams, elektrinė varža padidėjo labiausiai –  $10,82 \times 10^{-6} \Omega m$ . Šie rezultatai rodo, kad GO, AgNO<sub>3</sub> ir GO gali turėti didesnę poveikį kompozito elektrinėms charakteristikoms nei HA pridėjimas. GO gali padėti perduoti krūvį kompozite, nes tai labai laidi medžiaga. Be to, AgNO<sub>3</sub> gali sudaryti jonines jungtis, kurios gali padidinti bendrą laidumą.

Labai svarbu atsiminti, kad kiti veiksniai, pvz., priedų pasiskirstymas visame kompozite ir naudojamos apdorojimo sąlygos, taip pat gali turėti įtakos laidumui. Nepaisant to, reikia atlikti daugiau tyrimų, kad būtų galima tiksliai nustatyti pastebėtus elektrinių charakteristikų pokyčius.

### 6.5.3. Pjezoelektrinio koeficiento $d_{33}$ matavimo rezultatai

Sukurtų pjezoelektrinių kompozitų  $d_{33}$  reikšmėms matuoti naudotas statinis pjezoelektrinis matuoklis. Kai elektrinis laukas veikia poliarizacijos kryptimi (dažnai trimis kryptimis), medžiaga, turinti didelę  $d_{33}$  vertę, gali sukelti didelį mechaninį įtempį. Kiekvienas šio tyrimo mėginys buvo matuojamas ta pačia jėga  $[\pm 1-2 \text{ N}]$ . 2 pavyzdyje pjezoelektrinis matuoklis rodė mažiausią  $8,70 \text{ pC/N}$  rodmenį. 1 mėginys rodo didžiausius rezultatus  $11,40 \text{ pC/N}$ . Komponentų GO ir AgNO<sub>3</sub> pridėjimas į 1 mėginį davė didžiausią rezultatą, nors 4 mėginio, kuriame yra visi komponentai,

rezultatas yra 9,40 pC/N, tačiau rezultatai taip pat daug žadantys. Pjezoelektrinių  $d_{33}$  konstantų rezultatai pateikti 6.15 pav.



**6.15 pav.**  $d_{33}$  rezultatai (matuojami statiniu  $d_{33}$  matavimo įrenginiu), 1 mėginys – PVDF/AgNO<sub>3</sub>, GO, 2 pavyzdys – PVDF/HA/AgNO<sub>3</sub>, 3 mėginys – PVDF/HA/GO, 4 mėginys – PVDF/HA/AgNO<sub>3</sub>/GO

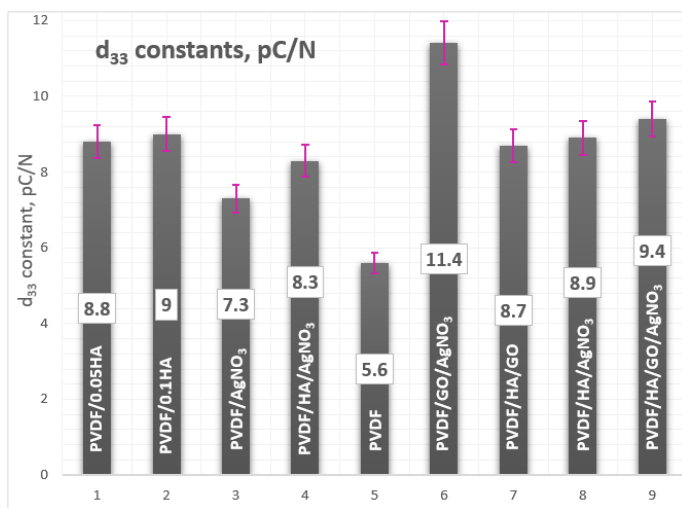
## 6.6. Sukurtų kompozitų rezultatų palyginimas ir GO įtaka savybėms

6.4 lentelėje pateikiami pagaminti kompozitai ir jų koncentracijos, o šiame skyriuje pateikiami kelių matavimo rezultatų palyginimai.

### 6.4 lentelė. Mėginių koncentracijos ir receptai

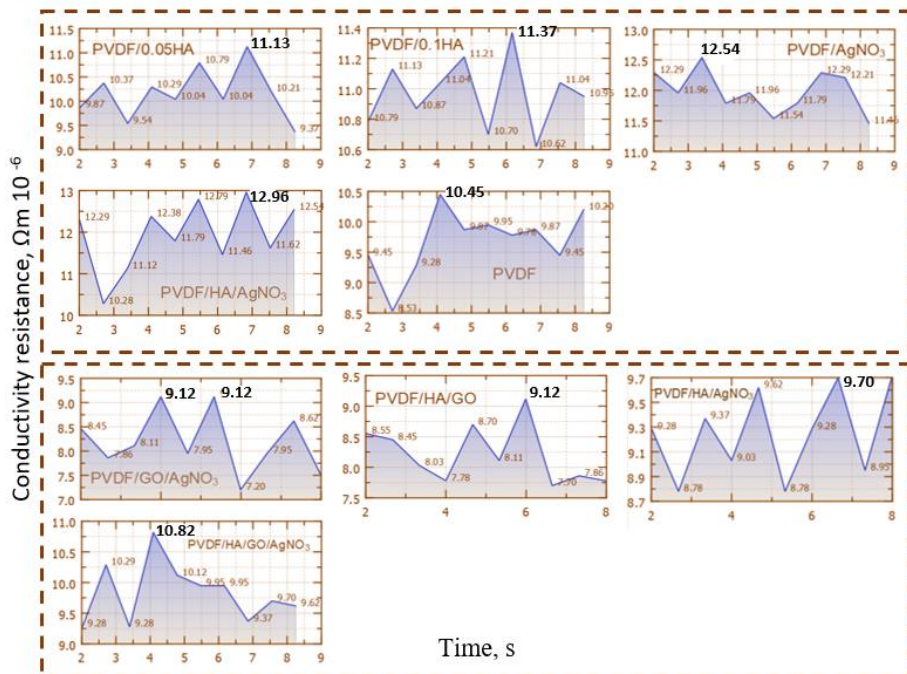
Bandiniai	Receptai (g/ml)
PVDF/0,05HA (	PVDF 0,5 g/2 ml, HA 0,05g/1ml
PVDF/0,1HA	PVDF 0,5 g/2 ml, HA 0,10g/1ml
PVDF/AgNO <sub>3</sub>	PVDF 0,5 g/2 ml, AgNO <sub>3</sub> 0,2g/1ml
PVDF/HA/AgNO <sub>3</sub>	PVDF 0,5g/2 ml, HA 0,05g/1ml, AgNO <sub>3</sub> 0,2g/1ml
PVDF	PVDF 0,5g/2 ml
PVDF/GO/AgNO <sub>3</sub>	PVDF0,3 g/2 ml, GO 0,3 g/1ml, AgNO <sub>3</sub> 0,3 g/1ml
PVDF/HA/GO	PVDF 0,3 g/2 ml, HA 0,1 g/1ml, GO 0,3 g/1ml
PVDF/HA/AgNO <sub>3</sub>	PVDF 0,3 g/2 ml, HA 0,1 g/1ml AgNO <sub>3</sub> 0,3 g/1ml
PVDF/HA/GO/AgNO <sub>3</sub>	PVDF 0,3 g/2 ml, HA 0,1 g/1ml, GO 0,3 g/1ml, AgNO <sub>3</sub> 0,3 g/1ml

6.16 pav. parodyti abiejų kompozitų  $d_{33}$  konstantos rezultatai. Didžiausia konstanta yra 11,40 pC/N PVDF/GO/AgNO<sub>3</sub> kompozite. Taip pat geri rezultatai PVDF/HA/GO/AgNO<sub>3</sub> mėginio – 9,40 pC/N. Mažiausi rezultatai mėginio, kuriame yra gryno atkaitinto PVDF, o tai rodo, kad fazių, tokių kaip GO, AgNO<sub>3</sub> ir HA, pridėjimas turi įtakos  $d_{33}$  rezultatams.



6.16 pav.  $d_{33}$  pjezoelektrinių konstantų visų mėginių palyginimo rezultatai

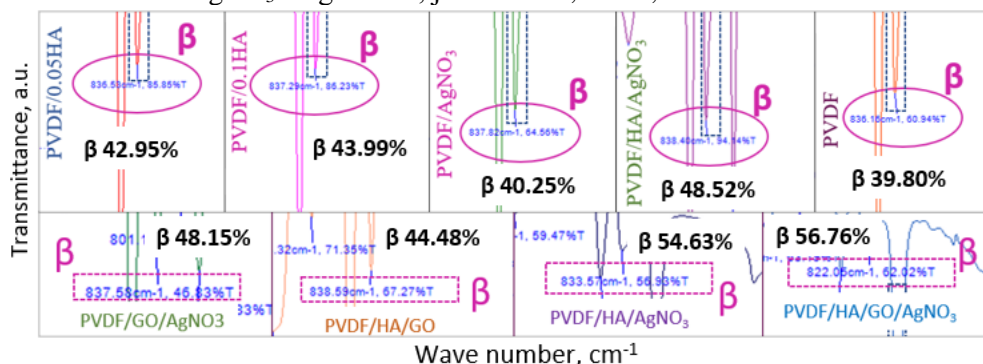
6.17 pav. parodyti 4 zondų elektriniai rezultatai. Aukščiausius rezultatus demonstruoja mėginiai su PVDF/HA ir mėginiai su PVDF/AgNO<sub>3</sub>. Pridėjus visas medžiagas, didžiausias elektrinės varžos padidėjimas buvo  $12,96 \times 10^{-6} \Omega m$ . HA įtraukimas į kompozitą padidina elektrinę varžą. Pridėjus visas medžiagas į PVDF/HA/AgNO<sub>3</sub>/GO mėginį, elektrinė varža padidėjo  $10,82 \times 10^{-6} \Omega m$ .



6.17 pav. 4 zondo matavimų elektros laidumo rezultatai, visų mėginių palyginimas

FTIR spektrai 6.18 pav. parodė, kad juostos, susijusios su PVDF  $\alpha$  ir  $\beta$  fazėmis, buvo labiau paplitusios.

FTIR spektras neatskleidė labai didelio reikšmingo  $\text{AgNO}_3$ , GO ir HA poveikio dėl mažos šių medžiagų koncentracijos ir žemos kristalizacijos temperatūros (90 °C). Kompozitų komponentai iš esmės buvo patvirtinti FTIR spektrais. Tačiau buvo įrodyta, kad visuose mėginiuose buvo PVDF  $\beta$  kristalinė fazė pagal matomas FTIR smailes. Buvo apskaičiuotos  $\beta$  fazės koncentracijos, kurios pateiktos 4.3 pav. Didžiausios  $\beta$  fazės koncentracijos buvo nustatytos PVDF/HA/ $\text{AgNO}_3$  ir PVDF/HA/GO/ $\text{AgNO}_3$  mėginiuose, jos buvo 54,63–56,76 %.

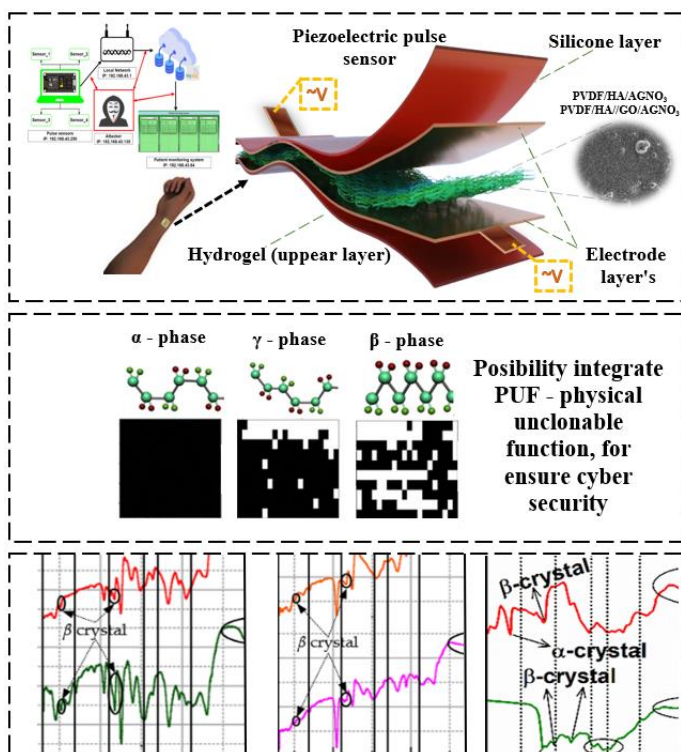


**6.18 pav.** Visų mėginių FTIR spektro rezultatų palyginimas

### 6.6.1. Funkcinio elemento taikymas ir integravimas

Pateiktame tyrime pagrindinis dėmesys skiriamas galutiniam pritaikymui – daugiasluoksniui biojutiklio dizainui. Be paties biojutiklio funkcinio elemento konstrukcijos, taip pat svarbu atsižvelgti į visumą, su kuria jis sąveikaus. 6.19 pav. parodyta biojutiklio konstrukcija jutimo įrenginyje. Vienas biosensoriaus sluoksnis yra funkcinis elementas su dviem elektrodais. Hidrogelis padeda jutikliui geriau liestis su žmogaus oda, o jutimo medžiaga, pagal atliktus tyrimus, parinkta PVDF/HA/ $\text{AgNO}_3$  arba PVDF/HA/GO/ $\text{AgNO}_3$  dėl puikios pjezoelektriškumo ir plastiškumo. Abiejose elektrodo laidininko pusėse uždedamos varinės sidabro pastos juostelės (kievienam elektrodui po vieną), kad būtų geras laidumas, ant jų prilituojamas sujungimo laidas. Visas prietaisas iš abiejų pusių visiškai padengiamas silikono sluoksniu, kad padidintų mechaninį stiprumą ir apsaugotų jutiklį nuo dulkių ir vandens.

Sukurtas funkcinis elementas puikiai tinka pulsui matuoti. FTIR smailės ir rezultatai puikiai atskleidė beta fazės egzistavimą mėginiuose, o tai reiškia, kad papildomos medžiagos ir pasirinktas apdorojimo būdas puikiai tinka beta fazei padidinti ir funkciniam elementams pritaikyti. Beta fazė reikalinga taip pat norint integruoti PUF raktą, kuris užtikrintų saugų funkcinio elemento naudojimą ir apsaugotų paciento duomenis.



**6.19 pav.** Pjezoelektrinio jutiklio struktūra, PUF – funkcija  $\beta$  fazėje ir FTIR  $\beta$  fazės smailės sukurtuose funkciniuose elementuose

## 6.7 Išvados

1. Ištyrus medicinos srityje naudojamų pjezoelektrinių biojutiklių bevielės infrastruktūros saugumo spragas, nustatyta, kad jutikliuose naudojama informacija yra atakų taikinyje. Lanksčiuose ir implantuojamuose jutikliuose naudojama įvairi informacija, kuri gali būti aptikta ir pakeista. Integravus PUF raktą į PVDF  $\beta$  fazę, galima apsaugoti naudojant jutiklius gautą informaciją. Tačiau labai svarbus ir pjezoelektrinio kompozito funkcionalumas ir pritaikomumas formuojant biomechaninius jutiklius. Funkcionalumui padidinti bei mechaninėms, elektrinėms, morfologinėms ir hidrofobinėms savybėms valdyti pasirinktos HA, GO ir  $\text{AgNO}_3$  nanodalelės. Pjezoelektriniuose kompozituose HA užtikrina biosuderinamumą ir padidina pjezoelektrinį efektą, GO gerina elektrines savybes, padidina beta fazės virsmą PVDF polimere, o  $\text{AgNO}_3$  turi antibakterinių savybių bei pagerina krūvio perdavimą. Tokie kompozitai anksčiau nebuvo analizuojami, todėl siekiama sukurti funkcinį elementą, užtikrinantį mechanines, elektrines ir pjezoelektrines savybes bei užtikrinantį perduodamų duomenų saugumą.

2. Sukurta pjezoelektrinio kompozito PVDF pagrindu su HA, GO ir  $\text{AgNO}_3$  nanodalelėmis sintetinimo metodika, užtikrinanti pjezoelektrinių savybių ir beta fazės

transformacijos integraciją kompozitinėje medžiagoje. Sintzei pasirinktas tirpiklio atkaitinimo būdas su DMSO (90 °C, 5 val.). Ant 0,05 mm plieninių elektrodų buvo paruošti įvairių koncentracijų mėginiai. Plėvelė buvo nusodinta ant 0,17 mm storio elektrodo. Paviršiaus šiurkštumo ir multifraktalinių spektrų analizė patvirtino gerą mėginio paruošimo kokybę.

3. Įvertinus HA, ir AgNO<sub>3</sub> nanodalelių įtaką pjezoelektrinio kompozito elektrinėms, mechaninėms ir morfologinėms savybėms bei beta fazių transformacijos užtikrinimui, rezultatai parodė, kad PVDF/HA/AgNO<sub>3</sub>, konstanta  $d_{33}$  yra 8,3 pC/N ir padidėja 33 %. Ištyrta elektrinės charakteristikos, rodančios didžiausias energijos reikšmes komponente PVDF/HA/AgNO<sub>3</sub>, o rezultatai svyravo nuo 56,50 iki 125,20 mV. Keturių taškų zondo matavimas parodė, kad HA ir AgNO<sub>3</sub> įtraukimas į kompozitą padidino elektrinę varžą iki  $12,96 \times 10^{-6} \Omega m$ . Didžiausia beta fazės transformacija užfiksuota tokiuose mėginiuose PVDF/HA/AgNO<sub>3</sub>.

4. Įvertinus GO įtaką PVDF pagrindu pagaminto kompozito pjezoelektrinėms, elektrinėms ir morfologinėms savybėms, jutimo taikymui, rezultatai parodė, kad PVDF/AgNO<sub>3</sub>/GO mėginyje buvo geriausi pjezoelektriniai radiniai esant 11,40 pC/N. FTIR rezultatai rodo, kad HA, GO arba AgNO<sub>3</sub> veikia beta fazės transformaciją kompozituose ir didžiausią beta fazės koncentracija yra 56,76%. Didžiausias elektrinės varžos padidėjimas rastas PVDF/HA/AgNO<sub>3</sub>/GO mėginyje –  $10,82 \times 10^{-6} \Omega m$ .  $\beta$  fazė reikalinga ir PUF rakto integravimui, kuris užtikrintų saugų funkcinio elemento naudojimą. Sukurtas beta fazės transformacija pasižymintis pjezoelektrinis kompozitas yra tinkamas biomechaninių jutiklių kūrimui.

## REFERENCES

1. WANG, Ting; Ming WANG; Le YANG; Zhuyun LI; Xian Jun LOH and Xiaodong CHEN. Cyber–Physiochemical Interfaces. *Advanced Materials*, 32, 2020, 8, 1905522. Accessed via: Wiley Online Library, <https://doi.org/10.1002/adma.201905522>.
2. LABRADO, Carson; Himanshu THAPLIYAL; Stacy PROWELL and Teja KURUGANTI. Use of Thermistor Temperature Sensors for Cyber-Physical System Security. *Sensors*, 19, 2019, 18, 390. Accessed via: <https://doi.org/10.3390/s19183905>.
3. WU, Cong; Yufei TANG; Bobo MAO; Kang ZHAO; Siyue CAO and Zixiang WU. Rapid Apatite Induction of Polarized Hydrophilic HA/PVDF Bio-Piezoelectric Coating on Titanium Surface. *Surface and Coatings Technology*, 405, 2021, 126510. Accessed via: ScienceDirect, <https://doi.org/10.1016/j.surfcoat.2020.126510>.
4. RIBEIRO, A. A.; L. G. VAZ; A. C. GUASTALDI and J. S. C. CAMPOS. Adhesion Strength Characterization of PVDF/HA Coating on Cp Ti Surface Modified by Laser Beam Irradiation. *Applied Surface Science*, 258, 2012, 10110–10114. Accessed via: ScienceDirect, <https://doi.org/10.1016/j.apsusc.2012.06.084>.
5. LEWIS, Stephen M. Emerging Biosecurity Considerations at the Intersection of Biotechnology and Technology. In *Applied Biosecurity: Global Health, Biodefense and Developing Technologies*, pp. 121–132. Cham: Springer, 2021. Accessed via: <https://doi.org/10.1007/978-3-030-69464-7>.
6. MCGOLDRICK, Leif K. and Jan HALÁMEK. Recent Advances in Noninvasive Biosensors for Forensics, Biometrics, and Cybersecurity. *Sensors*, 20, 2020, 21, 5974. Accessed via: <https://doi.org/10.3390/s20215974>.
7. HAN, Youngmin; Subin LEE; Eun Kwang LEE; Hocheon YOO and Byung Chul JANG. Strengthening Multi-Factor Authentication Through Physically Unclonable Functions in PVDF-HFP-Phase-Dependent a-IGZO Thin-Film Transistors. *Advanced Science*, 11, 2024, 18. Accessed via: Wiley Online Library, <https://doi.org/10.1002/advs.202309221>.
8. NI, Li; Pengjun WANG; Yuejun ZHANG; Gang LI; Lin DING and Jiliang ZHANG. PI PUF: A Processor-Intrinsic PUF for IoT. *Computers and Electrical Engineering*, 105, 2023, 108540. Accessed via ScienceDirect: <https://doi.org/10.1016/j.compeleceng.2022.108540>.
9. GADGE, J. and A. A. PATIL. Port scan detection. In *2008 16th IEEE International Conference on Networks*. 2008, 1–6. Accessed via: IEEE, <https://doi.org/10.1109/ICON.2008.4772622>.
10. ARLETT, J. L.; E. B. MYERS and M. L. ROUKES. Comparative advantages of mechanical biosensors. *Nature Nanotechnology*, 6, 2011, 203–215. Accessed via: <https://doi.org/10.1038/nnano.2011.44>.
11. JIANRONG, Chen; Miao YUQING; He NONGYUE; Wu XIAOHUA and Li SIJIAO. Nanotechnology and biosensors. *Biotechnology Advances*, 22, 2004, 7, 505–518. Accessed via: ScienceDirect, <https://doi.org/10.1016/j.biotechadv.2004.03.004>.
12. WU, Tianqiong; Di YOU; Huayun GAO; Pinghua LIAN; Weigang MA; Xinyi ZHOU; Chuanmin WANG; Jianghai LUO; Haibo ZHANG and Hua TAN. Research Status and Development Trend of Piezoelectric Accelerometer. *Crystals*, 13, 2023, 9. Accessed via: <https://doi.org/10.3390/cryst13091363>.
13. LI, Pei; Yong ZHANG; Chunbao LI; Xian CHEN; Xin GOU; Yong ZHOU; Jun YANG and Lei XIE. From materials to structures: a holistic examination of achieving linearity in flexible pressure sensors. *Nanotechnology*, 36, 2024, 4, 042002, 27. Accessed via: <https://doi.org/10.1088/1361-6528/ad8750>.

14. KIM, Kyungrim; Jinwook KIM; Xiaoning JIANG and Taeyang KIM. Static Force Measurement Using Piezoelectric Sensors. *Journal of Sensors*, 2021, 2021, 1. Accessed via: Wiley Online Library, <https://doi.org/10.1155/2021/6664200>.
15. YAGHOOTKAR, Bahareh; Soheil AZIMI and Behraad BAHREYNI. A High-Performance Piezoelectric Vibration Sensor. *IEEE Sensors Journals*, 17, 2017, 13, 4005–4012. Accessed via: IEEE Xplore, <https://doi.org/10.1109/JSEN.2017.2707063>.
16. AKSEL, Elena and Jacob L. JONES. Advances in Lead-Free Piezoelectric Materials for Sensors and Actuators. *Sensors*, 10, 2010, 3, 395–1954. Accessed via: <https://doi.org/10.3390/s100301935>.
17. DASHTIZAD, Soroush; Alizadeh PARVIN and Amin YOURDKHANI. Improving piezoelectric properties of PVDF fibers by compositing with BaTiO<sub>3</sub>-Ag particles prepared by sol-gel method and photochemical reaction. *Journal of Alloys and Compounds*, 883, 2021, 160810. Accessed via: ScienceDirect, <https://doi.org/10.1016/j.jallcom.2021.160810>.
18. WANG, Menglong; Ke WANG; Yaoyao YANG; Yanan LIU and Deng-Guang YU. Electrospun Environment Remediation Nanofibers Using Unspinnable Liquids as the Sheath Fluids: A Review. *Polymers*, 12, 2020, 103. Accessed via: <https://doi.org/10.3390/polym12010103>.
19. DAS MAHAPATRA, Susmriti; Preetam Chandan MOHAPATRA, Adrianus Indrat ARIA, Graham CHRISTIE, Yogendra Kumar MISHRA, Stephan HOFMANN, Vijay Kumar THAKUR. Piezoelectric Materials for Energy Harvesting and Sensing Applications: Roadmap for Future Smart Materials. *Advanced Science*, 8, 2021, 17, 2100864. Accessed via: Wiley Online Library, <https://doi.org/10.1002/adv.202100864>.
20. STEJSKAL, Jaroslav. Conducting Polymer-Silver Composites. *Chemical Papers*, 67, 2013, 8, 814–848. Accessed via: <https://doi.org/10.2478/S11696-012-0304-6>.
21. TANDON, Biranche; Prashant KAMBLE; Richard T. OLSSON; Jonny J. BLAKER and Sarah H. CARTMELL. Fabrication and Characterisation of Stimuli Responsive Piezoelectric PVDF and Hydroxyapatite-Filled PVDF Fibrous Membranes. *Molecules*, 24, 2019, 1903. Accessed via: <https://doi.org/10.3390/molecules24101903>.
22. KUANG, X.; Z. LIU and H. ZHU. Dielectric properties of Ag@C/PVDF composites. *Journal of Applied Polymer Science*, 129, 2013, 3411–3416.
23. BRAGA, F. J. C.; S. O. ROGERO; A. A. COUTO; R. F. C. MARQUES; A. A. RIBEIRO and J. S. de C. CAMPOS. Characterization of PVDF/HAP Composites for Medical Applications. *Materials Research*, 10, 2007, 3, 247–251. Accessed via: <https://doi.org/10.1590/S1516-14392007000300005>.
24. ZAMIN, Hasnat; Takeshi YABUTSUKA and Shigeomi TAKAI. Bioactivity Assessment of Apatite Nuclei-PVDF Composite Thin Films. *Key Engineering Materials*, 782, 2018, 78–83. Accessed via: <https://doi.org/10.4028/www.scientific.net/KEM.782.78>.
25. SILVA, L. M.; T. G. M. BONADIO; J. M. ROSSO; G. S. DIAS; L. F. CÓTICA; W. R. WEINAND; R. Y. MIYAHARA; I. A. SANTOS and V. F. FREITAS. On the Synthesis and Characterization of (Bio)Ferroelectrically Active PVDF-BCP Composites. *Ferroelectrics*, 553, 2019, 63–71. Accessed via: <https://doi.org/10.1080/00150193.2018.1470840>.
26. JU Min, Zhongshang DOU, Jia-Wang LI, Xuting QIU, Binglin SHEN, Dawei ZHANG, Fang-Zhou YAO, Wen GONG and Ke WANG. Piezoelectric Materials and Sensors for Structural Health Monitoring: Fundamental Aspects, Current Status, and Future Perspectives. *Sensors*, 23, 2023, 1, 543. Accessed via: <https://doi.org/10.3390/s23010543>.



27. AL-AUBIDY, Kasim M.; Ahmad M. DERBAS and Abdullah W. AL-MUTAIRI. Real-time patient health monitoring and alarming using wireless-sensor-network. In *2016 13th International Multi-Conference on Systems, Signals & Devices (SSD)*, 2016, 416–423. Accessed via: IEEE Xplore, <https://doi.org/10.1109/SSD.2016.7473672>.
28. CALDERON, Paulino. *Nmap Network Exploration and Security Auditing Cookbook: Network discovery and security scanning at your fingertips*. 3<sup>rd</sup> ed. Birmingham: Packt Publishing Ltd. 2021.
29. RIBEIRO, A. A.; R. F. C. MARQUES; A. C. GUASTALDI and J. S DE CARVALHO CAMPOS. Hydroxyapatite Deposition Study through Polymeric Process on Commercially Pure Ti Surfaces Modified by Laser Beam Irradiation. *Journal of Materials Science*, 44, 2009, 4056–4061. Accessed via: Springer Nature Link, <https://doi.org/10.1007/s10853-009-3585-6>.
30. UL SAMI, Iftikhar; Maaz Bin AHMAD; Muhammad ASIF and Rafi ULLAH. R. DoS/DDoS detection for E-Healthcare in internet of things. *International Journal of Advanced Computer Science and Applications*, 9, 2018, 1. Accessed via: <https://doi.org/10.14569/IJACSA.2018.090140>.
31. SALEM, Osman; Khalid ALSUBHI; Aymen SHAAFI, Mostafa GHERYANI; Ahmed MEHAOUA and Raouf BOUTABA. Man-in-the-Middle attack mitigation in internet of medical things. *IEEE Transactions on Industrial Informatics*, 18, 2021, 3, 2053–2062. Accessed via: IEEE Xplore, <https://doi.org/10.1109/TII.2021.3089462>.
32. ALKEEM, E. A.; D. SHEHADA; C. Y. YEUN; M. J. ZEMERLY ir J. HU. New secure healthcare system using cloud of things. *Cluster Computing*, 20, 2017, 2211–2229. Accessed via: Springer Nature Link, <https://doi.org/10.1007/s10586-017-0872-x>.
33. MALLIK, Avijit. Man-in-the-middle-attack: Understanding in simple words. *Cyberspace: Jurnal Pendidikan Teknologi Informasi*, 2, 2019, 2, 109–134. Accessed via: <http://dx.doi.org/10.22373/cj.v2i2.3453>.
34. MANIRIHO, Pascal; Ephrem NIYIGABA; Zephania BIZIMANA; Valens TWIRINGIYIMANA; Leki Jovial MAHORO and Tohari AHMAD. Anomaly-based intrusion detection approach for IoT networks using machine learning. In *2020 International Conference on Computer Engineering, Network, and Intelligent Multimedia (CENIM)*, 2020, 303–308. Accessed via: IEEE Xplore, <https://doi.org/10.1109/CENIM51130.2020.9297958>.
35. ISLAS-GARCIA, E.; C. R. TORRES-SANMIGUEL; M. TREJO-VALDEZ; C. MERCADO-ZUNIGA; F. RAMIREZ-CRESCENCIO; R. VILLARROEL; C. TORRES-TORRES and J. A. GARCIA-MERINO. Interferometric characterization of high-frequency piezoelectric effects in hydroxyapatite thin films. *Sensors and Actuators A: Physical*, 372, 2024, 115327. Accessed via ScienceDirect, <https://doi.org/10.1016/j.sna.2024.115327>.
36. MICHELENA, Alvaro; José AVELEIRA-MATA; Esteban JOVE; Martín BAYÓN-GUTIÉRREZ; Paulo NOVAIS; Oscar Fontenla ROMERO, José Luis CALVO-ROLLE and Héctor ALÁIZ-MORETÓN. A novel intelligent approach for man-in-the-middle attacks detection over internet of things environments based on message queuing telemetry transport. *Expert Systems*, 41, 2024, 2. Accessed via: Wiley Online Library, <https://doi.org/10.1111/exsy.13263>.
37. PARIDA, Ap; Sujana SWAIN; Rashmirekha SAHU; Rashmi Rekha NEGI; Buddhadev SAMANTA and Pawan KUMAR. Phase formation and electrical properties study of PVDF thick films synthesized by solution casting method. *International Journal of Materials Research (formerly Zeitschrift fuer Metallkunde)*, 114, 2023, 4–5. Accessed via: <https://doi.org/10.1515/ijmr-2022-0229>.

38. KHANDURI, Priya; Varij PANWAR and Sribidhya MOHANTY. Analysis of PVDF/AgNO<sub>3</sub> conductive membrane. *Materials Today: Proceedings*, 46, 2021, 20, 11002–11006. Accessed via: ScienceDirect, <https://doi.org/10.1016/j.matpr.2021.02.096>.
39. MORE, Namdev; Akshay SRIVASTAVA and Grovinda KAPUSETTI. Graphene Oxide Reinforcement Enhances the Piezoelectric and Mechanical Properties of Poly(3-hydroxybutyrate-co-3-hydroxy valerate)-Based Nanofibrous Scaffolds for Improved Proliferation of Chondrocytes and ECM Production. *ACS Applied Bio Materials*, 3, 2020, 10, 6823–6835. Accessed via: <https://doi.org/10.1021/acsabm.0c00765>.
40. MUDULI, Sakti P.; Sabyasachi PARIDA; Sanjay K. BEHURA; Shailendra RAJPUT, Sanjeeb K. ROUT and Shweta SAREEN. Synergistic effect of graphene on dielectric and piezoelectric characteristic of PVDF-(BZT-BCT) composite for energy harvesting applications. *Polymer for Advanced Technologies*, 33, 2022, 10, 3628–3642. Accessed via: Wiley Online Library, <https://doi.org/10.1002/pat.5816>.
41. ISSA, Ahmed A.; Miaram A. AL-MAADEED; Adriaan S. LUYT; Deepalekshmi PANNAMMA, Mohammad K. HASSAN. Physico-Mechanical, Dielectric, and Piezoelectric Properties of PVDF Electrospun Mats Containing Silver Nanoparticles. *C*, 3, 2017, 3. Accessed via: <https://doi.org/10.3390/c3040030>.
42. XU, Lanxin; Jiali MA; Guodong WEI; Chenjie GU and Too JIANG. Improved surface-enhanced Raman scattering performance enabled by hydrophilic-hydrophobic piezoelectric PVDF-silver substrate. *Sensors and Actuators B: Chemical*, 370, 2022, 132431. Accessed via: ScienceDirect, <https://doi.org/10.1016/j.snb.2022.132431>.
43. PARIY, Igor O.; Anna A. IVANOVA; Vladimir V. SHVARTSMAN; Doru C. LUPASCU; Gleb B. SUKHORUKOV; Tim LUDWIG; Ausrine BARTASYTE; Sanjay MATHUR; Maria A. SURMENEVA and Roman A. SURMENEV. Piezoelectric Response in Hybrid Micropillar Arrays of Poly(Vinylidene Fluoride) and Reduced Graphene Oxide. *Polymers*, 11, 2019, 6. Accessed via: <https://doi.org/10.3390/polym11061065>.
44. BHATTI, Imtiaz Noor; M. BANERJEE and Ilyas Noor BHATTI. Effect of Annealing and Time of Crystallization on Structural and Optical Properties of PVDF Thin Film Using Acetone as Solvent. *IOSR Journal of Applied Physics*, 4, 2013, 4, 42–47. Accessed via: <https://doi.org/10.9790/4861-0444247>.
45. ENAYATZADEH, Mohammad and Toraj MOHAMMADI. Morphology and Performance of Poly(Vinylidene Fluoride) Flat Sheet Membranes: Thermodynamic and Kinetic Aspects. *Journal of Applied Polymer Science*, 135, 2018, 46419. Accessed via: Wiley Online Library, <https://doi.org/10.1002/app.46419>.
46. AREFI-OSKOU, Samira; Alireza KHATAEE and Vahid VATANPOUR. Effect of Solvent Type on the Physicochemical Properties and Performance of NLDH/PVDF Nanocomposite Ultrafiltration Membranes. *Separation and Purification Technology*, 184, 2017, 97–118. Accessed via: ScienceDirect, <https://doi.org/10.1016/j.seppur.2017.04.040>.
47. RABIEI, Marzieh; Arvydas, Palevicius; Reza EBRAHIMI-KAHRIZSANGI; Sohrab NASIRI; Andrius VILKAUSKAS and Giedrius JANUSAS. New Approach for Preparing In Vitro Bioactive Scaffold Consisted of Ag-Doped Hydroxyapatite + Polyvinyltrimethoxysilane. *Polymers*, 13, 2021, 11, 1695. Accessed via: <https://doi.org/10.3390/polym13111695>.
48. ARAMI, H.; M. MOHAJERANI; M. MAZLOUMI; R. KHALIFEHZADEH; A. Lak and S. K. SADRNEZHAAD. Rapid Formation of Hydroxyapatite Nanostrips via Microwave Irradiation. *Journal of Alloys and Compounds*, 469, 2009, 1–2, 391–394. Accessed via: ScienceDirect, <https://doi.org/10.1016/j.jallcom.2008.01.116>.

49. FERN, Hor Wee and M. N. SALIMI. Hydroxyapatite Nanoparticles Produced by Direct Precipitation Method: Optimization and Characterization Studies. *AIP Conference Proceedings*, 2339, 2021, 1, 020215. Accessed via: <https://doi.org/10.1063/5.0044252>.
50. XIAO, Bo; Gugu N. RUTHERFORD; Amrit P. SHARMA; Sangram K. PRADHAN; Carl E. BONNER and Messaoud J. BAHOURA. Surface Modification and Charge Injection in a Nanocomposite of Metal Nanoparticles and Semiconductor Oxide Nanostructures. *Scientific Reports*, 10, 2020, 4743. Accessed via: <https://doi.org/10.1038/s41598-020-58308-9>.
51. ALENCHERRY, Tinto; Naveen, A. R.; Somnath GHOSH; Jency DANIEL and Venkataraghavan R. Effect of increasing electrical conductivity and hydrophilicity on the electrosorption capacity of activated carbon electrodes for capacitive deionization. *Desalination*, 415, 2017, 14–19. Accessed via: ScienceDirect, <https://doi.org/10.1016/j.desal.2017.04.001>.
52. ABDULLAH, Ibtisam Yahya; Muhammad YAHAYA; Mohd Hafizuddin JUMALI and Haider Homammed SHANSHOOL. Effect of Annealing Process on the Phase Formation in Poly(Vinylidene Fluoride) Thin Films. *AIP Conference Proceedings*, 1614, 2014, 1, 147–151. Accessed via: <https://doi.org/10.1063/1.4895187>.
53. MEANEY, Paul M.; Colleen J. FOX; Shireen D. GEIMER and Keith D. PAULSEN. Electrical Characterization of Glycerin: Water Mixtures: Implications for Use as a Coupling Medium in Microwave Tomography. *IEEE Transactions on Microwave Theory and Techniques*, 65, 2017, 5, 1471–1478. Accessed via: IEEE Xplore, <https://doi.org/10.1109/TMTT.2016.2638423>.
54. ATAC, Cihan and Sedat AKLEYLEK. A survey on security threats and solutions in the age of IoT. *Avrupa Bilim ve Teknoloji Dergisi*, 15, 2019, 36–42. Accessed via: <https://doi.org/10.31590/ejosat.494066>.
55. MALIK, Shiza; Khalid MUHAMMAD and Yasir WAHEED. Nanotechnology: A Revolution in Modern Industry. *Molecules*, 28, 2023, 2, 661. Accessed via: <https://doi.org/10.3390/molecules28020661>.
56. HU, Xiaokai; Liming ZHU; Kangjun DIAO; Wei LIU; Xin DENG and Han WANG. Electrostatic derivation for the van der Pauw formula and simulation using arbitrarily shaped resistive materials. *AIP Advances*, 12, 2022, 7, 075208. Accessed via: <https://doi.org/10.1063/5.0081561>.
57. KANG, Jeon-Hong; Sang-Hwa LEE; Hyun RUH and Kwang-Min YU. Development of a Thickness Meter for Conductive Thin Films Using Four-Point Probe Method. *Journal of Electrical Engineering & Technology*, 16, 2021, 2265–2273. Accessed via: Springer Nature Link, <https://doi.org/10.1007/s42835-021-00725-5>.
58. LI, J. C.; Y. WANG and D. C. BA. Characterization of Semiconductor Surface Conductivity by Using Microscopic Four-Point Probe Technique. *Physics Procedia*, 32, 2012, 347–355. Accessed via: ScienceDirect, <https://doi.org/10.1016/j.phpro.2012.03.568>.
59. MARINO, Tiziana; Francesco GALIANO; Silvia SIMONE and Alberto FIGOLI. DMSO EVOL™ as Novel Non-Toxic Solvent for Polyethersulfone Membrane Preparation. *Environmental Science and Pollution Research*, 26, 2019, 14774–14785. Accessed via: Springer Nature Link, <https://doi.org/10.1007/s11356-018-3575-9>.
60. FIGOLI, A.; T. MARINO; S. SIMONE, S.; E. DI NICOLÒ; X.-M. LI; T. HE; S. TORNAGHI and E. DRIOLI. Towards Non-Toxic Solvents for Membrane Preparation: A Review. *Green Chemistry*, 16, 2014, 9, 4034–4059. Accessed via: <https://doi.org/10.1039/C4GC00613E>.
61. HAI, Chunxi; Song LI; Yuan ZHOU; Jinbo ZENG; Xiufeng REN and Xiang LI. Roles of Ethylene Glycol Solvent and Polymers in Preparing Uniformly Distributed MgO

- Nanoparticles. *Journal of Asian Ceramic Societies*, 5, 2017, 176–182. Accessed via: Taylor & Francis Online, <https://doi.org/10.1016/j.jascer.2017.04.004>.
62. MIRKOVIC, Jelena and Peter REIHER. A taxonomy of DDoS attack and DDoS defense mechanisms. *ACM SIGCOMM Computer Communication Review*, 34, 2004, 2, 39–53. Accessed via: ACM Digital Library, <https://doi.org/10.1145/997150.997156>.
  63. SEDLARIK, Vladimir; Tsermaa GALYA; Jana SEDLARIKOVA; Pavel VALASEK and Petr SAHA. The Effect of Preparation Temperature on the Mechanical and Antibacterial Properties of Poly(Vinyl Alcohol)/Silver Nitrate Films. *Polymer Degradation and Stability*, 95, 2010, 399–404. Accessed via ScienceDirect, <https://doi.org/10.1016/j.polymdegradstab.2009.11.017>.
  64. SONG, Guanghui; Yaojin WANG and Daniel Q. TAN. A review of surface roughness impact on dielectric film properties. *IET Nanodielectrics*, 5, 2021, 1, 1–23. Accessed via: <https://doi.org/10.1049/nde2.12026>.
  65. NASR-ESFAHANI, Mojtaba and Sohrab NASIRI. Bioactive Organic-Inorganic Composite Monolith Derived from Poly Vinyl Trimethoxy Silane Using Sol- Gel Process. *Plastic and Polymer Technology (PAPT)*, 2, 2013, 3, 63–67. Accessed via: <https://www.researchgate.net/publication/360806196>.
  66. CAI, Xiaomei; Tingping LEI; Daoheng SUN and Liwei LIN. A Critical Analysis of the a, b and g Phases in Poly(Vinylidene Fluoride) Using FTIR. *RSC Advances*, 7, 2017, 15382–15389. Accessed via: <https://doi.org/10.1039/C7RA01267E>.
  67. LI, Man; Xiangmei LIU; Ziqiang XU; K W K YEUNG and Shuilin WU. Dopamine Modified Organic-Inorganic Hybrid Coating for Antimicrobial and Osteogenesis. *ACS Appl Mater Interfaces*, 8, 2016, 49, 33972–33981. Accessed via: PubMed, <https://doi.org/10.1021/acsami.6b09457>.
  68. NEWMAN, B. A.; C. H. YOON; K. D. PAE and J. I. SCHEINBEIM. Piezoelectric Activity and Field-induced Crystal Structure Transitions in Poled Poly(Vinylidene Fluoride) Films. *Journal of Applied Physics*, 50, 1979, 10, 6095–6100. Accessed via: <https://doi.org/10.1063/1.325778>.
  69. KANCHANA, P. and C. SEKAR. Influence of Sodium Fluoride on the Synthesis of Hydroxyapatite by Gel Method. *Journal of Crystal Growth*, 312, 2010, 6, pages 808–816. Accessed via: ScienceDirect, <https://doi.org/10.1016/j.jcrysgro.2009.12.032>.
  70. ZHAO, Q.; H. LU; L. MENG and S. L. YU. The Adsorption Performance of Hybrid PVDF Membrane by HA. *Applied Mechanics and Materials*, 700, 2015, 298–301. Accessed via: <https://doi.org/10.4028/www.scientific.net/AMM.700.298>.
  71. INCE-GUNDUZ, B. Seyhan; Robert ALPERN; Debeshu AMARE; Jennifer CRAWFORD; Breanna DOLAN; Stacey JONES; Ryan KOBYLARZ; Matthew REVELEY and Peggy CEBE. Impact of Nanosilicates on Poly(Vinylidene Fluoride) Crystal Polymorphism: Part 1. Melt-Crystallization at High Supercooling. *Polymer*, 51, 2010, 6, 1485–1493. Accessed via: ScienceDirect, <https://doi.org/10.1016/j.polymer.2010.01.011>.
  72. PON-ON, Weeraphat; Siwaporn MEEJOO and I-Ming TANG. Incorporation of iron into nano hydroxyapatite particles synthesized by the microwave process. *International Journal of Nanoscience*, 6, 2011, 1, 9–16. Accessed via: <https://doi.org/10.1142/S0219581X07004262>.
  73. ROOPAA, T. S.; H. N. MURTHY; V. P. KUMAR and M. KRISHNA. Development and Characterization of PVDF Thin Films for pressure sensors. *Materials Today: Proceedings*, 5, 2018, 10, 1, 21082–21090. Accessed via: ScienceDirect, <https://doi.org/10.1016/j.matpr.2018.06.503>.
  74. LAK, Aidin; Mahyar MAZLOUMI; Matin Sadat MOHAJERANI, Saeid ZANGANEH, Mohammad Reza SHAYEGH, Amir KAJBAFVALA, Hamed ARAMI

- and Saeyed Khatiboleslam SADRNEZHAAD. Rapid Formation of Mono-Dispersed Hydroxyapatite Nanorods with Narrow-Size Distribution via Microwave Irradiation. *Journal of the American Ceramic Society*, 91, 2008, 11, 3850–3584. Accessed via: <https://DOI:10.1111/j.1551-2916.2008.02690.x>.
75. ZHANG, Liang; Dingquan XIAO and Jian MA. Dielectric Properties of PVDF/Ag/BaTiO<sub>3</sub>Composites. *Ferroelectrics*, 455, 2013, 1, 77–82. Accessed via: Taylor & Francis Online, <https://doi.org/10.1080/00150193.2013.844011>.
  76. MALHERBI, Milena S.; Luciano C. DIAS; Mariana S. Z. LIMA; Larissa G. RIBEIRO; Valdirlei F. FREITAS, et al. Electrically stimulated bioactivity in hydroxyapatite/ $\beta$ -tricalciumphosphate/polyvinylidene fluoride biocomposites. *Journal of Materials Research and Technology*, 20, 2022, 169–179. Accessed via: ScienceDirect, <https://doi.org/10.1016/j.jmrt.2022.06.151>.
  77. LI, Xiongjie; Yiping WANG; Tingrui HE; Querui HU and Ying YANG. Preparation of PVDF flexible piezoelectric film with high  $\beta$ -phase content by matching solvent dipole moment and crystallization temperature. *Journal of Materials Science: Materials in Electronics*, 30, 2019, 20174–20180. Accessed via: Springer Nature Link, <https://doi.org/10.1007/s10854-019-02400-y>.
  78. SATAPATHY, Srinibas; Santosh PAWAR; P. K. GUPTA and K. B. R. VARMA. Effect of annealing on phase transition in poly(vinylidene fluoride) films prepared using polar solvent. *Bulletin of Materials Science*, 34, 2011, 4, 727–733. Accessed via: Springer Nature Link, <https://doi.org/10.1007/s12034-011-0187-0>.
  79. HARI, M. Arjun; Lintu RAJAN; Subash C. K. and Soney VARGHESE. Effect of nanoparticle size on the piezoelectric properties of PVDF based nanocomposite thin films. *Materials Today: Proceedings*, 46, 2021, 12, 5781–5784. Accessed via: ScienceDirect, <https://doi.org/10.1016/j.matpr.2021.02.715>.
  80. XIE, Linfang; Guoliang WANG; Chao JIANG; Fapeng YU and Xian ZHAO. Properties and Applications of Flexible Poly(Vinylidene Fluoride)-Based Piezoelectric Materials. *Crystals*, 11, 2021, 6, 644. Accessed via: <https://doi.org/10.3390/cryst11060644>.
  81. Ruan, Liuxia; Xiannian YAO; Yufang CHANG; Lianqun ZHOU; Gaowu QIN and Xianmin ZHANG. Properties and Applications of the  $\beta$  Phase Poly(vinylidene fluoride). *Polymers*, 10, 2018, 3, 228. Accessed via: <https://doi.org/10.3390/polym10030228>.
  82. CHOI, Jinwoo; Kyuho LEE; Minhwan LEE; Taebin KIM; Sangwon EOM, et al. High  $\beta$ -phase Poly(vinylidene fluoride) Using a Thermally Decomposable Molecular Splint. *Advanced Electronic Materials*, 9, 2023, 1, 2200279. Accessed via: Wiley Online Library, <https://doi.org/10.1002/aelm.202200279>.
  83. FRITZ, Sandra, E.; Tommie Wilson KELLEY and C. Daniel FRISBIE. Effect of Dielectric Roughness on Performance of Pentacene TFTs and Restoration of Performance with a Polymeric Smoothing Layer. *The Journal of Physical Chemistry B*, 109, 2005, 21, 10574–10577. Accessed via: <https://doi.org/10.1021/jp044318f>.
  84. YI, Zhengkun and Yilei ZHANG. Recognizing tactile surface roughness with a biomimetic fingertip: A soft neuromorphic approach. *Neurocomputing*, 244, 2017, 102–111. Accessed via: ScienceDirect, <https://doi.org/10.1016/j.neucom.2017.03.025>.
  85. YI, Zhengku; Yilei ZHANG and Jan PETERS. Bioinspired tactile sensor for surface roughness discrimination. *Sensors and Actuators: A Physical*, 255, 2017, 46–53. Accessed via: ScienceDirect, <https://doi.org/10.1016/j.sna.2016.12.021>.
  86. SUH, Alison Y. and Andreas A. POLYCARPOU. Effect of Molecularly Thin Lubricant on Roughness and Adhesion of Magnetic Disks Intended for Extremely High-Density Recording. *Tribology Letters*, 15, 2003, 365–376. Accessed via: Springer Nature Link, <https://doi.org/10.1023/B:TRIL.0000003059.62250.88>.

87. XIE, Jing; Yang QIAO; Zu'an WANG; Yuanshen QI; Quingfeng XU, et al. Application of the Taguchi method to areal roughness-based surface topography control by waterjet treatments. *Applied Surface Science Advances*, 19, 2024, 100548. Accessed via: ScienceDirect, <https://doi.org/10.1016/j.apsadv.2023.100548>.
88. KRUPINSKI, Michal; Anna WAWRZASZEK; Wojciech DRZEWIECKI; Malgorzata JENEROWICZ and Sebastian ALEKSANDROWICZ. What Can Multifractal Analysis Tell Us about Hyperspectral Imagery? *Remote Sensing*, 12, 2020, 24, 4077. Accessed via: <https://doi.org/10.3390/rs12244077>.
89. KRZYSZCZAK, Jaromir; Piotr BARANOWSKI; Monika ZUBIK; Valentin KAZANDJIEV; Veska GEORGIEVA, et al. Multifractal characterization and comparison of meteorological time series from two climatic zones. *Theoretical and Applied Climatology*, 137, 2019, 1811–1824. Accessed via: Springer Nature Link, <https://doi.org/10.1007/s00704-018-2705-0>.
90. CHINAGLIA, Dante Luis; Rinaldo GREGORIO JR; Josiani Christina STEFANELLO; Ruy Alberto Pisani ALTAFIM; Werner WIRGES; Feipeng WANG and Reimund GERHARD. Influence of the Solvent Evaporation Rate on the Crystalline Phases of Solution-Cast Poly(Vinylidene Fluoride) Films. *Journal of Applied Polymer Science*, 116, 2010, 2, 785–791. Accessed via: Wiley Online Library, <https://doi.org/10.1002/app.31488>.
91. KATO, Sota; Shigeki FURUKAWA; Daisuke AOKI; Raita GOSEKI; Kazusato OIKAWA, et al. Crystallization-Induced Mechanofluorescence for Visualization of Polymer Crystallization. *Nature Communications*, 12, 2021 126. Accessed via: <https://doi.org/10.1038/s41467-020-20366-y>.
92. PREDOI, Daniela; Simona Liliana ICONARU, Mihai Valentin PREDOI; Mikael MOTELICA-HEINO; Regis GUEGAN and Nicolas BUTON. Evaluation of Antibacterial Activity of Zinc-Doped Hydroxyapatite Colloids and Dispersion Stability Using Ultrasounds. *Nanomaterials*, 9, 2019, 4, 515. Accessed via: <https://doi.org/10.3390/nano9040515>.
93. YAO, Bing; Farhad IMANI; Aniket S. SAKPAL; E. W. REUTZEL and Hui YANG. Multifractal analysis of image profiles for the characterization and detection of defects in additive manufacturing. *Journal of Manufacturing Science and Engineering*, 140, 2017, 3, 031014. Accessed via: <https://doi.org/10.1115/1.4037891>.
94. IMANI, Farhad; Bing YAO; Ruimin CHEN; Prahalad RAO and Hui YANG. Joint Multifractal and Lacunarity Analysis of Image Profiles for Manufacturing Quality Control. *Journal of Manufacturing Science and Engineering*, 141, 2019, 4, 044501. Accessed via: <https://doi.org/10.1115/1.4042579>.
95. CHEN, Yun and Hui YANG. Numerical simulation and pattern characterization of nonlinear spatiotemporal dynamics on fractal surfaces for the whole-heart modeling applications. *The European Physical Journal B*, 89, 2016, 181. Accessed via: Pringer Nature Link, <https://doi.org/10.1140/epjb/e2016-60960-6>.
96. AUGUSTYNIAK, J.; I. ZGŁOBICKA; K. KURZYDŁOWSKI; P. MISIAK; A. Z. WILCZEWSKA, et al. Characterization of nanofluids using multifractal analysis of a liquid droplet trace. *Scientific Reports*, 12, 2022, 11111. Accessed via: <https://doi.org/10.1038/s41598-022-15402-4>.
97. CIOBANU, Carmen Stetula; Simona Liliana ICONARU; Mariana Carmen CHIFIRIUC; Adrian COSTESCU; Philippe Le COUSTUMER and Daniela PREDOI. Synthesis and Antimicrobial Activity of Silver-Doped Hydroxyapatite Nanoparticles. *BioMed Research International*, 2013, 916218. Accessed via: Wiley Online Library, <https://doi.org/10.1155/2013/916218>.

98. JANUSAS, Tomas; Sigita URBAITE; Arvydas PALEVICIUS; Sohrab NASIRI and Giedrius JANUSAS. Biologically Compatible Lead-Free Piezoelectric Composite for Acoustophoresis Based Particle Manipulation Techniques. *Sensors*, 21, 2021, 2, 483. Accessed via: <https://doi.org/10.3390/s21020483>.
99. HWANG, S. W.; A. UMAR; G. N. DAR; S. H. KIM and R. I. Badran. Synthesis and Characterization of Iron Oxide Nanoparticles for Phenyl Hydrazine Sensor Applications. *Sensor Letters*, 12, 2014, 1, 97–101. Accessed via: <https://doi.org/10.1166/sl.2014.3224>.
100. ASHOK, M.; N. Meenakshi SUNDARAM and S. Narayana KALKURA. Crystallization of Hydroxyapatite at Physiological Temperature. *Materials Letters*, 57, 2003, 13–14, 2066–2070. Accessed via: ScienceDirect, [https://doi.org/10.1016/S0167-577X\(02\)01140-0](https://doi.org/10.1016/S0167-577X(02)01140-0).
101. GRUBE DOS SANTOS, Gabriel; Milena Schroeder MALHERBI; Natalia SILVA DE SOUZA; Gabriel Batista CÉSAR; Tania Toyomi TOMINAGA, et al. 4th Generation Biomaterials Based on PVDF-Hydroxyapatite Composites Produced by Electrospinning: Processing and Characterization. *Polymers*, 14, 2022, 19, 4190. Accessed via: <https://doi.org/10.3390/polym14194190>.
102. SALIMI, A. and A. A. YOUSEFI. Conformational Changes and Phase Transformation Mechanisms in PVDF Solution-Cast Films. *Journal of Polymer Science. Part B, Polymer Physics*, 42, 2004, 18, 3487–3495. Accessed via: Wiley Online Library, <https://doi.org/10.1002/polb.20223>.
103. CHEN, Qin; Don NATALE; Bret NEESE; Kailiang REN; Minren LIN, et al. Piezoelectric Polymers Actuators for Precise Shape Control of Large Scale Space Antennas. *Electroactive Polyme Actuators and Devices (EAPAD)*, 6524, 2007, 491–501. Accessed via: <https://doi.org/10.1117/12.717696>.
104. GIRIDHAR, Gurram; R. K. N. R. MANEPALLI and Gudimamilla APPARAO. Chapter 8 - Contact Angle Measurement Techniques for Nanomaterials. *Thermal and Rheological Measurement. Techniques for Nanomaterials Characterization*, 2017, 173–195. Accessed via: ScienceDirect, <https://doi.org/10.1016/B978-0-323-46139-9.00008-6>.
105. GARETZ, Bruce A.; Jelena MATIC and Allan S. MYERSON. Polarization Switching of Crystal Structure in the Nonphotochemical Light-Induced Nucleation of Supersaturated Aqueous Glycine Solutions. *Physical Review Letters*, 89, 2002, 175501. Accessed via: <https://doi.org/10.1103/PhysRevLett.89.175501>.
106. ZHENG, Yanqiong; Juncong CHEN; Weiguang LI; Jie TANG; Junbiao PENG; Jianhua ZHANG and Xifeng LI. Investigation of the Characteristic of Solution-Processed Tetraphenyldibenzoperiflanthene (DBP) Film and Its Application on Organic Photovoltaic Cells. *Physical Status Solidi*, 218, 2021, 16, 2100232. Accessed via: Wiley Online Library, <https://doi.org/10.1002/pssa.202100232>.
107. HUHTAMÄKI, Tommi; Xuelin TIAN; Juuso T. KORHONEN and Robin H. A. RAS. Surface-Wetting Characterization Using Contact-Angle Measurements. *Nature Protocols*, 13, 2018, 1521–1538. Accessed via: <https://doi.org/10.1038/s41596-018-0003-z>.
108. AGRAWAL, Khelendra; Gurbhinder SINGH; Devendra PURI and Satya PRAKASH. Synthesis and Characterization of Hydroxyapatite Powder by Sol-Gel Method for Biomedical Application. *Journal of Minerals & Materials Characterization & Engineering*, 10, 2011, 8, 727–734. Accessed via: <https://doi.org/10.4236/jmmce.2011.108057>.
109. KIM, Il-Seok and Prasgant N. KUMTA. Sol-Gel Synthesis and Characterization of Nanostructured Hydroxyapatite Powder. *Materials Science and Engineering: B*, 111,

- 2004, 2–3, 232–236. Accessed via: ScienceDirect, <https://doi.org/10.1016/j.mseb.2004.04.011>.
110. YU, Ling; Yi YANG, Jin ZHANG and Yang YU. Properties and performance of Ag(I) ion imprinted PVDF-PVA/GO composite membrane: Enhanced permeability, rejection and anti-microbial ability. *Water Cycle*, 1, 2020, 121–127. Accessed via: ScienceDirect, <https://doi.org/10.1016/j.watcyc.2020.09.002>.
111. GONÇALVES, R.; A. C. LOPES; G. BOTELHO; I. C. NEVES and S. LANCEROS-MENDEZ. Influence of Solvent Properties on the Electrical Response of Poly(Vinylidene Fluoride)/NaY Composites. *Journal of Polymer Research*, 20, 2013, 143. Accessed via: Springer Nature Link, <https://doi.org/10.1007/s10965-013-0143-3>.
112. HU, Chen; Yujun YANG; Yuqing LIN; Linlin WANG; Rongyang MA; Yanli ZHANG; Xiaoli FENG, Junrong WU; Lili CHEN and Longquan SHAO. GO-based antibacterial composites: Application and design strategies. *Advanced Drug Delivery Reviews*, 178, 2021. Accessed via: ScienceDirect, <https://doi.org/10.1016/j.addr.2021.113967>.
113. CAI, Jing; Ning HU, Liangke WU, Yuhang LIU, Yuan LI, Huiming NING, Xuyang LIU and Liyang LIN. Preparing carbon black/graphene/PVDF-HFP hybrid composite films of high piezoelectricity for energy harvesting technology. *Composites Part A: Applied Science and Manufacturing*, 121, 2019, 223–231. Accessed via: ScienceDirect, <https://doi.org/10.1016/j.compositesa.2019.03.031>.
114. WANG, Yang; Dan LEI; Liangke WU; Ning HU; Huiming NING; Alamusi and Yaolu LIU. Preparation of PVDF-HFP/CB/Ni nanocomposite films for piezoelectric energy harvesting. *Reviews on Advanced Materials Science*, 62, 2023, 1. <https://doi.org/10.1515/rams-2023-0146>.
115. SU, Yanli; Yiqi GU; Hua LI and Fenxia GENG. Ag-NBCTO-PVDF composites with enhanced dielectric properties. *Materials Letters*, 185, 2016, 208–210. Accessed via: ScienceDirect, <https://doi.org/10.1016/j.matlet.2016.08.136>.
116. TOFAIL, S.A.M.; D. HAVERTY; K. T. STANTON and J. B. MCMONAGLE. Structural Order and Dielectric Behaviour of Hydroxyapatite. *Ferroelectrics*, 319, 2011, 1, 117–123. Accessed via: Taylor & Francis Online, <https://doi.org/10.1080/00150190590965523>.
117. NASIRI, Sohrab; MOZHGAN Hosseinneshad; Marzieh RABIEI; Arvydas PALEVICIUS and Giedrius JANUSAS. The Effect of Calcination Temperature on the Photophysical and Mechanical Properties of Copper Iodide (5 Mol%)–Doped Hydroxyapatite. *Optical Materials*, 121, 2021, 111559. Accessed via: ScienceDirect, <https://doi.org/10.1016/j.optmat.2021.111559>.
118. LANG, S. B.; S. A. M. TOFAIL; A. L. KHOLKIN; M. WOJTAŚ; M. GREGOR, et al. Ferroelectric Polarization in Nanocrystalline Hydroxyapatite Thin Films on Silicon. *Scientific Reports*, 3, 2013, 2215. Accessed via: <https://doi.org/10.1038/srep02215>.
119. YANG, Jie; Yihe ZHANG; Yanan LI; Zhihao WANG; Wenjiang WANG; Qi AN and Wangshu TONG. Piezoelectric Nanogenerators based on Graphene Oxide/PVDF Electrospun Nanofiber with Enhanced Performances by In-Situ Reduction. *Materials Today. Communications*, 26, 2021, 101629. Accessed via: ScienceDirect, <https://doi.org/10.1016/j.mtcomm.2020.101629>.
120. CAI, Xiaomei; Tingping LEI; Daoheng SUN and Liwei LIN. A critical analysis of the  $\alpha$ ,  $\beta$  and  $\gamma$  phases in poly(vinylidene fluoride) using FTIR. *RSC Advances*, 7, 2017, 15382–15389. Accessed via: <https://doi.org/10.1039/c7ra01267e>.



## CURRICULUM VITAE

**Name Surname:** Ieva Markūnienė

**Email:** ieva.markuniene@ktu.edu; markuniene.ieva@gmail.com;

### **Education:**

2011 – 2015      **Bachelor's and Master's degrees**

Kaunas University of Technology

2021 – 2025      **Doctor of Philosophy in Mechanical Engineering**

Kaunas University of Technology

### **Work experience:**

2024 02 – 2024 06      Laborant (internship) in TUBITAK Research Center

2024 02 – 2024 06      Practical internship at Gelisim Istanbul University.

## **LIST OF SCIENTIFIC AND OTHER PUBLICATIONS**

Development and analysis of mechanical, physical, and optical properties of composite materials;

Synthesis of piezoelectric, plasmonic, and biocompatible composite materials;

### **Indexed in the Web of Science with Impact Factor:**

1. Markuniene, Ieva; Rabiei, Marzieh; Nasiri, Sohrab; Urbaite, Sigita; Palevicius, Arvydas; Janusas, Giedrius. Biocompatible piezoelectric PVDF/HA/AgNO<sub>3</sub> thin film prepared by the solvent casting method // Sensors. Basel : MDPI. ISSN 1424-8220. 2023, vol. 23, iss. 1, art. no. 289, p. 1-15. DOI: 10.3390/s23010289. [Science Citation Index Expanded (Web of Science); Scopus; MEDLINE] [IF: 3,400; AIF: 4,000; IF/AIF: 0,850; Q2 (2023, InCites JCR SCIE)] [CiteScore: 7,30; SNIP: 1,247; SJR: 0,786; Q1 (2023, Scopus Sources)] [FoR: T 009] [Input: 0,170]
2. Nasiri, Sohrab; Rabiei, Marzieh; Markuniene, Ieva; Hosseinneshad, Mozghan; Ebrahimi-Kahrizsangi, Reza; Palevicius, Arvydas; Vilkauskas, Andrius; Janusas, Giedrius. Nanocomposite based on HA/PVTMS/Cl<sub>2</sub>FeH<sub>8</sub>O<sub>4</sub> as a gas and temperature sensor // Sensors. Basel : MDPI. ISSN 1424-8220. 2022, vol. 22, iss. 24, art. no. 10012, p. 1-16. DOI: 10.3390/s222410012. [Science Citation Index Expanded (Web of Science); Scopus; MEDLINE] [IF: 3,900; AIF: 4,333; IF/AIF: 0,900; Q2 (2022, InCites JCR SCIE)] [CiteScore: 6,80; SNIP: 1,330; SJR: 0,764; Q1 (2022, Scopus Sources)] [FoR: T 009] [Input: 0,125].

### **Indexed in other Web of Science or Scopus publications:**

1. Markuniene, Ieva; Janusas, Giedrius. Synthesis of biocompatible piezoelectric PVDF, HA, AGNO<sub>3</sub> composite material for application in biomechanics // 2024 IEEE 19th international conference on the perspective technologies and

methods in MEMS design (MEMSTECH): Zozuli (Lviv region), Ukraine, 16 - 19 May, 2024: proceedings. Piscataway, NJ : IEEE, 2024. ISBN 9798350378634. eISBN 9798350378627. ISSN 2573-5357. eISSN 2573-5373. p. 128-131. DOI: 10.1109/MEMSTECH63437.2024.10620048. [Conference Proceedings Citation Index - Science (Web of Science); Scopus; Dimensions] [FoR: T 009] [Input: 0,500].

2. Markuniene, Ieva; Palevicius, Arvydas; Vezys, Joris; Augustyniak, Jakub; Perkowski, Dariusz; Urbaite, Sigita; Janusas, Giedrius. Effect of PVDF, HA, and AgNO<sub>3</sub> annealing on  $\beta$ -phase, optical, and mechanical properties // Journal of composites science. Basel : MDPI. ISSN 2504-477X. 2024, vol. 8, iss. 7, art. no. 240, p. 1-23. DOI: 10.3390/jcs8070240. [Emerging Sources Citation Index (Web of Science); Scopus] [CiteScore: 5,00; SNIP: 1,012; SJR: 0,583; Q1 (2023, Scopus Sources)] [FoR: T 009] [Input: 0,148].

### **In peer-reviewed conference proceedings (not indexed in the Web of Science or Scopus):**

1. Markūnienė, I.; Janušas, G. PVDF film with HA, PHA, AGNO<sub>3</sub> fillers for biocompatible piezoelectric sensors // Engineering mechanics 2023: 29th international conference, May 9 – 11, 2023, Milovy, Czech Republic: book of full texts / Vojtěch Radolf and Igor Zolotarev (eds.). Prague: Institute of thermomechanics of the Czech Academy of sciences, 2023. ISBN 9788087012840. ISSN 1805-8248. eISSN 1805-8256. p. 155-158. DOI: 10.21495/em2023-155. [FoR: T 009] [Input: 0,500].
2. Markuniene, Ieva; Janusas, Giedrius. Characterization of beta phase and piezoelectric properties of PVDF/HA/AgNO<sub>3</sub> piezoelectric film // Mechanika 2024: proceedings of the 28th international scientific conference, 31 May 2024, Kaunas University of Technology, Lithuania. Kaunas : Kaunas University of Technology. ISSN 2783-5677. 2024, p. 63-67. [FoR: T 009] [Input: 0,500].
3. Markuniene, Ieva; Janusas, Giedrius. Numerical modelling of PVDF/HA/AGNO<sub>3</sub> piezoelectric composite // Mechanika 2023: proceedings of the 27th international scientific conference, 26 May 2023, Kaunas University of Technology, Lithuania: proceedings. Kaunas : Kaunas University of Technology. ISSN 2783-5677. 2023, p. 236-240. [FoR: T 009] [Input: 0,500].

### **Other conference presentation abstracts and non-peer reviewed conference papers:**

1. Markūnienė, Ieva; Janušas, Giedrius. Synthesis and investigation of biocompatible piezoelectric material // Advanced materials and technologies: book of abstracts of 24th international conference-school, 22-26 August 2022, Palanga, Lithuania. Kaunas : Kaunas University of Technology. ISSN 2669-1930. 2022, B-P90, p. 129. [FoR: T 009].

## ACKNOWLEDGMENTS

The biggest thanks to the superior, Prof. Dr. Giedrius Janušas, for consultations, support, encouragement, and great trust and flexibility. All the ideas and discussions that encouraged me to grow and improve were very useful. I am grateful for the cooperation and dedicated a large amount of time to corrections and development. I am very glad to have had the opportunity to work with you. Thank you for your efforts in promoting cooperation with other departments and sharing all available contacts.

I would also like to thank the consultant Joris Vėžys, who supported me throughout the years of study, provided the necessary information, and helped me learn and understand the peculiarities of measurement.

Many thanks to Simona Tučkutė for the measurements and cooperation. I also want to thank Prof. Dr. Arvydas Palevičius, who supported me throughout my studies, was flexible, and encouraged me to grow.

My thanks to Sigita Urbaitė; she helped and advised me. Thank you for her advice and help in writing research papers, professionalism, and thoroughness.

Special thanks to the Lithuanian Science Council and Kaunas University of Technology for funding and the opportunity to participate in various conferences and scientific events that encouraged international cooperation.

Thanks to the Department of International Erasmus for the cooperation and for the help in organizing the international Erasmus+ internship, during which I got an experience at the Center for Sensory Sciences.

Also, a big thank you to the Doctoral School for coordination, quick responses, financing, and all the consultations that helped me travel during my studies.

I also want to thank the staff of the Faculty of Mechanical Engineering and Design for their help, support, and encouragement.

I would especially like to thank my family, who always believed in me, encouraged me, and have been happy and proud of me since the beginning of my studies.



UDK 681.586+620.168+537.226.86](043.3)

SL344. 2025-04-29, 16,5 leidyb. apsk. l. Tiražas 14 egz. Užsakymas 62.  
Išleido Kauno technologijos universitetas, K. Donelaičio g. 73, 44249 Kaunas  
Spausdino leidyklos „Technologija“ spaustuvė, Studentų g. 54, 51424 Kaunas

